

Simultaneous Measurement of Oscillation Parameters in Beam and Atmospheric Neutrino Data from Tokai-to-Kamioka and Super-Kamiokande Experiments

Daniel Robert Clement Barrow

Magdalen College, Oxford University

¹⁰ A Dissertation Submitted to Oxford University

¹¹ for the Degree of Doctor of Philosophy

¹²

13 **Simultaneous Measurement of**

14 **Oscillation Parameters in Beam and**

15 **Atmospheric Neutrino Data from**

16 **Tokai-to-Kamioka and**

17 **Super-Kamiokande Experiments**

18 *Abstract*

19 Lorem ipsum dolor sit amet, consectetur adipiscing elit, sed do eiusmod tempor incididunt ut labore et dolore magna aliqua. Nulla aliquet porttitor lacus luctus accumsan tortor posuere. Pulvinar neque laoreet suspendisse interdum. Sem viverra aliquet eget sit. Nunc sed velit dignissim sodales ut eu sem integer vitae. At erat pellentesque adipiscing commodo elit at imperdiet dui accumsan. Fames ac turpis egestas integer eget aliquet nibh. Scelerisque eu ultrices vitae auctor eu augue. Purus non enim praesent elementum facilisis leo vel. Sollicitudin nibh sit amet commodo. Vitae auctor eu augue ut. Vel quam elementum pulvinar etiam. A condimentum vitae sapien pellentesque habitant morbi tristique senectus. Viverra accumsan in nisl nisi scelerisque eu ultrices. Sed viverra ipsum nunc aliquet bibendum enim. Sit amet purus gravida quis. In vitae turpis massa

³² sed elementum tempus egestas sed sed. Vivamus arcu felis bibendum
³³ ut tristique et egestas. Senectus et netus et malesuada fames ac turpis.
³⁴ Ac auctor augue mauris augue.

35 Declaration

36 This dissertation is the result of my own work, except where ex-
37 plicit reference is made to the work of others, and has not been sub-
38 mitted for another qualification to this or any other university. This
39 dissertation does not exceed the word limit for the respective Degree
40 Committee.

41 Daniel Robert Clement Barrow

42 ©The copyright of this thesis rests with the author and is made available under a Creative
43 Commons Attribution Non-Commercial No Derivatives licence. Researchers are free to copy,
44 distribute or transmit the thesis on the condition that they attribute it, that they do not use
45 it for commercial purposes and that they do not alter, transform or build upon it. For any
46 reuse or redistribution, researchers must make clear to others the licence terms of this work.

47

Acknowledgements

48 at pretium nibh ipsum. Eget nunc scelerisque viverra mauris in aliquam. Arcu vitae
49 elementum curabitur vitae nunc sed velit dignissim. Sed arcu non odio euismod lacinia
50 at quis risus sed. Vitae tempus quam pellentesque nec nam aliquam sem et tortor.
51 Viverra aliquet eget sit amet tellus cras adipiscing. Purus sit amet luctus venenatis
52 lectus magna. In aliquam sem fringilla ut morbi tincidunt augue. Fermentum dui
53 faucibus in ornare. Aliquam malesuada bibendum arcu vitae elementum curabitur
54 vitae nunc sed.

55 Ultricies leo integer malesuada nunc vel risus commodo. Tellus cras adipiscing
56 enim eu turpis egestas pretium. Dictumst quisque sagittis purus sit amet volutpat
57 consequat mauris nunc. Vitae congue mauris rhoncus aenean vel elit scelerisque
58 mauris pellentesque. Vel facilisis volutpat est velit egestas dui id ornare. Suscipit
59 adipiscing bibendum est ultricies. At in tellus integer feugiat scelerisque varius
60 morbi enim. Cras semper auctor neque vitae tempus. Commodo sed egestas egestas
61 fringilla phasellus faucibus. Cras pulvinar mattis nunc sed blandit. Pretium viverra
62 suspendisse potenti nullam ac tortor vitae. Purus sit amet volutpat consequat. Orci
63 sagittis eu volutpat odio facilisis mauris. Sit amet massa vitae tortor condimentum
64 lacinia quis. Commodo sed egestas egestas fringilla phasellus. Sed libero enim sed
65 faucibus turpis. Vitae tempus quam pellentesque nec.

66 Blandit massa enim nec dui. Viverra tellus in hac habitasse platea dictumst vestibulu-
67 lum. Bibendum enim facilisis gravida neque convallis. Sagittis nisl rhoncus mattis
68 rhoncus urna neque. Nisl rhoncus mattis rhoncus urna neque. Ac tortor vitae purus
69 faucibus ornare. Aenean sed adipiscing diam donec adipiscing tristique risus. Sapien
70 nec sagittis aliquam malesuada bibendum. Et leo duis ut diam quam nulla. Tellus
71 rutrum tellus pellentesque eu tincidunt tortor aliquam nulla facilisi. Fermentum leo

⁷² vel orci porta non pulvinar neque. Eget sit amet tellus cras adipiscing enim eu. Sed
⁷³ viverra tellus in hac habitasse platea dictumst vestibulum.

⁷⁴ Sit amet consectetur adipiscing elit. At varius vel pharetra vel turpis nunc eget
⁷⁵ lorem. Elit scelerisque mauris pellentesque pulvinar pellentesque habitant morbi
⁷⁶ tristique senectus. Odio euismod lacinia at quis risus sed vulputate odio. Vitae suscipit
⁷⁷ tellus mauris a diam maecenas sed enim ut. Dignissim convallis aenean et tortor at
⁷⁸ risus viverra. Diam sollicitudin tempor id eu. Erat velit scelerisque in dictum. Blandit
⁷⁹ cursus risus at ultrices. Ac tortor vitae purus faucibus ornare suspendisse sed.

Contents

81	1	Neutrino Oscillation Physics	1
82	1.1	Discovery of Neutrinos	1
83	1.2	Theory of Neutrino Oscillation	3
84	1.2.1	Three Flavour Oscillations	3
85	1.2.2	The MSW Effect	7
86	1.3	Neutrino Oscillation Measurements	8
87	1.3.1	Solar Neutrinos	9
88	1.3.2	Atmospheric Neutrinos	11
89	1.3.3	Accelerator Neutrinos	14
90	1.3.4	Reactor Neutrinos	17
91	2	T2K and SK Experiment Overview	20
92	2.1	The Super-Kamiokande Experiment	20
93	2.1.1	The SK Detector	21
94	2.1.2	Calibration	25
95	2.1.3	Data Acquisition and Triggering	28
96	2.1.4	Cherenkov Radiation	30
97	2.2	The Tokai to Kamioka Experiment	32
98	2.2.1	The Neutrino Beam	34
99	2.2.2	The Near Detector at 280m	37
100	2.2.2.1	Fine Grained Detectors	40
101	2.2.2.2	Time Projection Chambers	41
102	2.2.2.3	π^0 Detector	43
103	2.2.2.4	Electromagnetic Calorimeter	43
104	2.2.2.5	Side Muon Range Detector	45

105	2.2.3 The Interactive Neutrino GRID	45
106	3 Bayesian Statistics and Markov Chain Monte Carlo Techniques	47
107	3.1 Bayesian Statistics	48
108	3.2 Monte Carlo Simulation	49
109	3.2.1 Markov Chain Monte Carlo	51
110	3.2.2 Metropolis-Hastings Algorithm	54
111	3.2.3 MCMC Optimisation	55
112	3.3 Understanding the MCMC Results	59
113	3.3.1 Marginalisation	59
114	3.3.2 Parameter Estimation and Credible Intervals	60
115	3.3.3 Application of Bayes' Theorem	62
116	3.3.4 Comparison of MCMC Output to Expectation	63
117	4 Oscillation Probability Calculation	65
118	4.1 Overview	66
119	4.2 Treatment of Fast Oscillations	72
120	4.3 Calculation Engine	82
121	4.4 Matter Density Profile	83
122	4.5 Production Height Averaging	89
123	Bibliography	93
124	List of Figures	101
125	List of Tables	108

¹²⁷ **Chapter 1**

¹²⁸ **Neutrino Oscillation Physics**

¹²⁹ When first proposed, neutrinos were expected to be massless fermions that only in-
¹³⁰ teract through weak and gravitational forces. This meant they were very difficult to
¹³¹ detect as they can pass through significant amounts of matter without interacting. De-
¹³² spite this, experimental neutrino physics has developed with many different detection
¹³³ techniques and neutrino sources being used today. In direct tension with the standard
¹³⁴ model physics, neutrinos have been determined to oscillate between different lepton
¹³⁵ flavours requiring them to have mass.

¹³⁶ section 1.1 describes the observation techniques and discovery of neutrinos. The
¹³⁷ theory underpinning neutrino oscillation is described in section 1.2. This section
¹³⁸ includes the approximations which can be made to simplify the understanding of
¹³⁹ neutrino oscillation in a two-flavour approximation as well as how the medium
¹⁴⁰ in which neutrinos propagate can manipulate the oscillation probability. The past,
¹⁴¹ current, and future neutrino experiments are detailed in section 1.3 including the
¹⁴² reactor, atmospheric, and long-baseline accelerator neutrino sources that have been
¹⁴³ used to successfully constrain oscillation parameter determination.

¹⁴⁴ **1.1 Discovery of Neutrinos**

¹⁴⁵ At the start of the 20th century, the electrons emitted from the β -decay of the nucleus
¹⁴⁶ were found to have a continuous energy spectrum [1,2]. This observation seemingly
¹⁴⁷ broke the energy conservation invoked within that period's nuclear models. Postulated

in 1930 by Pauli as the solution to this problem, the neutrino (originally termed “neutron”) was theorized to be an electrically neutral spin-1/2 fermion with a mass of the same order of magnitude as the electron [3]. This neutrino was to be emitted with the electron in β -decay to alleviate the apparent breaking of energy conservation. As a predecessor of the weak interaction model, Fermi’s theory of β -decay developed the understanding by coupling the four constituent particles; electron, proton, neutron, and neutrino, into a consistent model [4].

Whilst Pauli was not convinced of the ability to detect neutrinos. The first observations of the particle were made in the mid-1950s when neutrinos from a reactor were observed via the inverse β -decay (IBD) process, $\bar{\nu}_e + p \rightarrow n + e^+$ [5, 6]. The detector consisted of two parts; a neutrino interaction medium and a liquid scintillator. The interaction medium was built from two water tanks. These were loaded with cadmium chloride to allow increased efficiency of neutron capture. The positron emitted from IBD annihilates, $e^+ + e^- \rightarrow 2\gamma$, generating a prompt signal and the neutron is captured on the cadmium via $n + ^{108}Cd \rightarrow ^{109}Cd \rightarrow ^{109}Cd + \gamma$, producing a delayed signal. The experiment observed an increase in the neutrino event rate when the reactor was operating compared to when it was switched off, in much the same way as modern reactor neutrino experiments operate.

After the discovery of the ν_e , the natural question of how many flavours of neutrino exist was asked. In 1962, a measurement of the ν_μ was conducted at the Brookhaven National Laboratory [7]. A proton beam was directed at a beryllium target, generating a π -dominated beam which then decayed via $\pi^\pm \rightarrow \mu^\pm + (\nu_\mu, \bar{\nu}_\mu)$, and the subsequent interactions of the ν_μ were observed. The final observation to be made was that of the ν_τ from the DONUT experiment [8]. Three neutrinos seem the obvious solution as it mirrors the known number of charged lepton (as they form weak isospin doublets) but there could be evidence of more. Several neutrino experiments have found anomalous

₁₇₄ results [9, 10] which could be attributed to sterile neutrinos however cosmological
₁₇₅ observations indicate the number of neutrino species $N_{eff} = 3.15 \pm 0.23$ [11].

₁₇₆ 1.2 Theory of Neutrino Oscillation

₁₇₇ As direct evidence of beyond Standard Model physics, a neutrino generated with
₁₇₈ lepton flavour α can change into a different lepton flavour β after propagating some
₁₇₉ distance. This phenomenon is called neutrino oscillation and requires that neutrinos
₁₈₀ must have a non-zero mass (as seen in subsection 1.2.1). This is direct evidence
₁₈₁ of beyond standard model physics. This behaviour has been characterised by the
₁₈₂ Pontecorvo-Maki-Nakagawa-Sakata (PMNS) [12–14] mixing matrix which describes
₁₈₃ how the flavour and mass of neutrinos are associated. This is analogous to the Cabibbo-
₁₈₄ Kobayashi-Maskawa (CKM) [15] matrix measured in quark physics.

₁₈₅ 1.2.1 Three Flavour Oscillations

₁₈₆ The PMNS parameterisation defines three flavour eigenstates, ν_e , ν_μ and ν_τ (indexed
₁₈₇ ν_α), which are assigned based upon the weak interaction flavour states and three mass
₁₈₈ eigenstates, ν_1 , ν_2 and ν_3 (indexed ν_i). Each mass eigenstate is the superposition of all
₁₈₉ three flavour states,

$$|\nu_i\rangle = \sum_\alpha U_{\alpha i} |\nu_\alpha\rangle. \quad (1.1)$$

₁₉₀ U is the PMNS matrix which correlates the mass and flavour eigenstates. Neutrinos
₁₉₁ interact with leptons of the same weak flavour eigenstate rather than mass eigenstate.

¹⁹² The propagation of a neutrino flavour eigenstate, in a vacuum, can be re-written as a
¹⁹³ plane-wave solution to the time-dependent Schrödinger equation,

$$|\nu_\alpha(t)\rangle = \sum_i U_{\alpha i}^* |\nu_i\rangle e^{-i\phi_i}. \quad (1.2)$$

¹⁹⁴ The probability of observing a neutrino of flavour eigenstate β from one which
¹⁹⁵ originated as flavour α can be calculated as,

$$P(\nu_\alpha \rightarrow \nu_\beta) = |\langle \nu_\beta | \nu_\alpha(t) \rangle|^2 = \sum_{i,j} U_{\alpha i}^* U_{\beta i} U_{\alpha j} U_{\beta j}^* e^{-i(\phi_j - \phi_i)} \quad (1.3)$$

¹⁹⁶ The ϕ_i term can be expressed in terms of the energy, E_i , and magnitude of the
¹⁹⁷ three momenta, p_i , of the neutrino, $\phi_i = E_i t - p_i x$ (t and x being time and position
¹⁹⁸ coordinates). Therefore,

$$\phi_j - \phi_i = E_j t - E_i t - p_j x + p_i x. \quad (1.4)$$

¹⁹⁹ For a relativistic particle, $E_i \gg m_i$,

$$p_i = \sqrt{E_i^2 - m_i^2} \approx E_i - \frac{m_i^2}{2E_i}. \quad (1.5)$$

²⁰⁰ Making the approximations that neutrinos are relativistic, the mass eigenstates
²⁰¹ were created with the same energy and that $x = L$, where L is the distance traveled by
²⁰² the neutrino, Equation 1.4 then becomes

$$\phi_j - \phi_i = \frac{\Delta m_{ij}^2 L}{2E}, \quad (1.6)$$

²⁰³ where $\Delta m_{ij}^2 = m_i^2 - m_j^2$. This, teamed with further use of unitarity relations results
²⁰⁴ in Equation 1.3 becoming

$$P(\nu_\alpha \rightarrow \nu_\beta) = \delta_{\alpha\beta} - 4 \sum_{i>j} \Re \left(U_{\alpha i}^* U_{\beta i} U_{\alpha j} U_{\beta j}^* \right) \sin^2 \left(\frac{\Delta m_{ij}^2 L}{4E} \right) + (-) 2 \sum_{i>j} \Im \left(U_{\alpha i}^* U_{\beta i} U_{\alpha j} U_{\beta j}^* \right) \sin \left(\frac{\Delta m_{ij}^2 L}{2E} \right). \quad (1.7)$$

²⁰⁵ Where $\delta_{\alpha\beta}$ is the Kronecker delta function and the negative sign is included for the
²⁰⁶ oscillation probability of antineutrinos.

²⁰⁷ Typically, the PMNS matrix is parameterised into three mixing angles, a charge
²⁰⁸ parity (CP) violating phase δ_{CP} , and two Majorana phases $\alpha_{1,2}$,

$$U = \underbrace{\begin{pmatrix} 1 & 0 & 0 \\ 0 & c_{23} & s_{23} \\ 0 & -s_{23} & c_{23} \end{pmatrix}}_{\text{Atmospheric, Accelerator}} \underbrace{\begin{pmatrix} c_{13} & 0 & s_{13}e^{-i\delta_{CP}} \\ 0 & 1 & 0 \\ -s_{13}e^{-i\delta_{CP}} & 0 & c_{13} \end{pmatrix}}_{\text{Reactor, Accelerator}} \underbrace{\begin{pmatrix} c_{12} & s_{12} & 0 \\ -s_{12} & c_{12} & 0 \\ 0 & 0 & 1 \end{pmatrix}}_{\text{Reactor, Solar}} \underbrace{\begin{pmatrix} e^{i\alpha_1/2} & 0 & 0 \\ 0 & e^{i\alpha_2/2} & 0 \\ 0 & 0 & 1 \end{pmatrix}}_{\text{Majorana}}. \quad (1.8)$$

209 Where $s_{ij} = \sin(\theta_{ij})$ and $c_{ij} = \cos(\theta_{ij})$. The oscillation parameters are often
210 grouped; (1, 2) as “solar”, (2, 3) as “atmospheric” and (1, 3) as “reactor”. Many
211 neutrino experiments aim to measure the PMNS parameters from a wide array of
212 origins, as is the purpose of this thesis.

213 The Majorana phase, $\alpha_{1,2}$, containing matrix included within Equation 1.8 is only
214 included for completeness. For an oscillation analysis experiment, any term in this
215 oscillation probability calculation containing this phase disappears due to taking the
216 expectation value of the PMNS matrix.

217 A two flavour approximation can be attained when one assumes the third mass
218 eigenstate is degenerate with another. As discussed in section 1.3, it is found that
219 $\Delta m_{21}^2 \ll |\Delta m_{31}^2|$. This results in the two flavour approximation being reasonable for
220 understanding the features of the oscillation. In this two flavour case, the mixing
221 matrix becomes,

$$U_{2\text{ Flav.}} = \begin{pmatrix} \cos(\theta) & \sin(\theta) \\ -\sin(\theta) & \cos(\theta) \end{pmatrix}. \quad (1.9)$$

222 This culminates in the oscillation probability,

$$\begin{aligned} P(\nu_\alpha \rightarrow \nu_\alpha) &= 1 - \sin^2(2\theta) \sin^2\left(\frac{\Delta m^2 L}{4E}\right), \\ P(\nu_\alpha \rightarrow \nu_\beta) &= \sin^2(2\theta) \sin^2\left(\frac{\Delta m^2 L}{4E}\right). \end{aligned} \quad (1.10)$$

223 For $\alpha \neq \beta$. For a fixed neutrino energy, the oscillation probability is a sinusoidal
224 function depending upon the distance over which the neutrino propagates. The

225 frequency and amplitude of oscillation are dependent upon the ratio of the $\Delta m^2 / 4E$
226 and $\sin^2 2\theta$, respectively. For more human-readable units, the maximum oscillation
227 probability for a fixed value of θ is given at $L[km] / E[GeV] \sim 1.27 / \Delta m^2$. It is this
228 calculation that determines the best L/E value for a given experiment to be designed
229 around for measurements of a specific value of Δm^2 .

230 1.2.2 The MSW Effect

231 The theory of neutrino oscillation in a vacuum is described in subsection 1.2.1. How-
232 ever, the beam neutrinos and atmospheric neutrinos originating from below the
233 horizon propagate through matter in the Earth. The coherent scattering of neutrinos
234 from a material target modifies the hamiltonian of the system. This results in a change
235 in the oscillation probability. Notably, charged current scattering ($\nu_e + e^- \rightarrow \nu_e + e^-$,
236 propagated by a W boson) only affects electron neutrinos compared to the neutral
237 current scattering ($\nu_l + l^- \rightarrow \nu_l + l^-$, propagated by a Z^0 boson), interacts through
238 all neutrino flavours equally. In the two-flavour limit, the effective mixing parameter
239 becomes

$$\sin^2(2\theta) \rightarrow \sin^2(2\theta_m) = \frac{\sin^2(2\theta)}{(A/\Delta m^2 - \cos(2\theta))^2 + \sin^2(2\theta)}, \quad (1.11)$$

240 where $A = 2\sqrt{2}G_F N_e E$ with N_e is the electron density of the medium and G_F is
241 Fermi's constant. It is clear to see that there exists a value of $A = \Delta m^2 \cos(2\theta)$ for
242 $\Delta m^2 > 0$ which results in a divergent mixing parameter. This resonance is due to
243 the Mikheyev-Smirnov-Wolfenstein (MSW) effect (or more colloquially, the matter
244 resonance) which regenerates the electron neutrino component of the neutrino flux
245 [16–18]. The density at which the resonance occurs is given by

$$N_e = \frac{\Delta m^2 \cos(2\theta)}{2\sqrt{2}G_F E}. \quad (1.12)$$

246 At densities lower than this critical value, the oscillation probability will be much
247 closer to that of vacuum oscillation. The resonance occurring from the MSW effect
248 depends on the sign of Δm^2 . Therefore, any neutrino oscillation experiment which
249 observes neutrinos and antineutrinos which have propagated through matter can have
250 some sensitivity to the ordering of the neutrino mass eigenstates.

251 1.3 Neutrino Oscillation Measurements

252 As evidence of beyond standard model physics, the 2015 Nobel Prize in Physics was
253 awarded to the Super-Kamiokande (SK) [19] and Sudbury Neutrino Observatory
254 (SNO) [20] collaborations for the first definitive observation of solar and atmospheric
255 neutrino oscillation [21]. Since then, the field has seen a wide array of oscillation
256 measurements from a variety of neutrino sources. As seen in subsection 1.2.1, the
257 neutrino oscillation probability is dependent on the ratio of the propagation baseline, L ,
258 to the neutrino energy, E . It is this ratio that determines the type of neutrino oscillation
259 a particular experiment is sensitive to.

260 As illustrated in Figure 1.1, there are many neutrino sources that span a wide
261 range of energies. The least energetic neutrinos are from diffuse supernovae and
262 terrestrial neutrinos at $O(1)\text{MeV}$ whereas the most energetic neutrinos originate from
263 atmospheric and galactic neutrinos of $> O(1)\text{TeV}$.

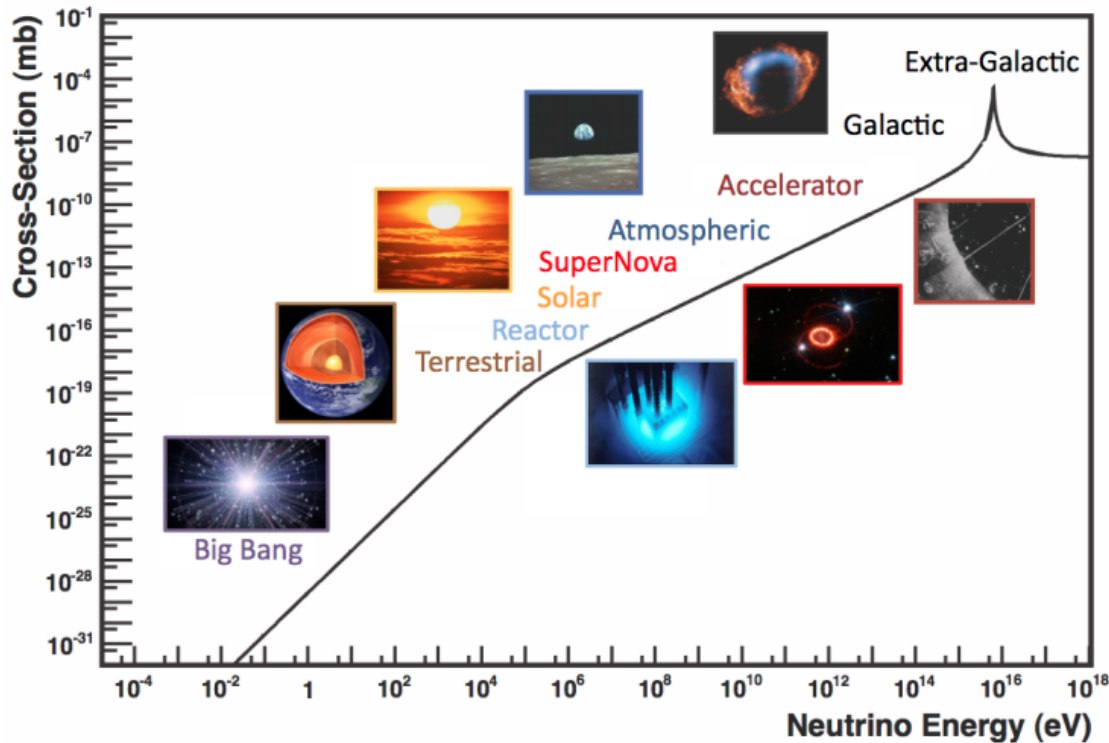


Figure 1.1: The cross-section of neutrinos from various natural and man-made sources as a function of neutrino energy. Taken from [22]

264 1.3.1 Solar Neutrinos

265 Solar neutrinos are emitted from fusion reaction chains at the center of the Sun. The
 266 solar neutrino flux, given as a function of neutrino energy for different fusion and
 267 decay chains is illustrated in Figure 1.2. Whilst proton-proton fusion generates the
 268 largest flux of neutrinos, the neutrinos are of low energy and are difficult to reconstruct
 269 due to the IBD interaction threshold of 1.8MeV. Consequently, most experiments focus
 270 on the neutrinos from the decay of 8B (via ${}^8B \rightarrow {}^8Be^* + e^+ + \nu_e$), which are higher
 271 energy.

272 The first measurements of solar neutrinos observed a significant reduction in the
 273 event rate compared to predictions from the Standard Solar Model [24, 25]. The
 274 proposed solution to this “solar neutrino problem” was $\nu_e \leftrightarrow \nu_\mu$ oscillations in a

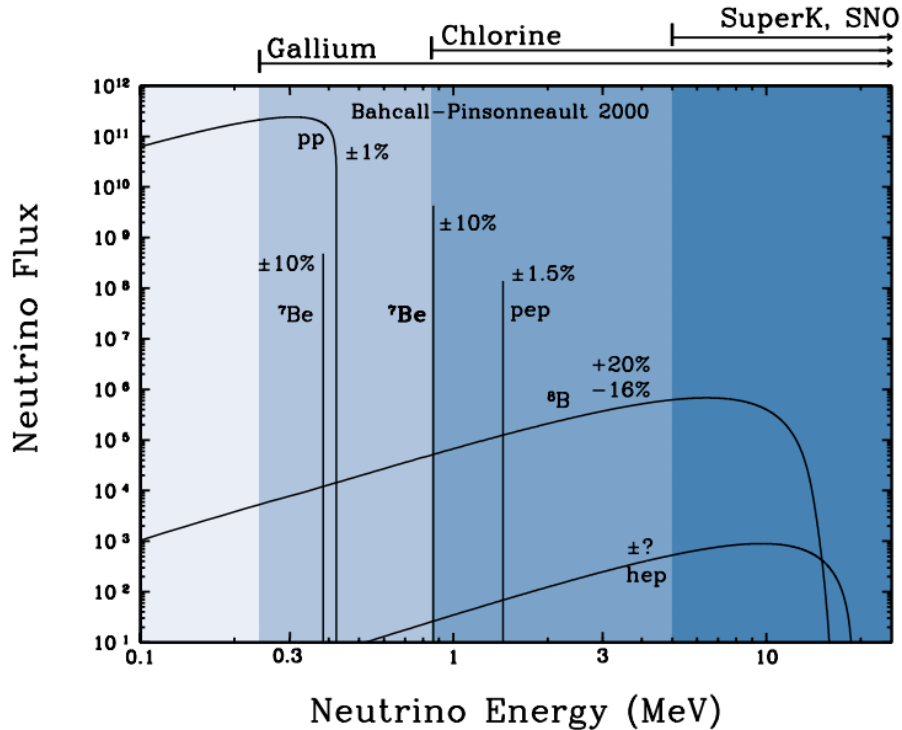


Figure 1.2: The solar neutrino flux as a function of neutrino energy for various fusion reactions and decay chains as predicted by the Standard Solar Model. Taken from [23].

275 precursory version of the PMNS model [26]. The Kamiokande [27], Gallex [28] and
 276 Sage [29] experiments confirmed the ~ 0.5 factor deficit of solar neutrinos.

277 The conclusive solution to this problem was determined by the SNO collabora-
 278 tion [30]. Using a deuterium water target to observe 8B neutrinos, the event rate of
 279 charged current (CC), neutral current (NC), and elastic scattering (ES) interactions
 280 (Given in Equation 1.13) was simultaneously measured. CC events can only occur for
 281 electron neutrinos, whereas the other interaction channels are agnostic to neutrino
 282 flavour (Although the ES reaction is more sensitive to electron neutrino interactions).
 283 This meant that there were direct measurements of the ν_e and ν_x neutrino flux. It
 284 was concluded that the CC and ES interaction rates were consistent with the deficit
 285 previously observed. Most importantly, the NC reaction rate was only consistent with
 286 the others under the hypothesis of flavour transformation.

$$\begin{aligned}
 \nu_e + d &\rightarrow p + p + e^- & (CC) \\
 \nu_x + d &\rightarrow p + n + \nu_x & (NC) \\
 \nu_x + e^- &\rightarrow \nu_x + e^- & (ES)
 \end{aligned} \tag{1.13}$$

287 Many experiments have since measured the neutrino flux of different interaction
 288 chains within the sun [31–33]. The most recent measurement was that of CNO neutrinos
 289 which were recently observed with 5σ significance by the Borexino collaboration.
 290 Future neutrino experiments aim to further these spectroscopic measurements of
 291 different fusion chains within the Sun [34–36]. Solar neutrinos act as an irreducible
 292 background for dark matter experiments like DARWIN but oscillation parameter
 293 measurements can be made [37].

294 1.3.2 Atmospheric Neutrinos

295 The interactions of primary cosmic ray protons in Earth’s upper atmosphere generate
 296 showers of energetic hadrons. These are mostly pions and kaons which when they
 297 decay produce a natural source of neutrinos spanning energies of MeV to TeV [38].
 298 This decay is via

$$\begin{aligned}
 \pi^\pm &\rightarrow \mu^\pm + (\nu_\mu, \bar{\nu}_\mu) \\
 \mu^\pm &\rightarrow e^\pm + (\nu_\mu, \bar{\nu}_\mu) + (\nu_e, \bar{\nu}_e)
 \end{aligned} \tag{1.14}$$

299 such that for a single pion decay, three neutrinos are produced. The atmospheric
 300 neutrino flux energy spectra as predicted by the Bartol [39], Honda [40, 41], and
 301 FLUKA [42] models are illustrated in Figure 1.3. The flux distribution peaks at an

³⁰² energy of $O(10)$ GeV. The uncertainties associated with these models are dominated
³⁰³ by the hadronic production of kaon and pions as well as the primary cosmic flux.

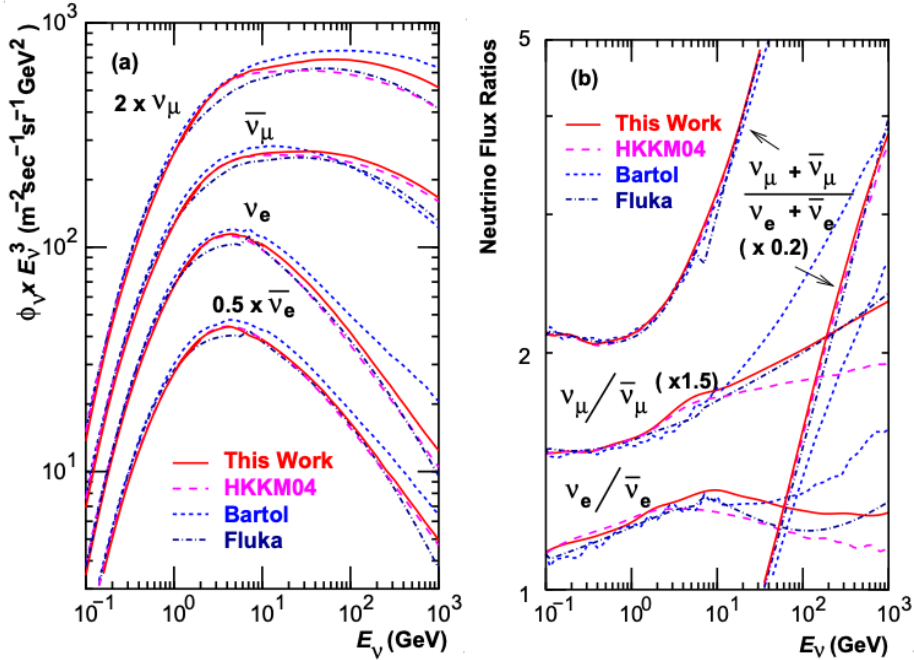


Figure 1.3: Left panel: The atmospheric neutrino flux for different neutrino flavours as a function of neutrino energy as predicted by the 2007 Honda model (“This work”) [40], the 2004 Honda model (“HKKM04”) [41], the Bartol model [39] and the FLUKA model [42]. Right panel: The ratio of the muon to electron neutrino flux as predicted by all the quoted models. Both figures taken from [40].

³⁰⁴ Unlike long-baseline experiments which have a fixed baseline, the distance at-
³⁰⁵ mospheric neutrinos propagate is dependent upon the zenith angle at which they
³⁰⁶ interact. This is illustrated in Figure 1.4. Neutrinos that are generated directly above
³⁰⁷ the detector ($\cos(\theta) = 1.0$) have a baseline equivalent to the height of the atmosphere
³⁰⁸ whereas neutrinos that interact directly below the detector ($\cos(\theta) = -1.0$) have to
³⁰⁹ travel a length equal to the diameter of the Earth. This means atmospheric neutrinos
³¹⁰ have a baseline that varies from $O(20)$ km to $O(6 \times 10^3)$ km. Any neutrino generated
³¹¹ at or below the horizon will be subject to matter effects as they propagate through the
³¹² Earth.

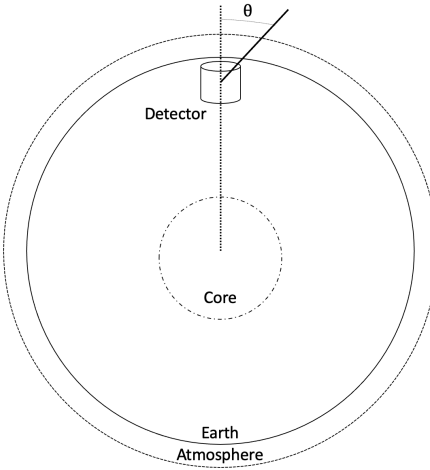


Figure 1.4: A diagram illustrating the definition of zenith angle as used in the Super Kamiokande experiment [43].

313 Figure 1.5 highlights the neutrino flux as a function of the zenith angle for different

314 slices of neutrino energy. For medium to high-energy neutrinos (and to a lesser degree

315 for low-energy neutrinos), the flux is approximately symmetric around $\cos(\theta) = 0$.

316 To the accuracy of this approximation, the systematic uncertainties associated with

317 atmospheric flux for comparing upward-going and down-going neutrino cancels. This

318 allows the down-going events, which are mostly insensitive to oscillation probabilities,

319 to act as an unoscillated prediction (similar to a near detector in an accelerator neutrino

320 experiment).

321 Precursory hints of atmospheric neutrinos were observed in the mid-1960s search-

322 ing for $\nu_\mu^{(-)} + X \rightarrow X^* + \mu^\pm$ [44]. This was succeeded with the IMB-3 [45] and

323 Kamiokande [46] experiments which measured the ratio of muon neutrinos com-

324 pared to electron neutrinos $R(\nu_\mu/\nu_e)$. Both experiments were found to have a con-

325 sistent deficit of muon neutrinos, with $R(\nu_\mu/\nu_e) = 0.67 \pm 0.17$ and $R(\nu_\mu/\nu_e) =$

326 $0.60^{+0.07}_{-0.06} \pm 0.05$. Super-Kamiokande (SK) [43] extended this analysis by fitting os-

327 cillation parameters in $P(\nu_\mu \rightarrow \nu_\tau)$ which found best fit parameters $\sin^2(2\theta) > 0.92$

328 and $1.5 \times 10^{-3} < \Delta m^2 < 3.4 \times 10^{-3} \text{ eV}^2$.

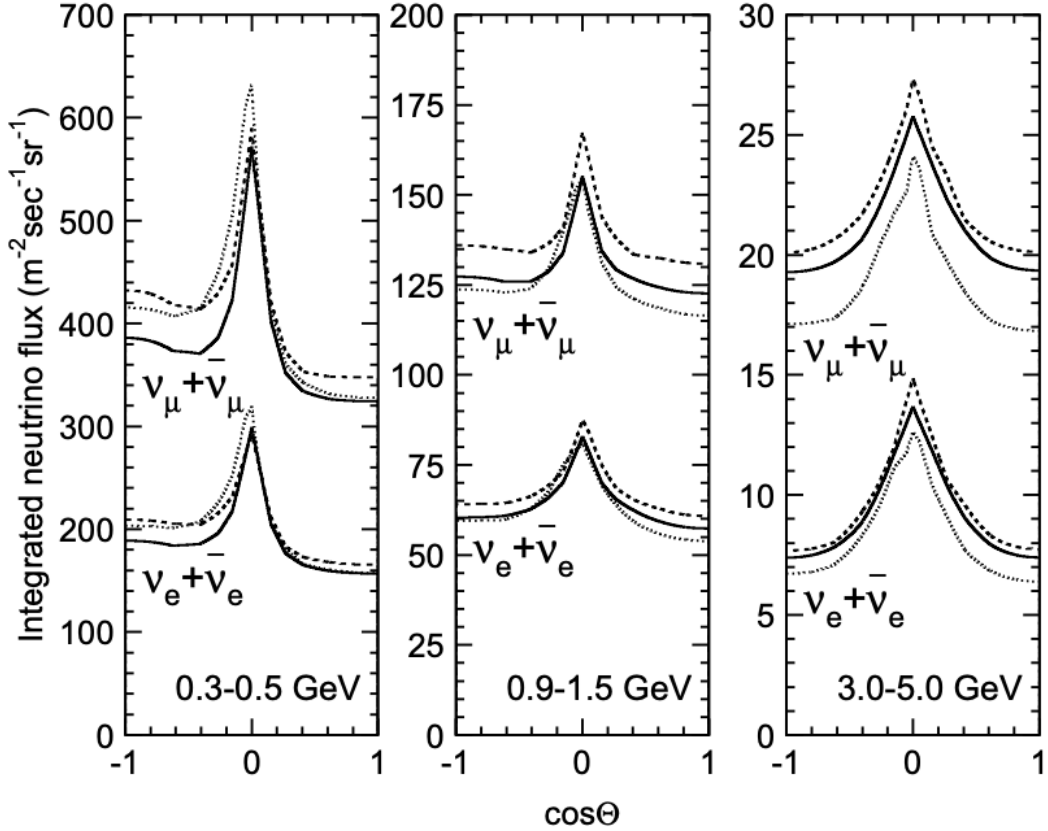


Figure 1.5: Predictions of the summed neutrino and antineutrino flux for electron and muon neutrinos from the Bartol [39], Honda [40] and FLUKA [42] models as a function of zenith angle with respect to the detector. Left panel: $0.3 < E_\nu < 0.5$. Middle panel: $0.9 < E_\nu < 1.5$. Right panel: $3.0 < E_\nu < 5.0$. Figures taken from [43].

Since then, atmospheric neutrino experiments have been making precision measurements of the $\sin^2(\theta_{23})$ and Δm_{32}^2 oscillation parameters. Atmospheric neutrino oscillation is dominated by $P(\nu_\mu \rightarrow \nu_\tau)$, where SK observed a 4.6σ discovery of ν_τ appearance [47]. Figure 1.6 illustrates the current estimates on the atmospheric mixing parameters from a wide range of atmospheric and accelerator neutrino observatories.

1.3.3 Accelerator Neutrinos

The concept of using a man-made “neutrino beam” was first realised in 1962 [54]. Since then, many experiments have followed which all use the same fundamental concepts. Typically, a proton beam is aimed at a target producing charged mesons that

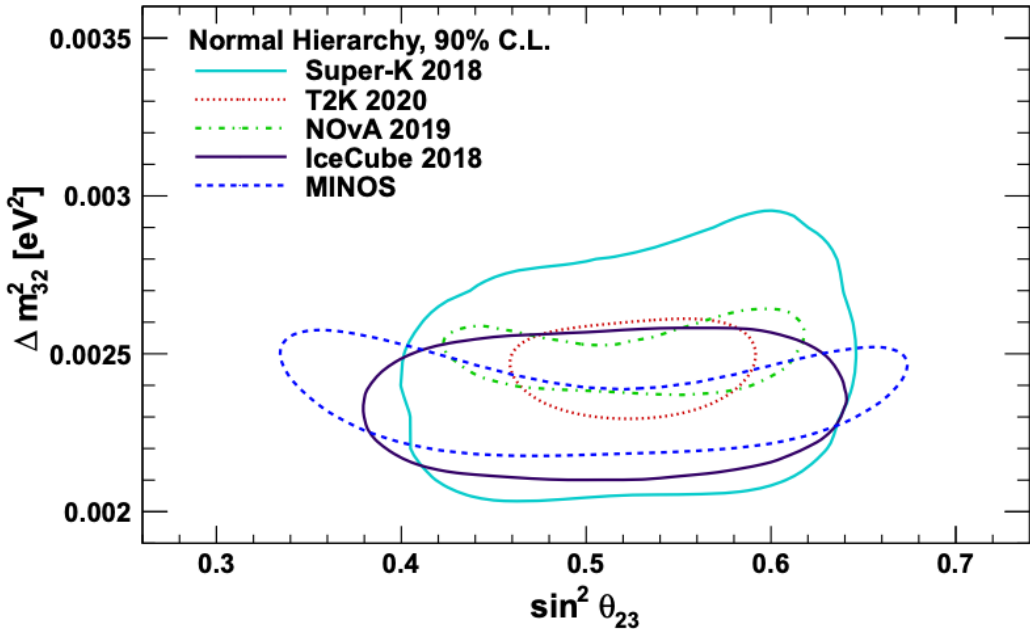


Figure 1.6: Constraints on the atmospheric oscillation parameters, $\sin^2(\theta_{23})$ and Δm_{32}^2 , from atmospheric and long baseline experiments: SK [48], T2K [49], NO ν A [50], IceCube [51] and MINOS [52]. Figure taken from [53].

decay to neutrinos. The mesons can be sign-selected by the use of magnetic focusing horns to generate a neutrino or antineutrino beam. Pions are the primary meson that decay and depending on the orientation of the magnetic field, a muon (anti-)neutrino beam is generated via $\pi^+ \rightarrow \mu^+ + \nu_\mu$ or $\pi^- \rightarrow \mu^- + \bar{\nu}_\mu$. The decay of muons and kaons does result in an irreducible intrinsic electron neutrino background. In T2K, this background contamination is $O(< 1\%)$ [55]. There is also an approximately $\sim 5\%$ “wrong-sign” neutrino background of $\bar{\nu}_\mu$ generated via the same decays.

The energy of each neutrino in the beam is dependent on the energy of the initial proton beam. Therefore, tuning the proton energy allows the neutrino energy to be set to a value that maximises the disappearance oscillation probability in the L/E term in Equation 1.10. This means that accelerator experiments are typically more sensitive to the mixing parameters as compared to a natural neutrino source. However, the disadvantage compared to atmospheric neutrino experiments is that the baseline has

351 to be shorter due to the lower flux. Consequently, there is typically less sensitivity to
352 matter effects and the ordering of the neutrino mass eigenstates.

353 A neutrino experiment measures

$$R(\vec{x}) = \Phi(E_\nu) \times \sigma(E_\nu) \times \epsilon(\vec{x}) \times P(\nu_\alpha \rightarrow \nu_\beta), \quad (1.15)$$

354 where $R(\vec{x})$ is the event rate of neutrinos at position \vec{x} , $\Phi(E_\nu)$ is the flux of neutrinos
355 with energy E_ν , $\sigma(E_\nu)$ is the cross-section of the neutrino interaction and $\epsilon(\vec{x})$ is the
356 efficiency of the detector. In order to leverage the most out of an accelerator neutrino
357 experiment, the flux and cross-section systematics need to be constrained. This is
358 typically done via the use of a “near detector”, situated at a baseline of $O(1)$ km. This
359 detector observes the unoscillated neutrino flux and constrains the parameters used
360 within the flux and cross-section model.

361 The first accelerator experiments to precisely measure oscillation parameters were
362 MINOS [56] and K2K [57]. These experiments confirmed the $\nu_\mu \rightarrow \nu_\mu$ oscillations seen
363 in atmospheric neutrino experiments by finding consistent mixing parameter values
364 for $\sin^2(\theta_{23})$ and Δm_{23}^2 . The current generation of accelerator neutrino experiments,
365 T2K and NOvA extended this field by observing $\bar{\nu}_\mu \rightarrow \bar{\nu}_e$ and lead the sensitivity to at-
366 mospheric mixing parameters as seen in Figure 1.6 [58]. The two experiments differ in
367 their peak neutrino energy, baseline, and detection technique. The NOvA experiment
368 is situated at a baseline of 810km from the NuMI beamline which delivers 2GeV neu-
369 trinos. The T2K neutrino beam is peaked around 0.6GeV and propagates 295km. The
370 NOvA experiment also uses functionally identical detectors (near and far) which allow
371 the approximate cancellation of detector systematics whereas T2K uses a plastic scin-
372 tillator technique at the near detector and a water Cherenkov far detector. The future

³⁷³ generation experiments DUNE [59] and Hyper-Kamiokande [60] will succeed these
³⁷⁴ experiments as the high-precision era of neutrino oscillation parameter measurements
³⁷⁵ develops.

³⁷⁶ Several anomalous results have been observed in the LSND [9] and MiniBooNE [10]
³⁷⁷ detectors which were designed with purposefully short baselines. Parts of the neu-
³⁷⁸ trino community attributed these results to oscillations induced by a fourth “sterile”
³⁷⁹ neutrino [61] but several searches in other experiments, MicroBooNE [62] and KAR-
³⁸⁰ MEN [63], found no hints of additional neutrino species. The solution to the anomalous
³⁸¹ results are still being determined.

³⁸² 1.3.4 Reactor Neutrinos

³⁸³ As illustrated in the first discovery of neutrinos (section 1.1), nuclear reactors are a very
³⁸⁴ useful man-made source of electron antineutrinos. For reactors that use low-enriched
³⁸⁵ uranium ^{235}U as fuel, the antineutrino flux is dominated by the β -decay fission of ^{235}U ,
³⁸⁶ ^{238}U , ^{239}Pu and ^{241}Pu [64] as illustrated in Figure 1.7.

³⁸⁷ Due to their low energy, reactor electron antineutrinos predominantly interact
³⁸⁸ via the inverse β -decay (IBD) interaction. The typical signature contains two signals
³⁸⁹ delayed by $O(200)\mu\text{s}$; firstly the prompt photons from positron annihilation, and
³⁹⁰ secondly the photons emitted ($E_{tot}^\gamma = 2.2\text{MeV}$) from de-excitation after neutron capture
³⁹¹ on hydrogen. Searching for both signals improves the detector’s ability to distinguish
³⁹² between background and signal events [66]. Recently, SK included gadolinium dopants
³⁹³ into the ultra-pure water to increase the energy released from the photon cascade to
³⁹⁴ $\sim 8\text{MeV}$ and reduce the time of the delayed signal to $\sim 28\mu\text{s}$.

³⁹⁵ There are many short baseline experiments ($L \sim O(1)\text{km}$) that have measured the
³⁹⁶ $\sin^2(\theta_{13})$ and Δm_{23}^2 oscillation parameters. Daya Bay [67], RENO [68] and Double

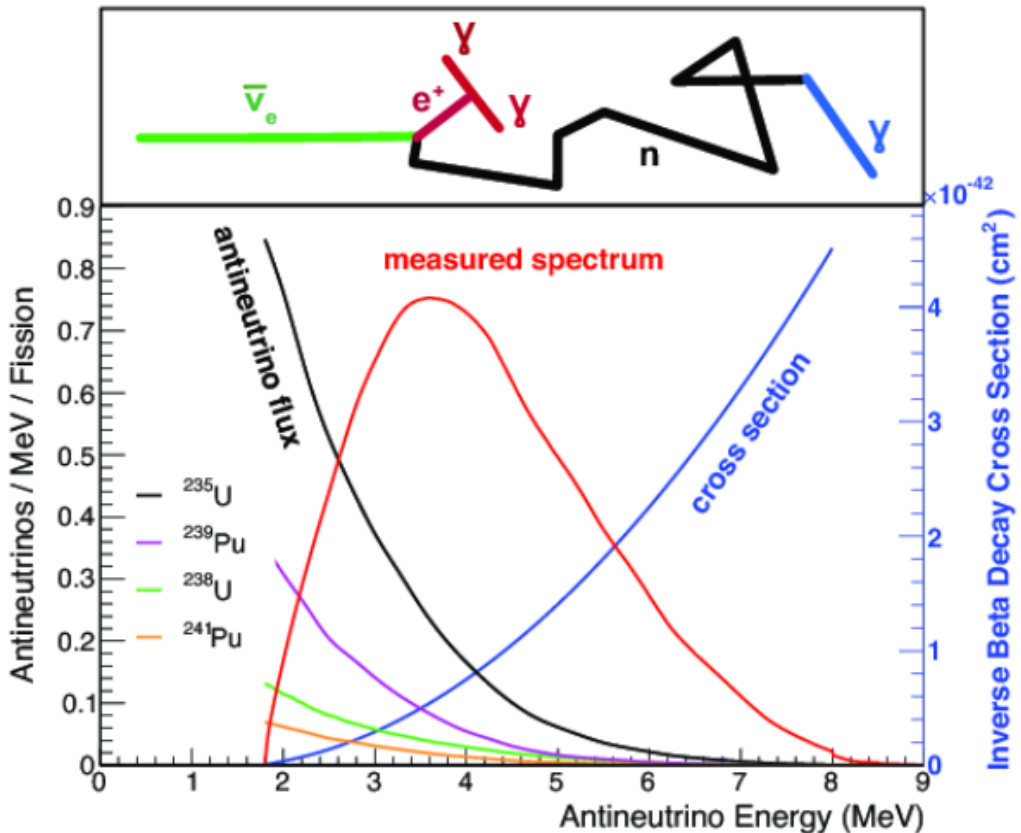


Figure 1.7: Reactor electron antineutrino fluxes for ^{235}U (Black), ^{238}U (Green), ^{239}Pu (Purple), and ^{241}Pu (Orange) isotopes. The inverse β -decay cross-section (Blue) and corresponding measurable neutrino spectrum (Red) are also given. Top panel: Schematic of Inverse β -decay interaction including the eventual capture of the emitted neutron. This capture emits a γ -ray which provides a second signal of the event. Taken from [65].

Chooz [69] have all provided precise measurements, with the first discovery of a non-zero θ_{13} made by Daya Bay and RENO (and complimented by T2K [69]). The constraints on $\sin^2(\theta_{13})$ by the reactor experiments lead the field and are often used as external inputs to accelerator neutrino experiments to improve their sensitivity to δ_{CP} and mass hierarchy determination. JUNO-TAO [70], a small collaboration within the larger JUNO experiment, is a next-generation reactor experiment that aims to precisely measure the isotopic antineutrino yields from the different fission chains. Alongside this, it aims to explain the ‘5MeV excess’ [71–73] by conducting a search for sterile neutrinos with a mass scale of around 1eV.

406 Kamland [74] is the only experiment to have observed reactor neutrinos using a
407 long baseline (flux weighted averaged baseline of $L \sim 180\text{km}$) which allows it to have
408 sensitivity to Δm_{12}^2 . Combined with the SK solar neutrino experiment, the combined
409 analysis puts the most stringent constraint on Δm_{12}^2 [75] which is used as a prior
410 uncertainty within accelerator neutrino experiments.

⁴¹¹ **Chapter 2**

⁴¹² **T2K and SK Experiment Overview**

⁴¹³ As the successor of the Kamiokande experiment, the Super-Kamiokande (SK) collaboration has been leading atmospheric neutrino oscillation analyses for over two decades.
⁴¹⁴ The detector has provided some of the strongest constraints on proton decay limits
⁴¹⁵ and as well as the first precise measurements of the Δm_{23}^2 and $\sin^2(\theta_{23})$ neutrino
⁴¹⁶ oscillation parameters. Despite this, the ability of the detector to low-energy neutrino
⁴¹⁷ events has been significantly improved with the recent gadolinium doping of the
⁴¹⁸ ultra-pure water target. section 2.1 describes the history, detection technique, and
⁴¹⁹ operation of the SK detector.

⁴²¹ The Tokai-to-Kamioka (T2K) experiment was one of the first long-baseline experiments to use both neutrino and antineutrino beams to precisely measure the
⁴²² charge parity violation within the neutrino sector. With the SK detector observing
⁴²³ the oscillated neutrino flux, the T2K experiment observed the first hints of a non-zero
⁴²⁴ $\sin^2(\theta_{13})$ measurement and continues to lead the field with the constraints it provides
⁴²⁵ on $\sin^2(\theta_{13})$, $\sin^2(\theta_{23})$, Δm_{23}^2 and δ_{CP} . section 2.2 documents the techniques
⁴²⁶ which T2K uses in generating its neutrino beam as well as the ‘near-detector’ used to
⁴²⁷ constrain the flux and cross-section parameters invoked within the systematic models.

⁴²⁹ **2.1 The Super-Kamiokande Experiment**

⁴³⁰ The SK experiment began taking data in 1996 [76] and has had many modifications
⁴³¹ throughout its lifespan. There have been seven defined periods of data taking as

noted in Table 2.1. Data taking began in SK-I which ran for five years. Between the SK-I and SK-II periods, a significant proportion of the PMTs were damaged during maintenance. Those that survived were equally distributed throughout the detector in the SK-II era, which resulted in a reduced photo-coverage. From SK-III onwards, repairs to the detector meant the full suite of PMTs was operational. Before the start of SK-IV, the data acquisition and electronic systems were upgraded. Between SK-IV and SK-V, a significant effort was placed into tank open maintenance and repair/replacement of defective PMTs, a task for which the author of this thesis was required. Consequently, the detector conditions were significantly different between the two operational periods. SK-VI saw the start of the 0.01% gadolinium doped water. SK-VII, which started during the writing of this thesis, has increased the gadolinium concentration to 0.03% for continued operation. DB: [Link to Linyan's talk from Nu2022.](#)

Period	Start Date	End Date	Live-time (days)
I	April 1996	July 2001	1489.19
II	October 2002	October 2005	798.59
III	July 2006	September 2008	518.08
IV	September 2008	May 2018	3244.4
V	January 2019	July 2020	461.02
VI	July 2020	May 2022	583.3
VII	May 2022	Ongoing	N/A

Table 2.1: The various SK periods and respective live-time. The SK-VI live-time is calculated until 1st April 2022. SK-VII started during the writing of this thesis.

2.1.1 The SK Detector

The basic structure of the Super-Kamiokande (SK) detector is a cylindrical tank with a diameter 39.3m and height 41.1m filled with ultrapure water [77]. A diagram of the significant components of the SK detector is illustrated in Figure 2.1. The SK detector

is situated in the Kamioka mine in Gifu, Japan. The mine is underground with roughly 1km rock overburden (2.7km water equivalent overburden) [78]. At this depth, the rate of cosmic ray muons is significantly decreased to a value of $\sim 2\text{Hz}$. The top of the tank is covered with stainless steel which is designed as a working platform for maintenance, calibration, and location for high voltage and data acquisition electronics.

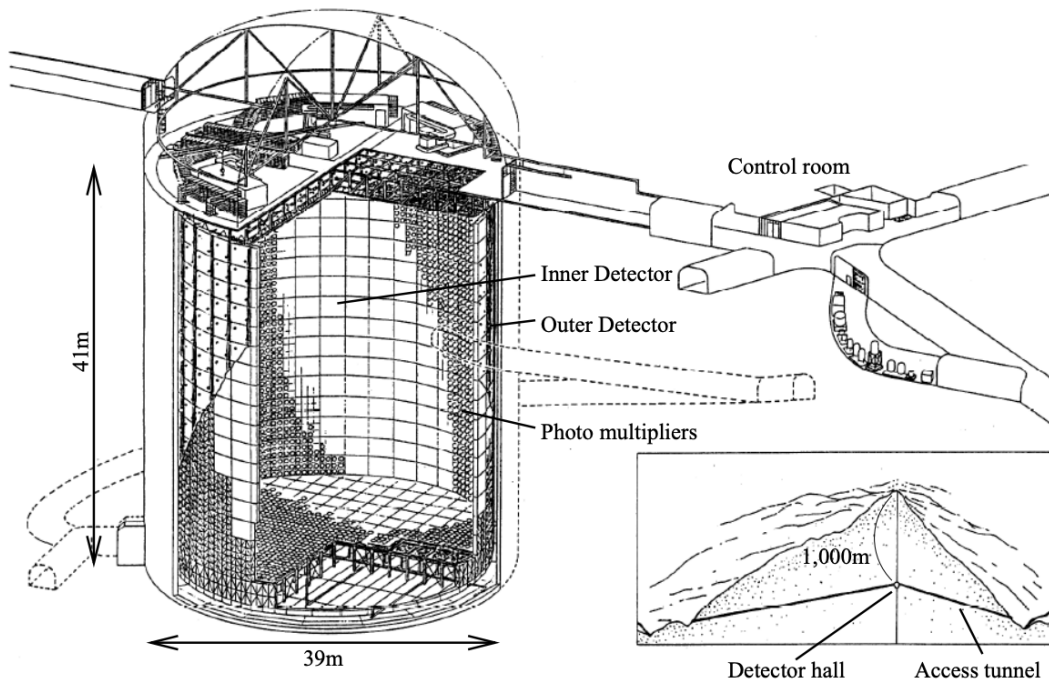


Figure 2.1: A schematic diagram of the Super-Kamiokande Detector. Taken from [79].

A smaller cylindrical structure (36.2m diameter, 33.8m height) is situated inside the tank, with an approximate 2m gap between this structure and the outer tank wall. The purpose of this structure is to support the photomultiplier tubes (PMTs). The volume inside and outside the support structure is referred to as the inner detector (ID) and outer detector (OD), respectively. In the SK-IV era, the ID and OD are instrumented by 11,129 50cm and 1,885 20cm PMTs respectively [77]. The ID contains a 32kton mass of water. Many analyses performed at SK use a “fiducial volume” defined by the volume of water inside the ID excluding some distance to the ID wall. This reduces the volume of the detector which is sensitive to neutrino events but reduces radioactive

⁴⁶³ backgrounds and allows for better reconstruction performance. The nominal fiducial
⁴⁶⁴ volume is defined as the area contained inside 2m from the ID wall for a total of
⁴⁶⁵ 22.5kton water [80].

⁴⁶⁶ The two regions of the detector (ID and OD) are optically separated with opaque
⁴⁶⁷ black plastic. The purpose of this is to determine whether a track entered or exited
⁴⁶⁸ the ID. This allows cosmic ray muons and partially contained events to be tagged and
⁴⁶⁹ separated from neutrino events entirely contained within the ID. This black plastic is
⁴⁷⁰ also used to cover the area between the ID PMTs to reduce photon reflection from the
⁴⁷¹ ID walls. Opposite to this, the OD is lined with a reflective material to allow photons to
⁴⁷² reflect around inside the OD until collected by one of the PMTs. Furthermore, each OD
⁴⁷³ PMT is backed with $50 \times 50\text{cm}$ plates of wavelength shifting acrylic which increases
⁴⁷⁴ the efficiency of light collection [78].

⁴⁷⁵ In the SK-IV data-taking period, the photocathode coverage of the detector, or the
⁴⁷⁶ fraction of the ID wall instrumented with PMTs, is $\sim 40\%$ [78]. The PMTs have a
⁴⁷⁷ quantum efficiency (the ratio of detected electrons to incident photons) of $\sim 21\%$ for
⁴⁷⁸ photons with wavelengths of $360\text{nm} < \lambda < 390\text{nm}$. The proportion of photoelectrons
⁴⁷⁹ that produce a signal in the dynode of a PMT, termed the collection efficiency, is
⁴⁸⁰ $> 70\%$ [78]. The PMTs used within SK are most sensitive to photons with wavelength
⁴⁸¹ $300\text{nm} \leq \lambda \leq 600\text{nm}$ [78]. One disadvantage of using PMTs as the detection media
⁴⁸² is that the Earth's geomagnetic field can modify its response. Therefore, a set of
⁴⁸³ compensation coils is built around the inner surface of the detector to mitigate this
⁴⁸⁴ effect [81].

⁴⁸⁵ As mentioned, the SK detector is filled with ultrapure water, which in a perfect
⁴⁸⁶ world would contain no impurities. However, bacteria and organic compounds can
⁴⁸⁷ significantly degrade the water quality. This decreases the attenuation length which
⁴⁸⁸ reduces the total number of photons that hit a PMT. To combat this, a sophisticated

489 water treatment system has been developed [78, 82]. UV lights, mechanical filters, and
490 membrane degasifiers are used to reduce the bacteria, suspended particulates, and
491 radioactive materials from the water. The flow of water within the tank is also critical
492 as it can remove stagnant bacterial growth or build-up of dust on the surfaces within
493 the tank. Gravity drifts impurities in the water towards the bottom of the tank which,
494 if left uncontrolled, can create asymmetric water conditions between the top and
495 bottom of the tank. Typically, the water entering the tank is cooled below the ambient
496 temperature of the tank to control convection and inhibit bacteria growth. Furthermore,
497 the dark noise hits within PMTs is sensitive to the PMT temperature [83] so controlling
498 the temperature gradients within the tank is beneficial for stable measurements.

499 SK-VI is the first phase of the SK experiment to use gadolinium dopants within
500 the ultrapure water [DB: Link to Linyan's talk at Nu2022](#). As such, the SK water
501 system had to be replaced to avoid removing the gadolinium concentrate from the
502 ultrapure water [84]. For an inverse β -decay (IBD) interaction in a water target, the
503 emitted neutron is thermally captured on hydrogen. This process releases 2.2MeV γ
504 rays which are difficult to detect due to Compton scattered electrons from a γ ray of
505 this energy is very close to the Cherenkov threshold, limiting the number of photons
506 produced. Thermal capture of neutrons on gadolinium generates γ rays with higher
507 energy meaning they are more easily detected. SK-VI has 0.01% Gd loading (0.02%
508 gadolinium sulphate by mass) which causes \approx 50% of neutrons emitted by IBD to
509 be captured on gadolinium [85, 86]. Whilst predominantly useful for low energy
510 analyses, Gd loading allows better $\nu/\bar{\nu}$ separation for atmospheric neutrino event
511 selections [87]. Efforts are currently in place to increase the gadolinium concentrate to
512 0.03% for \approx 75% neutron capture efficiency on gadolinium [DB: Link to Mark's talk at](#)
513 [Nu2022](#). The final stage of loading targets 0.1% concentrate.

514 2.1.2 Calibration

515 The calibration of the SK detector is documented in [77] and summarised below. The
516 analysis presented within this thesis is dependent upon ‘high energy events’ (Charged
517 particles with $O(> 100)\text{MeV}$ momenta). These are events that are expected to generate
518 a larger number of photons such that each PMT will be hit with multiple photons.
519 The reconstruction of these events depends upon the charge deposited within each
520 PMT and the timing response of each individual PMT. Therefore, the most relevant
521 calibration techniques to this thesis are outlined.

522 Before installation, 420 PMTs were calibrated to have identical charge responses
523 and then distributed throughout the tank in a cross-shape pattern (As illustrated by
524 Figure 2.2). These are used as a standardised measure for the rest of the PMTs installed
525 at similar geometric positions within SK to be calibrated against. To perform this
526 calibration, a xenon lamp is located at the center of the SK tank which flashes uniform
527 light at 1Hz. This allows for geometrical effects, water quality variation, and timing
528 effects to be measured in-situ throughout normal data-taking periods.

529 When specifically performing calibration of the detector (in out-of-data taking
530 mode), the water in the tank was circulated to avoid top/bottom asymmetric water
531 quality. Any non-uniformity within the tank significantly affects the PMT hit proba-
532 bility through scattering or absorption. This becomes a dominant effect for the very
533 low-intensity light sources discussed later which are designed such that only one
534 photon is incident upon a given PMT.

535 The “gain” of a PMT is defined as the ratio of the total charge of the signal produced
536 compared to the charge of photoelectrons emitted by the photocathodes within the
537 PMT. To calibrate the signal of each PMT, the “relative” and “absolute” gain values are

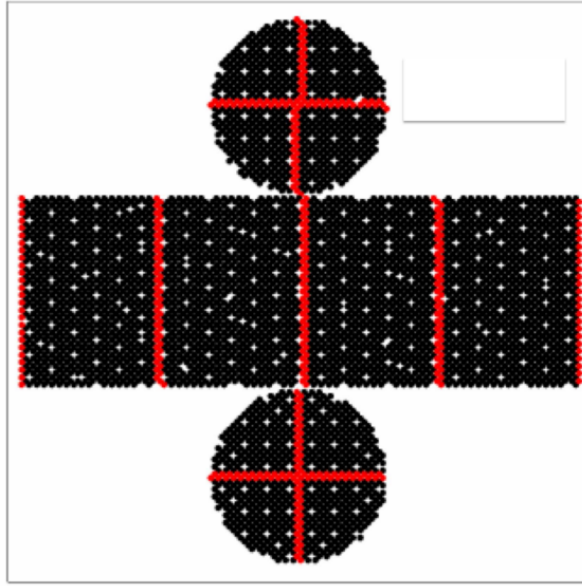


Figure 2.2: The location of “standard PMTs” (red) inside the SK detector. Taken from [77].

538 measured. The relative gain is the variation of gain among each of the PMTs whereas
 539 the absolute gain is the average gain of all PMTs.

540 The relative gain is calibrated as follows. A laser is used to generate two measure-
 541 ments; a high-intensity flash that illuminates every PMT with a sufficient number of
 542 photons, and a low-intensity flash in which only a small number of PMTs collect light.
 543 The first measurement creates an average charge, $Q_{obs}(i)$ on PMT i , whereas the second
 544 measurement ensures that each hit PMT only generates a single photoelectron. For the
 545 low-intensity measurement, the number of times each PMT records a charge larger
 546 than 1/4 photoelectrons, $N_{obs}(i)$, is counted. The values measured can be expressed as

$$\begin{aligned} Q_{obs}(i) &\propto I_H \times f(i) \times \epsilon(i) \times G(i), \\ N_{obs}(i) &\propto I_L \times f(i) \times \epsilon(i), \end{aligned} \tag{2.1}$$

547 Where I_H and I_L is the intensity of the high and low flashes, $f(i)$ is the acceptance
 548 efficiency of the i^{th} PMT, $\epsilon(i)$ is the product of the quantum and collection efficiency

549 of the i^{th} PMT and $G(i)$ is the gain of the i^{th} PMT. The relative gain for each PMT can
550 determined by taking the ratio of these quantities.

551 The absolute gain calibration is performed by observing fixed energy γ -rays of
552 $E_{\gamma} \sim 9\text{MeV}$ emitted isotropically from neutron capture on a NiCf source situated at
553 the center of the detector. This generates a photon yield of about 0.004 photoelec-
554 trons/PMT/event, meaning that $> 99\%$ of PMT signals are generated from single
555 photoelectrons. A charge distribution is generated by performing this calibration over
556 all PMTs, and the average value of this distribution is taken to be the absolute gain
557 value.

558 As mentioned in subsection 2.1.1, the average quantum and collection efficiency
559 for the SK detector is $\sim 21\%$ and $> 70\%$ respectively. However, these values do differ
560 between each PMT and need to be calibrated accordingly. Consequently, the NiCf
561 source is also used to calibrate the “quantum \times collection” efficiency (denoted “QE”)
562 value of each PMT. The NiCf low-intensity source is used as the PMT hit probability
563 is proportional to the QE ($N_{\text{obs}}(i) \propto \epsilon(i)$ in Equation 2.1). A Monte Carlo prediction
564 which includes photon absorption, scattering, and reflection is made to estimate the
565 number of photons incident on each PMT and the ratio of the number of predicted
566 to observed hits is calculated. The difference is attributed to the QE efficiency of that
567 PMT. This technique is extended to calculate the relative QE efficiency by normalizing
568 the average of all PMTs which removes the dependence on the light intensity.

569 Due to differing cable lengths and readout electronics, the timing response between
570 a photon hitting the PMT and the signal being captured by the data acquisition can be
571 different between each PMT. Due to threshold triggers (Described in subsection 2.1.3),
572 the time at which a pulse reaches a threshold is dependent upon the size of the pulse.
573 This is known as the ‘time-walk’ effect and also needs to be accounted for in each PMT.
574 To calibrate the timing response, a pulse of light with width 0.2ns is emitted into the

575 detector through a diffuser Two-dimensional distributions of time and pulse height
576 (or charge) are made for each PMT and are used to calibrate the timing response. This
577 is performed in-situ whilst data taking with the light source pulsing at 0.03Hz.

578 The top/bottom water quality asymmetry is measured using the NiCf calibration
579 data and cross-referencing these results to the “standard PMTs”. The water attenuation
580 length is continuously measured by the rate of vertically-downgoing cosmic-ray
581 muons which enter via the top of the tank.

582 2.1.3 Data Acquisition and Triggering

583 Dark noise is the phenomenon where a PMT registers a pulse that is consistent with a
584 single photoelectron emitted from photon detection despite the PMT being in complete
585 darkness. This is predominately caused by two processes. Firstly there is intrinsic
586 dark noise which is where photoelectrons gain enough thermal energy to be emitted
587 from the photocathode, and secondly, the radioactive decay of contaminants inside the
588 structure of the PMT. Typical dark noise rate for PMTs used within SK are $O(3)$ kHz [78]
589 which equates to about 12 dark noise hits per 220ns [88]. This is lower than the
590 expected number of photons generated for a ‘high energy event’ (As described in
591 subsection 2.1.4) but instability in this value can cause biases in reconstruction.

592 The analysis presented in this thesis only uses the SK-IV period of the SK exper-
593 iment so this subsection focuses on the relevant points of the data acquisition and
594 triggering systems to that SK period. The earlier data acquisition and triggering
595 systems are documented in [89, 90].

596 Before the SK-IV period started, the existing front-end electronics were replaced
597 with “QTC-Based Electrons with Ethernet, QBEE” systems [91]. When the QBEE
598 observes a signal above a 1/4 photoelectron threshold, the charge-to-time (QTC)

599 converter generates a rectangular pulse. The start of the rectangular pulse indicates
 600 the time at which the analog photoelectron signal was received and the width of the
 601 pulse indicates the total charge integrated throughout the signal. This is then digitized
 602 by time-to-digital converters and sent to the “front-end” PCs. The digitized signal
 603 from every QBEE is then chronologically ordered and sent to the “merger” PCs. It is
 604 the merger PCs that apply the software trigger. Any triggered events are passed to the
 605 “organizer” PC. This sorts the data stream of multiple merger PCs into chronologically
 606 ordered events which are then saved to disk. The schematic of data flow from PMTs to
 607 disk is illustrated in Figure 2.3.

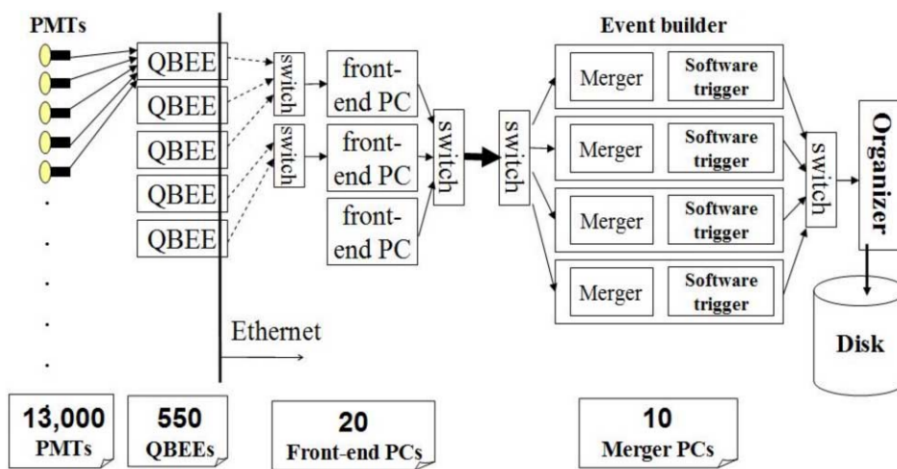


Figure 2.3: Schematic view of the data flow through the data acquisition and online system.
 Taken from [92].

608 The software trigger (described in [93]) operates by determining the number of
 609 PMT hits within a 200ns sliding window, N_{200} , coincides with the maximum time that
 610 a Cherenkov photon would take to traverse the length of the SK tank [90]. For lower
 611 energy events that generate fewer photons, this technique is useful for eliminating
 612 background processes like dark noise and radioactive decay which would be expected
 613 to separate in time. When the value of N_{200} exceeds some threshold, a software trigger
 614 is issued. There are several trigger thresholds used within the SK-IV period which are
 615 detailed in Table 2.2. If one of these thresholds is met, the PMT hits within an extended

time window are also read out and saved to disk. In the special case of an event that exceeds the SHE trigger but does not exceed the OD trigger, the AFT trigger looks for delayed coincidences of 2.2MeV gamma rays emitted from neutron capture in a $535\mu\text{s}$ window after the SHE trigger. A similar but more complex “Wideband Intelligent Trigger (WIT)” has been deployed and is described in [88].

Trigger	Acronym	Condition	Extended time window (μs)
Super Low Energy	SLE	>34/31 hits	1.3
Low Energy	LE	>47 hits	40
High Energy	HE	>50 hits	40
Super High Energy	SHE	>70/58 hits	40
Outer Detector	OD	>22 hits in OD	N/A

Table 2.2: The trigger thresholds and extended time windows saved around an event which were utilised throughout the SK-IV period. The exact thresholds can change and the values listed here represent the thresholds at the start and end of the SK-IV period.

2.1.4 Cherenkov Radiation

Cherenkov light is emitted from any highly energetic charged particle traveling with relativistic velocity, β , greater than the local speed of light in a medium [94]. Cherenkov light is formed at the surface of a cone with characteristic pitch angle,

$$\cos(\theta) = \frac{1}{\beta n}. \quad (2.2)$$

where n is the refractive index of the medium. Consequently, the Cherenkov momentum threshold, P_{thres} , is dependent upon the mass, m , of the charged particle moving through the media,

$$P_{thres} = \frac{m}{\sqrt{n^2 - 1}} \quad (2.3)$$

628 For water, where $n = 1.33$, the Cherenkov threshold momentum and energy for
 629 various particles are given in Table 2.3. In contrast, γ -rays are detected indirectly via
 630 the combination of photons generated by Compton scattering and pair production.
 631 The threshold for detection in the SK detector is typically higher than the threshold
 632 for photon production. This is due to the fact that the attenuation of photons in the
 633 water means that typically $\sim 75\%$ of Cherenkov photons reach the ID PMTs. Then the
 634 collection and quantum efficiencies described in subsection 2.1.1 result in the number
 635 of detected photons being lower than the number of photons which reach the PMTs.

Particle	Threshold Momentum (MeV)	Threshold Energy (MeV)
Electron	0.5828	0.7751
Muon	120.5	160.3
Pion	159.2	211.7
Proton	1070.0	1423.1

Table 2.3: The threshold momentum and energy for a particle to generate Cherenkov light in ultrapure water, as calculated in Equation 2.2 in ultrapure water which has refractive index $n = 1.33$.

636 The Frank-Tamm equation [95] describes the relationship between the number of
 637 Cherenkov photons generated per unit length, dN/dx , the wavelength of the photons
 638 generated, λ , and the relativistic velocity of the charged particle,

$$\frac{d^2N}{dxd\lambda} = 2\pi\alpha \left(1 - \frac{1}{n^2\beta^2}\right) \frac{1}{\lambda^2}. \quad (2.4)$$

where α is the fine structure constant. For a 100MeV momentum electron, approximately 330 photons will be produced per centimeter in the $300\text{nm} \leq \lambda \leq 700\text{nm}$ region which the ID PMTs are most sensitive to [78].

2.2 The Tokai to Kamioka Experiment

The Tokai to Kamioka (T2K) experiment is a long-baseline neutrino oscillation experiment located in Japan. Proposed in the early 2000s [96, 97] to replace K2K [98], T2K was designed to observe electron neutrino appearance whilst precisely measuring the oscillation parameters associated with muon neutrino disappearance [99]. The experiment consists of a neutrino beam generated at the Japan Proton Accelerator Research Complex (J-PARC), a suite of near detectors situated 280m from the beam target, and the Super Kamiokande far detector positioned at a 295km baseline. The cross-section view of the T2K experiment is drawn in Figure 2.4.

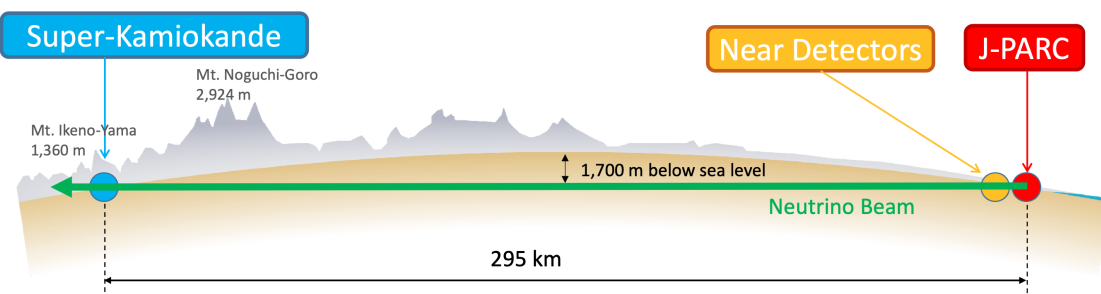


Figure 2.4: The cross-section view of the Tokai to Kamioka experiment illustrating the beam generation facility at J-PARC, the near detector situated at a baseline of 280m and the Super Kamiokande far detector situated 295km from the beam target.

The T2K collaboration makes world-leading measurements of the $\sin^2(\theta_{23})$, Δm_{23}^2 , and δ_{CP} oscillation parameters. Improvements in the precision and accuracy of parameter estimates are still being made by including new data samples and developing the models which describe the neutrino interactions and detector responses [DB: Link](#) to Christophe's slides from Nu2022. Electron neutrino appearance was first observed

656 at T2K in 2014 [100] which accompanied a 7.3σ significance of a non-zero $\sin^2(\theta_{13})$
 657 measurement.

658 The near detectors provide constraints on the beam flux and cross-section model
 659 parameters used within the fit by observing the unoscillated neutrino beam. There
 660 are a host of detectors situated in the near detector hall (As illustrated in Figure 2.5);
 661 ND280 (subsection 2.2.2), INGRID (subsection 2.2.3), NINJA [101], WAGASCI [102],
 662 and Baby-MIND [103]. The latter three are not currently used within the oscillation
 663 analysis presented within this thesis.

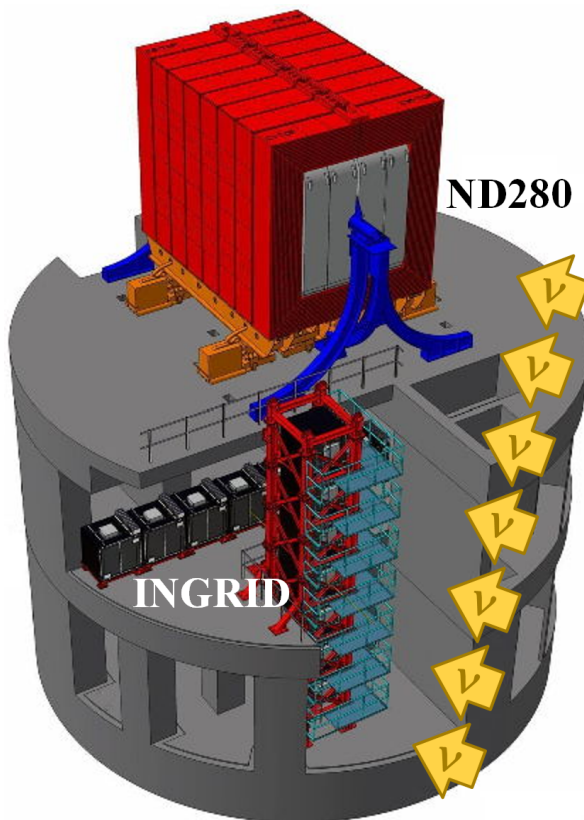


Figure 2.5: The near detector suite for the T2K experiment showing the ND280 and INGRID detectors. The distance between the detectors and the beam target is 280m.

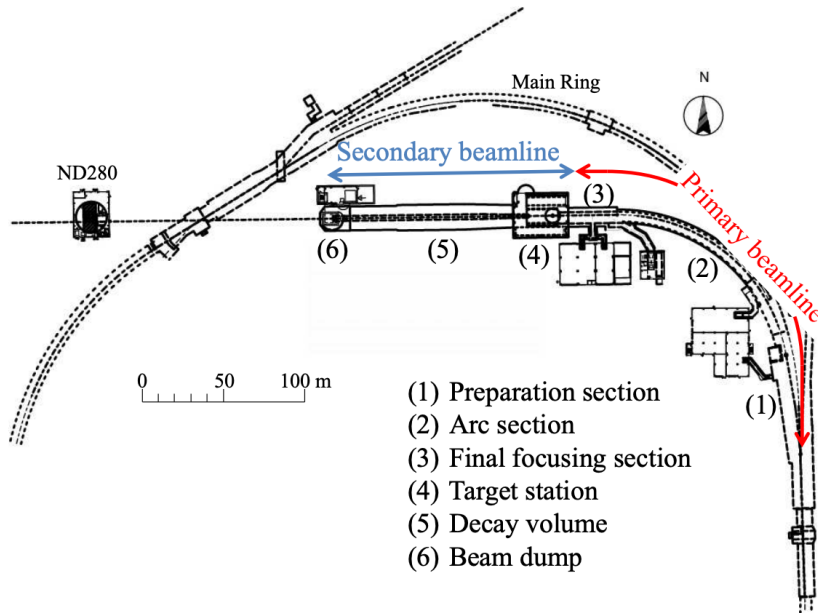
664 Whilst this thesis presents the ND280 in terms of its purpose for the oscillation
 665 analysis, the detector can also make many cross-section measurements at neutrino
 666 energies of $O(1)\text{GeV}$ for the different targets within the detector [104, 105]. These

667 measurements are of equal importance as they can lead the way in determining the
668 model parameters used in the interaction models for the future high-precision era of
669 neutrino physics.

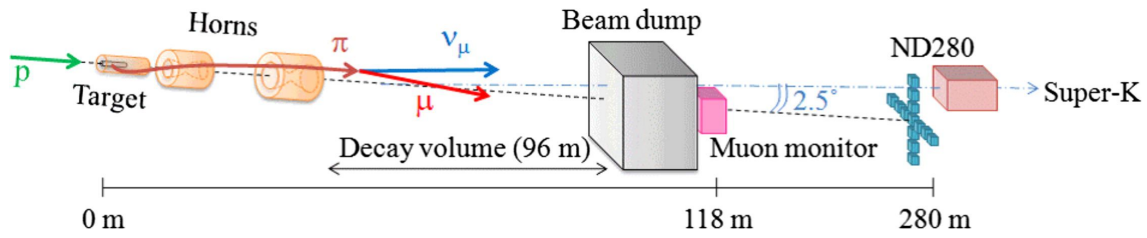
670 2.2.1 The Neutrino Beam

671 The neutrino beam used within the T2K experiment is described in [55, 106] and
672 summarised below. The accelerating facility at J-PARC is composed of two sections; the
673 primary and secondary beamlines. Figure 2.6 illustrates a schematic of the beamline,
674 focusing mostly on the components of the secondary beamline. The primary beamline
675 has three accelerators that progressively accelerate protons; a linear accelerator, a rapid-
676 cycling synchrotron, and the main-ring (MR) synchrotron. Once fully accelerated by
677 the MR, the protons have a kinetic energy of 30GeV. Eight bunches of these protons,
678 separated by 500ns, are extracted per “spill” from the MR and directed towards a
679 graphite target (A rod of length 91.4cm and diameter 2.6cm). Spills are extracted at
680 0.5Hz with $\sim 3 \times 10^{14}$ protons contained per spill.

681 The secondary beamline consists of three main components; the target station, the
682 decay volume, and the beam dump. The target station is comprised of the target, beam
683 monitors, and three magnetic focusing horns. The proton beam interacts with the
684 graphite target to form a secondary beam of mostly pions and kaons. The secondary
685 beam travels through a 96m long decay volume, generating neutrinos through the
686 following decays [55],



(a) Primary and secondary beamline



(b) Secondary beamline

Figure 2.6: Top panel: Bird's eye view of the most relevant part of primary and secondary beamline used within the T2K experiment. The primary beamline is the main-ring proton synchrotron, kicker magnet, and graphite target. The secondary beamline consists of the three focusing horns, decay volume, and beam dump. Figure taken from [106]. Bottom panel: The side-view of the secondary beamline including the focusing horns, beam dump and neutrino detectors. Figure taken from [107].

$$\begin{array}{ll}
 \pi^+ \rightarrow \mu^+ + \nu_\mu & \pi^- \rightarrow \mu^- + \bar{\nu}_\mu \\
 K^+ \rightarrow \mu^+ + \nu_\mu & K^- \rightarrow \mu^- + \bar{\nu}_\mu \\
 \rightarrow \pi^0 + e^+ + \nu_e & \rightarrow \pi^0 + e^- + \bar{\nu}_e \\
 \rightarrow \pi^0 + \mu^+ + \nu_\mu & \rightarrow \pi^0 + \mu^- + \bar{\nu}_\mu \\
 K_L^0 \rightarrow \pi^- + e^+ + \nu_e & K_L^0 \rightarrow \pi^+ + e^- + \bar{\nu}_e \\
 \rightarrow \pi^- + \mu^+ + \nu_\mu & \rightarrow \pi^+ + \mu^- + \bar{\nu}_\mu \\
 \mu^+ \rightarrow e^+ + \bar{\nu}_\mu + \nu_e & \mu^- \rightarrow e^- + \nu_\mu + \bar{\nu}_e
 \end{array}$$

The electrically charged component of the secondary beam is focused towards the far detector by the three magnetic horns. These horns direct charged particles of a particular polarity towards SK whilst defocusing the oppositely charged particles. This allows a mostly neutrino or mostly antineutrino beam to be used within the experiment, denoted as “forward horn current (FHC)” or “reverse horn current (RHC)” respectively.

Figure 2.7 illustrates the different contributions to the FHC and RHC neutrino flux.

The low energy flux is dominated by the decay of pions whereas kaon decay becomes the dominant source of neutrinos for $E_\nu > 3\text{GeV}$. The “wrong-sign” component, which is the $\bar{\nu}_\mu$ background in a ν_μ beam, and the intrinsic irreducible ν_e background are predominantly due to muon decay for $E_\nu < 2\text{GeV}$. As the antineutrino cross-section is smaller than the neutrino cross-section, the wrong-sign component is more dominant in the RHC beam as compared to that in the FHC beam.

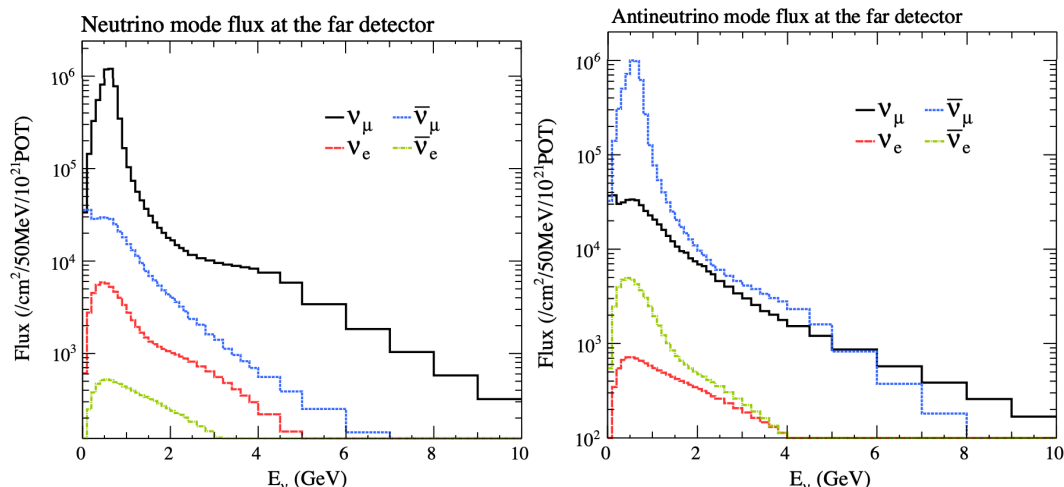


Figure 2.7: The Monte Carlo prediction of the energy spectrum for each flavour of neutrino (ν_e , $\bar{\nu}_e$, ν_μ and $\bar{\nu}_\mu$) in the neutrino dominated beam FHC mode (Left) and antineutrino dominated beam RHC mode (Right) expected at SK. Taken from [108].

The beam dump, situated at the end of the decay volume, stops all charged particles other than highly energetic muons ($p_\mu > 5\text{GeV}$). The MuMon detector monitors the

⁷⁰³ penetrating muons to determine the beam direction and intensity which is used to
⁷⁰⁴ constrain some of the beam flux systematics within the analysis [107, 109].

⁷⁰⁵ The T2K experiment uses an off-axis beam to narrow the neutrino energy distribu-
⁷⁰⁶ tion. This was the first implementation of this technique in a long-baseline neutrino
⁷⁰⁷ oscillation experiment after its original proposal [110]. Pion decay, $\pi \rightarrow \mu + \nu_\mu$, is a
⁷⁰⁸ two-body decay. Consequently, the neutrino energy, E_ν , can be determined based on
⁷⁰⁹ the pion energy, E_π , and the angle at which the neutrino is emitted, θ ,

$$E_\nu = \frac{m_\pi^2 - m_\mu^2}{2(E_\pi - p_\pi \cos(\theta))}, \quad (2.5)$$

⁷¹⁰ where m_π and m_μ are the mass of the pion and muon respectively. For a fixed
⁷¹¹ energy pion, the neutrino energy distribution is dependent upon the angle at which
⁷¹² the neutrinos are observed from the initial pion beam direction. For the 295km
⁷¹³ baseline at T2K, $E_\nu = 0.6\text{GeV}$ maximises the electron neutrino appearance probability,
⁷¹⁴ $P(\nu_\mu \rightarrow \nu_e)$, whilst minimising the muon disappearance probability, $P(\nu_\mu \rightarrow \nu_\mu)$.
⁷¹⁵ Figure 2.8 illustrates the neutrino energy distribution for a range of off-axis angles, as
⁷¹⁶ well as the oscillation probabilities most relevant to T2K.

⁷¹⁷ 2.2.2 The Near Detector at 280m

⁷¹⁸ Whilst all the near detectors are situated in the same “pit” located at 280m from the
⁷¹⁹ beamline, the “ND280” detector is the off-axis detector which is situated at the same
⁷²⁰ off-axis angle as the Super-Kamiokande far detector. It has two primary functions;
⁷²¹ firstly it measures the neutrino flux and secondly it counts the event rates of different
⁷²² types of neutrino interactions. Both of these constrain the flux and cross-section

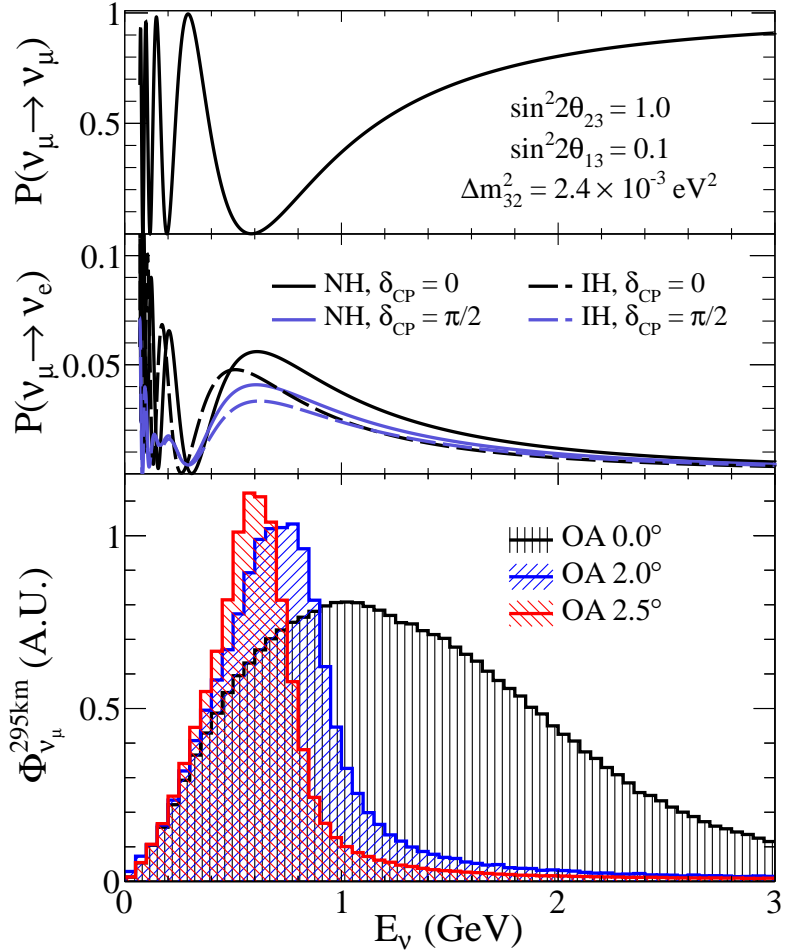


Figure 2.8: Top panel: T2K muon neutrino disappearance probability as a function of neutrino energy. Middle panel: T2K electron neutrino appearance probability as a function of neutrino energy. Bottom panel: The neutrino flux distribution for three different off-axis angles (Arbitrary units) as a function of neutrino energy.

systematics invoked within the model for a more accurate prediction of the expected event rate at the far detector.

As illustrated in Figure 2.9, the ND280 detector consists of several sub-detectors. The most important part of the detector for this analysis is the tracker region. This is comprised of two time projection chambers (TPCs) sandwiched between three fine grain detectors (FGDs). The FGDs contain both hydrocarbon plastics and water targets for neutrino interactions and provide track reconstruction near the interaction vertex. The emitted charged particles can then propagate into the TPCs which provide particle identification and momentum reconstruction. The FGDs and TPCs are

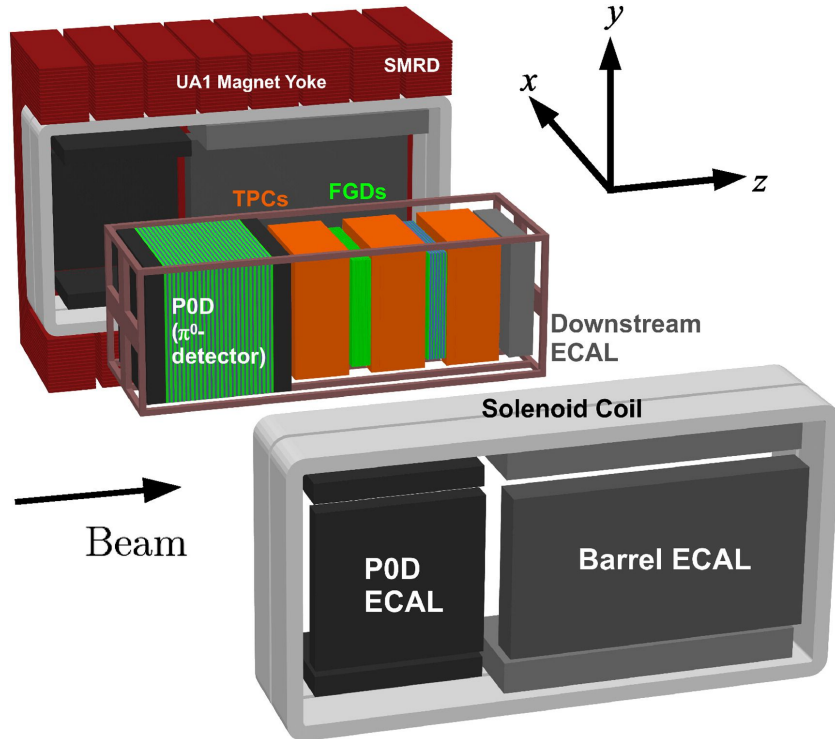


Figure 2.9: The components of the ND280 detector. The neutrino beam travels from left to right. Taken from [106].

732 further described in subsubsection 2.2.2.1 and subsubsection 2.2.2.2 respectively. The
 733 electromagnetic calorimeter (ECAL) encapsulates the tracker region alongside the π^0
 734 detector (P0D). The ECAL measures the deposited energy from photons emitted from
 735 interactions within the FGD. The P0D constrains the cross-section of neutral current
 736 interactions which generate neutral pions, which is one of the largest backgrounds in
 737 the electron neutrino appearance oscillation channel. The P0D and ECAL detectors
 738 are detailed in subsubsection 2.2.2.3 and subsubsection 2.2.2.4 respectively. The entire
 739 detector is located within a large yolk magnet which produces a 0.2T magnetic field.
 740 This design of the magnet also includes a scintillating detector called the side muon
 741 range detector (SMRD) which is used to track high-angle muons as well as acting as a
 742 cosmic veto. The SMRD is described in subsubsection 2.2.2.5.

⁷⁴³ **2.2.2.1 Fine Grained Detectors**

⁷⁴⁴ The T2K tracker region is comprised of two fine grained detectors (FGD) and three
⁷⁴⁵ Time Projection Chambers (TPC). A detailed description of the FGD design, construc-
⁷⁴⁶ tion, and assembly is found in [111] and summarised below. The FGDs are the primary
⁷⁴⁷ target for neutrino interactions with a mass of 1.1 tonnes per FGD. Alongside this,
⁷⁴⁸ the FGDs are designed to be able to track short-range particles which do not exit the
⁷⁴⁹ FGD. Typically, short-range particles are low momentum and are observed as tracks
⁷⁵⁰ that deposit a large amount of energy per unit length. This means the FGD needs
⁷⁵¹ good granularity to resolve these particles. The FGDs have the best timing resolution
⁷⁵² ($\sim 3\text{ns}$) of any of the sub-detectors of the ND280 detector. As such, the FGDs are
⁷⁵³ used for time of flight measurements to determine forward going positively charged
⁷⁵⁴ particles from backward going negatively charged particles. Finally, any tracks which
⁷⁵⁵ pass through multiple sub-detectors are required to be track matched to the FGD.

⁷⁵⁶ Both FDGs are made from square scintillator planes of side length 186cm and width
⁷⁵⁷ 2.02cm. Each plane consists of two layers of 192 scintillator bars in an XY orientation.
⁷⁵⁸ A wave-length shift fiber is threaded through the center of each bar and is read out by
⁷⁵⁹ a multi-photon pixel counter (MPPC). FGD1 is the most upstream of the two FGDs
⁷⁶⁰ and contains 15 planes of carbon plastic scintillator which is a common target in
⁷⁶¹ external neutrino scattering data. As the far detector is a pure water target, 7 of the 15
⁷⁶² scintillator planes in FGD2 have been replaced with a hybrid water-scintillator target.
⁷⁶³ Due to the complexity of the nucleus, nuclear effects can not be extrapolated between
⁷⁶⁴ different nuclei. Therefore having the ability to take data on one target which is the
⁷⁶⁵ same as external data and another target which is the same as the far detector target is
⁷⁶⁶ beneficial for reliable model parameter estimates.

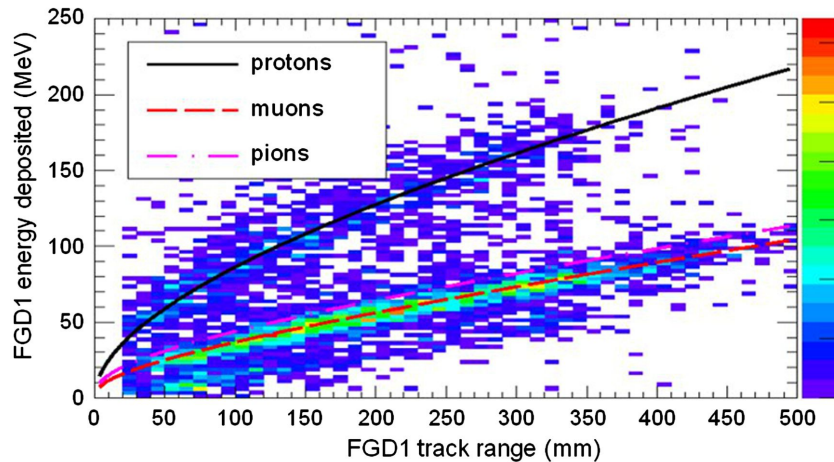


Figure 2.10: Comparison of data to Monte Carlo prediction of integrated deposited energy as a function of track length for particles that stopped in FGD1. Taken from [111].

The integrated deposited energy is used for particle identification. The FGD can distinguish protons from other charged particles by comparing the integrated deposited energy from data to Monte Carlo prediction as seen in Figure 2.10.

2.2.2.2 Time Projection Chambers

The majority of particle identification and momentum measurements within ND280 are provided by three Time Projection Chambers (TPCs) [112]. The TPCs are located on either side of the FGDs. They are located inside of the magnetic field meaning the momentum of a charged particle can be determined from the bending of the track.

Each TPC module consists of two gas-tight boxes, as shown in Figure 2.11, which are made of non-magnetic material. The outer box is filled with CO₂ which acts as an electrical insulator between the inner box and the ground. The inner box forms the field cage which produces a uniform electric drift field of $\sim 275\text{V/cm}$ and an argon gas mixture. Charged particles moving through this gas mixture ionize the gas mixture. The ionised charge is drifted towards micromega detectors which measure the ionization charge. The time and position information in the readout allows a three-dimensional image of the neutrino interaction.

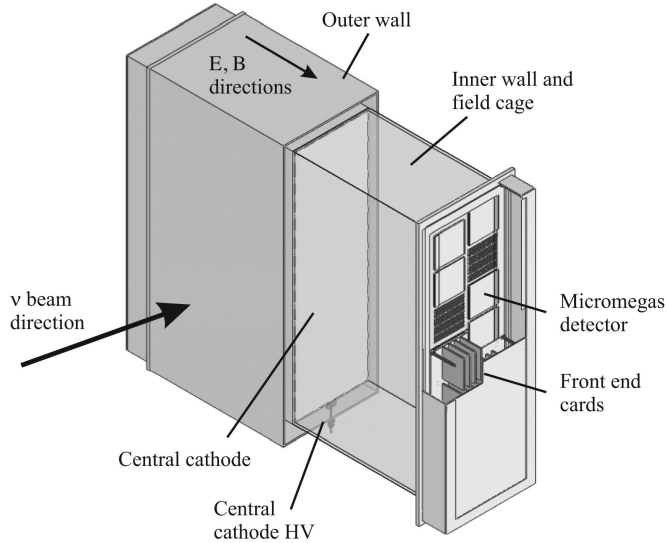


Figure 2.11: Schematic design of a Time Projection Chamber detector. Taken from [112].

The particle identification of tracks that pass through the TPCs is performed using

dE/dx measurements. Figure 2.12 illustrates the data to Monte Carlo distributions of the energy lost by a charged particle passing through the TPC as a function of the reconstructed particle momentum. The resolution is $7.8 \pm 0.2\%$ meaning that electrons and muons can be distinguished. This allows reliable measurements of the intrinsic ν_e component of the beam.

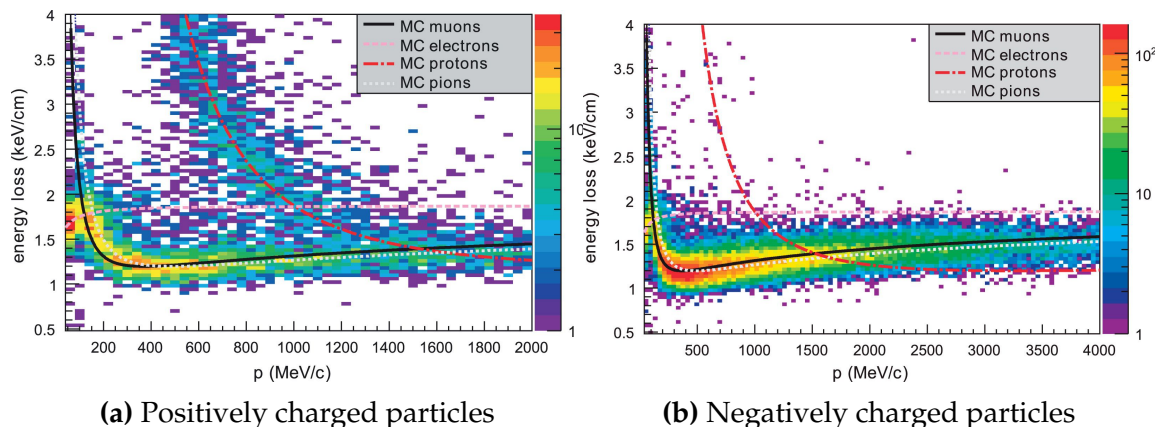


Figure 2.12: The distribution of energy loss as a function of reconstructed momentum for charged particles passing through the TPC, comparing data to Monte Carlo prediction. Taken from [112].

⁷⁸⁹ **2.2.2.3 π^0 Detector**

⁷⁹⁰ If one of the γ -rays from a $\pi^0 \rightarrow 2\gamma$ decay is missed at the far detector, the reconstruc-
⁷⁹¹ tion will determine that event to be electron-like. This is one of the main backgrounds
⁷⁹² hindering the electron neutrino appearance searches. Therefore, the π^0 detector (P0D)
⁷⁹³ measures the cross-section of the neutral current induced neutral pion production on
⁷⁹⁴ a water target.

⁷⁹⁵ The P0D is a cube of approximately 2.5m length. The P0D consists of layers of
⁷⁹⁶ scintillating bars, brass and lead sheets, and water bags as illustrated in Figure 2.13.
⁷⁹⁷ Two electromagnetic calorimeters are positioned at the most upstream and most
⁷⁹⁸ downstream position in the sub-detector and the water target is situated in between
⁷⁹⁹ them. The scintillator layers are built from two triangular bars orientated in opposite
⁸⁰⁰ directions to form a rectangular layer. Each triangular scintillator bar is threaded with
⁸⁰¹ optical fiber which is read out by MPPCs. The high-Z brass and lead regions produce
⁸⁰² electron showers from the photons emitted in π^0 decay.

⁸⁰³ The sub-detector can generate measurements of NC1 π^0 cross-sections on a water
⁸⁰⁴ target by measuring the event rate both with and without the water target, with the
⁸⁰⁵ cross-section on a water target being determined as the difference. The total active
⁸⁰⁶ mass is 16.1 tonnes when filled with water and 13.3 tonnes when empty.

⁸⁰⁷ **2.2.2.4 Electromagnetic Calorimeter**

⁸⁰⁸ The electromagnetic calorimeter [114] (ECal) encapsulates the P0D and tracking sub-
⁸⁰⁹ detectors. Its primary purpose is to aid π^0 reconstruction from any interaction in
⁸¹⁰ the tracker. To do this, it measures the energy and direction of photon showers from
⁸¹¹ $\pi^0 \rightarrow 2\gamma$ decay. It can also distinguish pion and muon tracks depending on the shape
⁸¹² of the photon shower deposited.

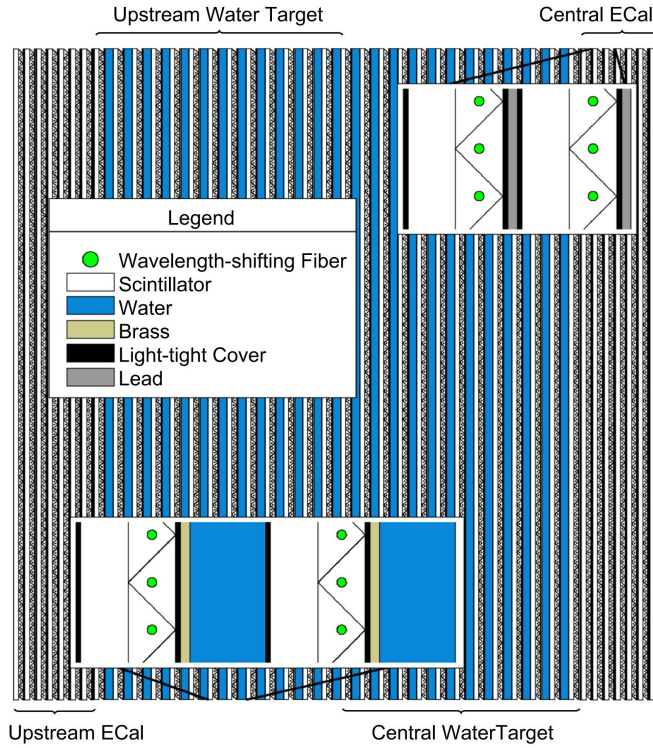


Figure 2.13: A schematic of the P0D side-view. Taken from [113].

The ECal is comprised of three sections; the P0D ECal which surrounds the P0D, the barrel ECal which encompasses the tracking region, and the downstream ECal which is situated downstream of the tracker region. The barrel and downstream ECals are tracking calorimeters that focus on electromagnetic showers from high-angle particles emitted from the tracking sub-detectors. Particularly in the TPC, high-angle tracks (those which travel perpendicularly to the beam-axis) can travel along a single scintillator bar resulting in very few hits. The width of the barrel and downstream ECal corresponds to ~ 11 electron radiation lengths to ensure $\sim 50\%$ of the energy of the π^0 is contained. As the P0D has its own calorimetry which reconstructs showers, the P0D ECal determines the energy which escapes the P0D.

Each ECal is constructed of multiple layers of scintillating bars sandwiched between lead sheets. The scintillating bars are threaded with optical fiber and read out by MPPCs. Each sequential layer of the scintillator is orientated perpendicular to the previous which allows a two-dimensional readout, which when temporal information

⁸²⁷ is included results in three-dimension event displays. The target mass of the P0D ECal,
⁸²⁸ barrel ECal, and downstream ECal are 1.50, 4.80 and 6.62 tonnes respectively.

⁸²⁹ **2.2.2.5 Side Muon Range Detector**

⁸³⁰ As illustrated in Figure 2.9, the ECal, FGDs, P0D, and TPCs are enclosed within the
⁸³¹ UA1 magnet. Originally designed for the NOMAD [115] experiment and reconditioned
⁸³² for use in the T2K experiment [116], the UA1 magnet provides a uniform horizontal
⁸³³ magnetic field of $0.2 \pm 2 \times 10^{-4}$ T.

⁸³⁴ Built into the UA1 magnet, the side muon range detector (SMRD) [117] monitors
⁸³⁵ high-energy muons which leave the tracking region and permeate through the ECal.
⁸³⁶ It additionally acts as a cosmic muon veto and trigger.

⁸³⁷ **2.2.3 The Interactive Neutrino GRID**

⁸³⁸ The Interactive Neutrino GRID (INGRID) detector is situated within the same “pit” as
⁸³⁹ the other near detectors. It is aligned with the beam in the “on-axis” position and mea-
⁸⁴⁰ sures the beam direction, spread, and intensity. The detector was originally designed
⁸⁴¹ with 16 identical modules [106] (two modules have since been decommissioned) and a
⁸⁴² “proton” module. The design of the detector is cross-shaped with length and height
⁸⁴³ 10m × 10m as illustrated in Figure 2.14.

⁸⁴⁴ Each module is composed of iron sheets interlaced with eleven tracking scintillator
⁸⁴⁵ planes for a total target mass of 7.1 tonnes per module. The scintillator design is an X-Y
⁸⁴⁶ pattern of 24 bars in both orientations, where each bar contains wave-length shifting
⁸⁴⁷ fibers which are connected to multi-pixel photon counters (MPPCs). The MPPCs
⁸⁴⁸ convert detected photons into electrical signals via photodiodes. This is then read
⁸⁴⁹ out by Trip-T front-end electronics [118] and passed to the readout merging modules

850 along with timing information from the clock module. Each module is encapsulated
 851 inside veto planes to aid the rejection of charged particles entering the module.

852 The proton module is different from the other modules in that it consists of entirely
 853 scintillator planes with no iron target. The scintillator bars are also smaller than those
 854 used in the other modules to increase the granularity of the detector and improve
 855 tracking capabilities. The module sits in the center of the beamline and is designed to
 856 give precise measurements of quasi-elastic charged current interactions to evaluate
 857 the performance of the Monte Carlo simulation of the beamline.

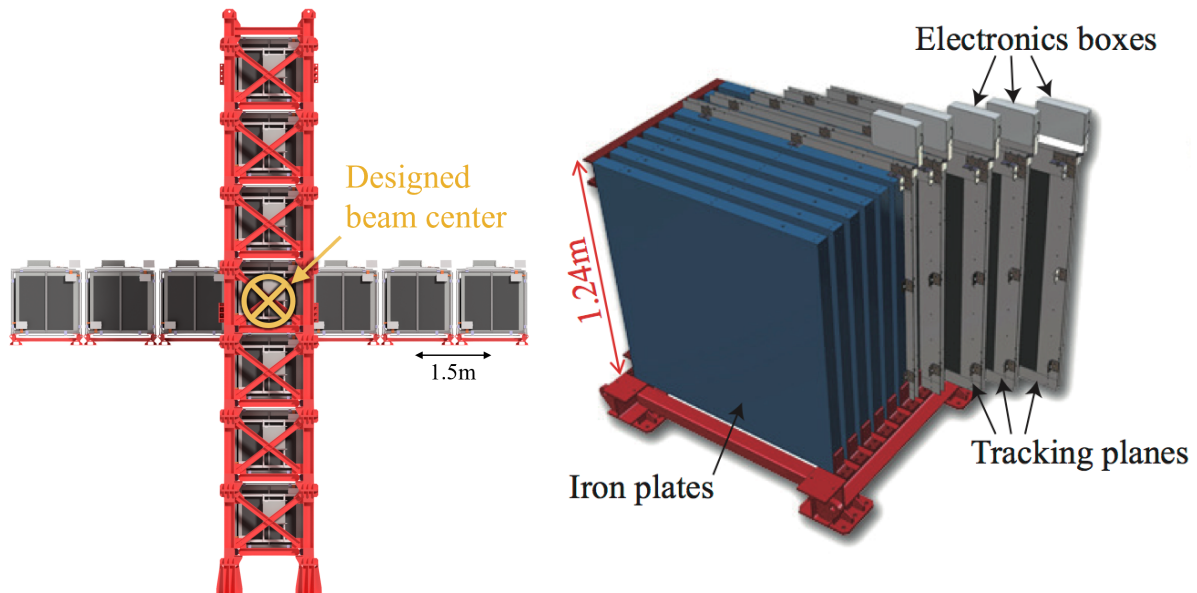


Figure 2.14: Left panel: The Interactive Neutrino GRID on-axis Detector. 14 modules are arranged in a cross-shape configuration, with the center modules being directly aligned with the on-axis beam. Right panel: The layout of a single module of the INGRID detector. Both figures are recreated from [106].

858 The INGRID detector can measure the beam direction to an uncertainty of 0.4mrad
 859 and the beam center within a resolution of 10cm [106]. The beam direction in both the
 860 vertical and horizontal directions is discussed in [119] and it is found to be in good
 861 agreement with the MUMON monitor described in subsection 2.2.1.

862 **Chapter 3**

863 **Bayesian Statistics and Markov Chain
Monte Carlo Techniques**

865 The analysis throughout this thesis is based upon a Bayesian oscillation analysis. To
866 extract the oscillation parameters, a Markov Chain Monte Carlo (MCMC) method is
867 used. This chapter explains the theory of how parameter estimates can be determined
868 using this technique and condenses the material found in the literature [120–123].

869 The oscillation parameter determination presented within this thesis is built upon a
870 simultaneous fit to the near detector, far detector beam, and atmospheric neutrino data.
871 In total, there are four oscillation parameters of interest ($\sin^2(\theta_{23})$, $\sin^2(\theta_{13})$, Δm_{23}^2 ,
872 and δ_{CP}), two oscillation parameters to which this study will not be sensitive ($\sin^2(\theta_{12})$
873 , Δm_{12}^2) and many nuisance parameters that control the systematic uncertainty models
874 invoked within this study. The systematic uncertainties can be grouped into categories
875 depending on how they are defined; 574 bin-normalisations due to the near detector
876 response, 45 bin-normalisations to describe the far detector response to neutrino beam
877 events, 27 parameters to describe the detector response to atmospheric neutrino events,
878 100 to model the bin-normalisation due to beam flux uncertainties, 18 which model the
879 atmospheric flux uncertainties, and 87 to describe the correlated cross-section model.
880 An alternative parameterisation, where the far detector response is correlated between
881 the beam and atmospheric samples, replaces the bin-normalisation parameters with
882 224 shift and smear systematics. Section [DB: Link to Systematics Chapter](#) describes
883 the systematic model in more depth.

884 The MCMC technique generates a multi-dimensional probability distribution across
 885 all of the model parameters used in the fit. To determine the parameter estimate of a
 886 single parameter, this multi-dimensional object is integrated over all other parameters.
 887 This process is called Marginalisation and is further described in subsection 3.3.1.
 888 Monte Carlo techniques approximate the probability distribution of each parameter
 889 within the limit of generating infinite samples. As ever, generating a large number of
 890 samples is time and resource-dependent. Therefore, an MCMC technique is utilised
 891 within this analysis to reduce the required number of steps to sufficiently sample the
 892 parameter space. This technique is described in further detail in subsection 3.2.1.

893 **3.1 Bayesian Statistics**

894 According to Bayesian Inference, observables and parameters of a statistical model are
 895 treated on an equal footing. To estimate model parameters $\vec{\theta}$ from some data D , one
 896 needs to define the joint probability distribution $P(D|\vec{\theta})$ which can be described as the
 897 prior distribution for model parameters $P(\vec{\theta})$ and the likelihood of the data given the
 898 model parameters $P(D|\vec{\theta})$,

$$P(D, \vec{\theta}) = P(D|\vec{\theta})P(\vec{\theta}). \quad (3.1)$$

899 The prior distribution, $P(\vec{\theta})$, describes all previous knowledge about the parameters
 900 within the model. For example, if the risk of developing health problems is known
 901 to increase with age, the prior distribution would describe the increase. For the
 902 purpose of this analysis, the prior distribution is typically the best-fit values taken
 903 from external data measurements with a Gaussian uncertainty. The prior distribution

904 can also contain correlations between model parameters. In an analysis using Monte
 905 Carlo techniques, the likelihood of measuring some data assuming some set of model
 906 parameters is calculated by comparing the Monte Carlo prediction generated at that
 907 particular set of model parameters to the data.

908 It is parameter estimation that is important for this analysis and as such, we apply
 909 Bayes' theorem [124]. To calculate the probability for each parameter to have a certain
 910 value given the observed data $P(\vec{\theta}|D)$, known as the posterior distribution (often
 911 termed the posterior). This can be expressed as

$$P(\vec{\theta}|D) = \frac{P(D|\vec{\theta})P(\vec{\theta})}{\int P(D|\vec{\theta})P(\vec{\theta})d\vec{\theta}}. \quad (3.2)$$

912 The denominator in Equation 3.2 is the integral of the joint probability distribution
 913 over all values of all parameters used within the fit. For brevity, we say that the
 914 posterior distribution is

$$P(\vec{\theta}|D)\alpha P(D|\vec{\theta})P(\vec{\theta}). \quad (3.3)$$

915 In subsection 3.3.1, we see that for the cases used within this analysis, it is reason-
 916 able to know the posterior to some normalisation constant.

917 3.2 Monte Carlo Simulation

918 Monte Carlo techniques are used to numerically solve a complex problem that does
 919 not necessarily have an analytical solution. These techniques rely on building a large

ensemble of samples from an unknown distribution and then using the ensemble to approximate the properties of the distribution.

An example that uses Monte Carlo techniques is to calculate the area underneath a curve. For example, take the problem of calculating the area under a straight line with gradient $M = 0.4$ and intercept $C = 1.0$. Analytically, one can calculate the area under the line is equal to 30 units for $0 \leq x \leq 10$. Using Monte Carlo techniques, one can calculate the area under this line by throwing many random values for the x and y components of each sample and then calculating whether that point falls below the line. The area can then be calculated by the ratio of points below the line to the total number of samples thrown multiplied by the total area in which samples were scattered. The study is shown in Figure 3.1 highlights this technique and finds the area under the curve to be 29.9 compared to an analytical solution of 30.0. The deviation of the numerical to analytical solution can be attributed to the number of samples used in the study. The accuracy of the approximation in which the properties of the Monte Carlo samples replicate those of the desired distribution is dependent on the number of samples used. Replicating this study with a differing number of Monte Carlo samples used in each study (As shown in Figure 3.2) highlights how the Monte Carlo techniques are only accurate within the limit of a high number of samples.

Whilst the above example has an analytical solution, these techniques are just as applicable to complex solutions. Clearly, any numerical solution is only as useful as its efficiency. As discussed, the accuracy of the Monte Carlo technique is dependent upon the number of samples generated to approximate the properties of the distribution. Furthermore, if the positions at which the samples are evaluated are not 'cleverly' picked, the efficiency of the Monte Carlo technique significantly drops. Given the example in Figure 3.1, if the region in which the samples are scattered significantly extends passed the region of interest, many calculations will be calculated but do

not add to the ability of the Monte Carlo technique to achieve the correct result. For instance, any sample evaluated at a $y \geq 5$ could be removed without affecting the final result. This does bring in an aspect of the ‘chicken and egg’ problem in that to achieve efficient sampling, one needs to know the distribution beforehand.

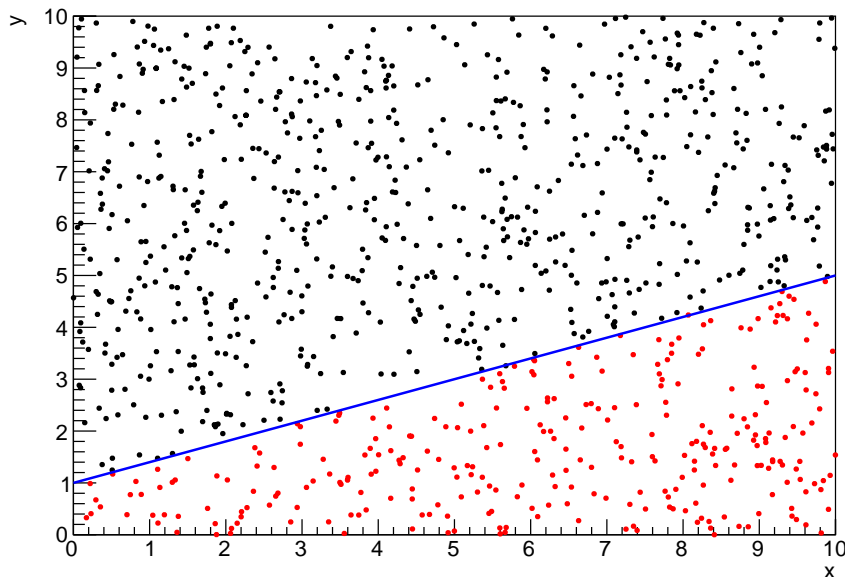


Figure 3.1: Example of using Monte Carlo techniques to find the area under the blue line. The gradient and intercept of the line are 0.4 and 1.0 respectively. The area found to be under the curve using one thousand samples is 29.9 units.

3.2.1 Markov Chain Monte Carlo

This analysis utilises a multi-dimensional probability distribution, with some dimensions being significantly more constrained than others. This could be from prior knowledge of parameter distributions from external data or un-physical regions in which parameters can not exist. Consequently, the Monte Carlo techniques used need to be as efficient as possible. For this analysis, the Markov Chain Monte Carlo (MCMC) technique is chosen. An MCMC technique is a Monte Carlo technique that uses a Markov chain to select which points at which to sample the parameter distribution.

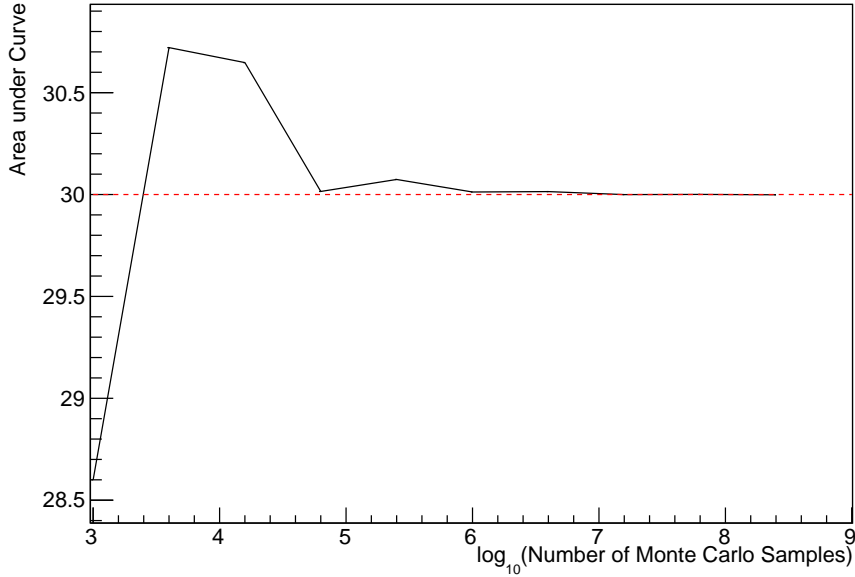


Figure 3.2: The area under a line of gradient 0.4 and intercept 1.0 for the range $0 \leq x \leq 10$ as calculated using Monte Carlo techniques as a function of the number of samples used in each repetition. The analytical solution to the area is 30 units as given by the red line.

958 This technique performs a semi-random stochastic walk through the allowable pa-
 959 rameter space. This builds a posterior distribution which has the property that the
 960 density of sampled points is proportional to the probability density of that parame-
 961 ter. This does mean that the samples produced by this technique are not statistically
 962 independent but they will cover the space of the distribution.

963 A Markov chain functions by selecting the position of step \vec{x}_{i+1} based on the
 964 position of \vec{x}_i . The space in which the Markov chain selects samples is dependent
 965 upon the total number of parameters utilised within the fit, where a discrete point in
 966 this space is described by the N-dimensional space \vec{x} . In a perfectly operating Markov
 967 chain, the position of the next step depends solely on the previous step and not on the
 968 further history of the chain (\vec{x}_0, \vec{x}_1 , etc.). However, in solving the multi-dimensionality
 969 of the fit used within this analysis, each step becomes correlated with several of
 970 the steps preceding itself. This behaviour is further explained in subsection 3.2.3.
 971 Providing the MCMC chain is well optimised, it will begin to converge towards a

unique stationary distribution. The period between the chain's initial starting point and the convergence to the unique stationary distribution is colloquially known as the burn-in period. This is discussed further in subsection 3.2.3. Once the chain reaches the stationary distribution, all points sampled after that point will look like samples from that distribution.

Further details of the theories underpinning MCMC techniques are discussed in [121] but can be summarised by the requirement that the chain satisfies the three 'regularity conditions':

- Irreducibility: From every position in the parameter space \vec{x} , there must exist a non-zero probability for every other position in the parameter space to be reached.
- Recurrence: Once the chain arrives at the stationary distribution, every step following from that position must be samples from the same stationary distribution.
- Aperiodicity: The chain must not repeat the same sequence of steps at any point throughout the sampling period.

The output of the chain after burn-in (ie. the sampled points after the chain has reached the stationary distribution) can be used to approximate the posterior distribution and model parameters $\vec{\theta}$. To achieve the requirement that the unique stationary distribution found by the chain be the posterior distribution, one can use the Metropolis-Hastings algorithm. This guides the stochastic process depending on the likelihood of the current proposed step compared to that of the previous step. Implementation and other details of this technique are discussed in subsection 3.2.2.

⁹⁹³ 3.2.2 Metropolis-Hastings Algorithm

⁹⁹⁴ As a requirement for MCMCs, the Markov chain implemented in this technique must
⁹⁹⁵ have a unique stationary distribution that is equivalent to the posterior distribution.
⁹⁹⁶ To ensure this requirement and that the regularity conditions are met, this analysis
⁹⁹⁷ utilises the Metropolis-Hastings (MH) algorithm [125,126]. For the i^{th} step in the chain,
⁹⁹⁸ the MH algorithm determines the position in the parameter space to which the chain
⁹⁹⁹ moves to based on the current step, \vec{x}_i , and the proposed step, \vec{y}_{i+1} . The proposed step
¹⁰⁰⁰ is randomly selected from some proposal function $f(\vec{x}_{i+1}|\vec{x}_i)$, which depends solely
¹⁰⁰¹ on the current step (ie. not the further history of the chain). The next step in the chain
¹⁰⁰² \vec{x}_{i+1} can be either the current step or the proposed step determined by whether the
¹⁰⁰³ proposed step is accepted or rejected. To decide if the proposed step is selected, the
¹⁰⁰⁴ acceptance probability, $\alpha(\vec{x}_i, \vec{y}_i)$, is calculated as

$$\alpha(\vec{x}_i, \vec{y}_{i+1}) = \min\left(1, \frac{P(\vec{y}_{i+1}|D)f(\vec{x}_i|\vec{y}_{i+1})}{P(\vec{x}_i|D)f(\vec{y}_{i+1}|\vec{x}_i)}\right). \quad (3.4)$$

¹⁰⁰⁵ Where $P(\vec{y}_{i+1}|D)$ is the posterior distribution as introduced in section 3.1. To
¹⁰⁰⁶ simplify this calculation, the proposal function is required to be symmetric such that
¹⁰⁰⁷ $f(\vec{x}_i|\vec{y}_{i+1}) = f(\vec{y}_{i+1}|\vec{x}_i)$. In practice, a multi-variate Gaussian distribution is used to
¹⁰⁰⁸ throw parameter proposals from. This reduces Equation 3.4 to

$$\alpha(\vec{x}_i, \vec{y}_{i+1}) = \min\left(1, \frac{P(\vec{y}_{i+1}|D)}{P(\vec{x}_i|D)}\right). \quad (3.5)$$

1009 After calculating this quantity, a random number, β , is generated uniformly be-
1010 tween 0 and 1. If $\beta \leq \alpha(\vec{x}_i, \vec{y}_{i+1})$, the proposed step is accepted. Otherwise, the chain
1011 sets the next step equal to the current step and this procedure is repeated. This can be
1012 interpreted as if the posterior probability of the proposed step is greater than that of
1013 the current step, ($P(\vec{y}_{i+1}|D) \geq P(\vec{x}_i|D)$), the proposed step will always be accepted.
1014 If the opposite is true, ($P(\vec{y}_{i+1}|D) \leq P(\vec{x}_i|D)$), the proposed step will be accepted
1015 with probability $P(\vec{x}_i|D)/P(\vec{y}_{i+1}|D)$. This ensures that the Markov chain does not get
1016 trapped in any local minima in the potentially non-Gaussian posterior distribution.
1017 The outcome of this technique is that the density of steps taken in a discrete region is
1018 directly proportional to the probability density in that region.

1019 3.2.3 MCMC Optimisation

1020 As discussed in subsection 3.2.2, the proposal function invoked within the MH algo-
1021 rithm can take any form and the chain will still converge to the stationary distribution.
1022 As discussed in [DB: Link to Analysis Strategy Section](#), this analysis performs the
1023 Monte Carlo reweighting on an event-by-event basis. This requires significant com-
1024 putational resources to perform a parameter fit. Therefore, the number of steps taken
1025 before the unique stationary distribution is found should be minimised as only steps
1026 after convergence add information to the fit. Furthermore, the chain should entirely
1027 cover the allowable parameter space to ensure that all values have been considered.
1028 Tuning the distance that the proposal function jumps between steps on a parameter-
1029 by-parameter basis can both minimise the length of the burn-in period and ensure that
1030 the correlation between step \vec{x}_i and \vec{x}_j is sufficiently small.

1031 The effect of changing the width of the proposal function is highlighted in Figure 3.3.
1032 Three scenarios, each with the same underlying stationary distribution (A Gaussian of
1033 width 1.0 and mean 0.), are presented. The only difference between the three scenarios

is the width of the proposal function, colloquially known as the ‘step size σ ’. Each scenario starts at an initial parameter value of 10.0 which would be considered an extreme variation. For the case where $\sigma = 0.1$, it is clear to see that the chain takes a long time to reach the expected region of the parameter. This indicates that this chain would have a large burn-in period and does not converge to the stationary distribution until step ~ 500 . Furthermore, whilst the chain does move towards the expected region, each step is significantly correlated with the previous. Considering the case where $\sigma = 5.0$, the chain approaches the expected parameter region almost instantly meaning that the burn-in period is not significant. However, there are clearly large regions of steps where the chain does not move. This is likely due to the chain proposing steps in the tails of the distribution which have a low probability of being accepted. Consequently, this chain would take a significant number of steps to fully span the allowable parameter region. For the final scenario, where $\sigma = 0.5$, you can see a relatively small burn-in period of approximately 100 steps. Once the chain reaches the stationary distribution, it moves throughout the expected region of parameter values many times, sufficiently sampling the full parameter region. This example is a single parameter varying across a continuous distribution and does not fully reflect the difficulties in the many-hundred multi-variate parameter distribution used within this analysis. However, it does give a conceptual idea of the importance of selecting the proposal function and associated step size.

As discussed, step size tuning directly correlates to the average step acceptance rate. If the step size is too small, many steps will be accepted but the chain moves slowly. If the opposite is true, many steps will be rejected as the chain proposes steps in the tails of the distribution. Discussion in [127] suggests that the ‘ideal’ acceptance rate of a high dimension MCMC chain should be approximately $\sim 25\%$. An “ideal” step size [127] of

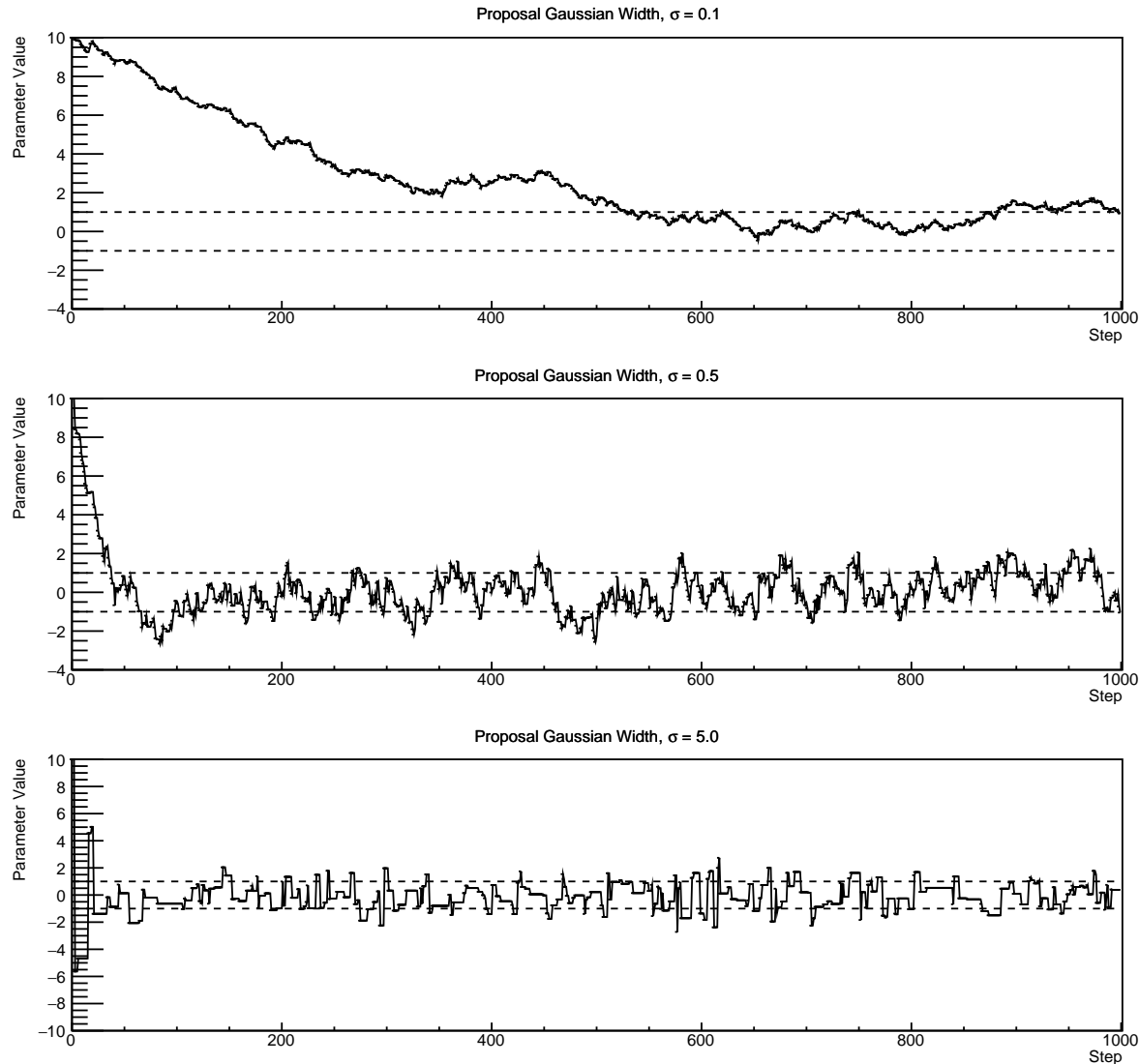


Figure 3.3: Three MCMC chains, each with a stationary distribution equal to a Gaussian centered at 0 and width 1 (As indicated by the black dotted lines). All of the chains use a Gaussian proposal function but have different widths (or ‘step size σ ’). The top panel has $\sigma = 0.1$, middle panel has $\sigma = 0.5$ and the bottom panel has $\sigma = 5.0$.

$$\sigma = \frac{2.4}{N_p}, \quad (3.6)$$

where N_p is the number of parameters included in the MCMC fit. However, the complex correlations between systematics mean that some parameters have to be hand

1062 tuned and many efforts have been taken to select a set of parameter-by-parameter step
1063 sizes to approximately reach the ideal acceptance rate.

1064 Figure 3.3 highlights the likelihood as calculated by the fit in [DB: Link to AsimovA](#)
1065 [Sensitivity Section](#) as a function of the number of steps in each chain. In practice,
1066 many independent MCMC chains are run simultaneously to parallelise the task of
1067 performing the fit. This figure overlays the distribution found in each chain. As seen,
1068 the likelihood decreases from its initial value and converges towards a stationary
1069 distribution after $\sim 1 \times 10^5$ steps. Each fit (whether it be different asimov fits or data
1070 fit) will have a different set of preferred parameter values which results in a different
1071 stationary distribution. For each fit presented in this thesis, a burn-in period of 1×10^5
1072 steps was found to be sufficient.

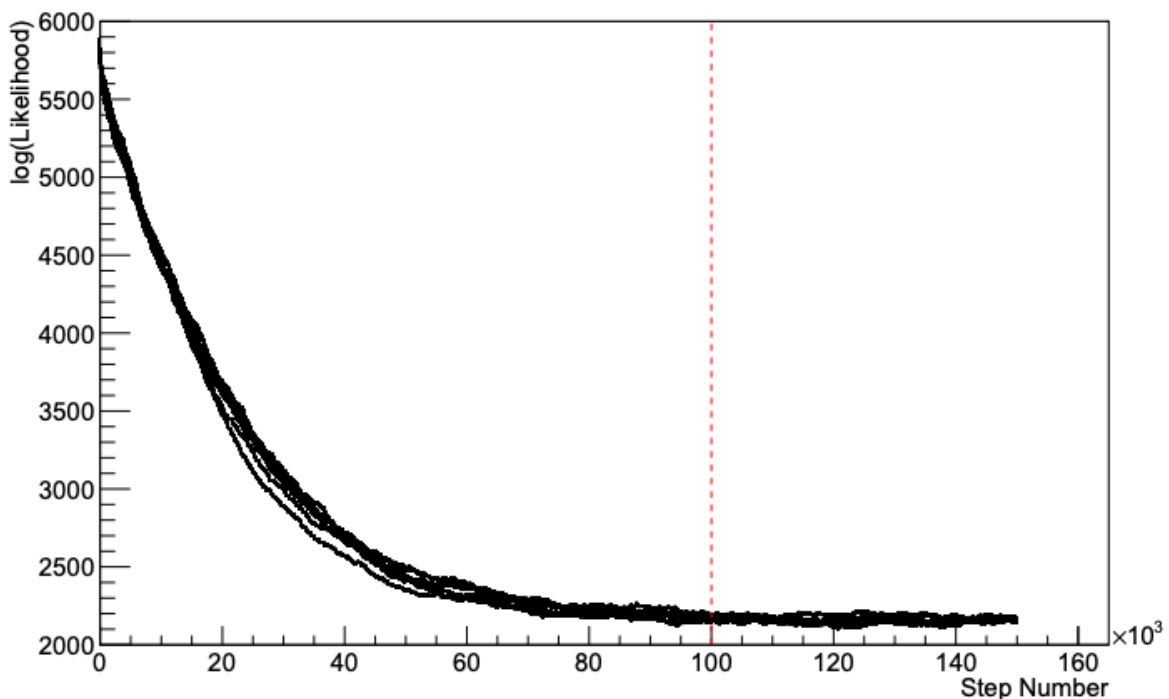


Figure 3.4: The log-likelihood from the fit detailed in [DB: Link to AsimovA](#) [Sensitivity Section](#) as a function of the number of steps accumulated in each fit. Many independent MCMC chains were run in parallel and overlaid on this plot. The red line indicates the 1×10^5 step burn-in period after which the log-likelihood becomes stable.

¹⁰⁷³ 3.3 Understanding the MCMC Results

¹⁰⁷⁴ Whilst section 3.1 and section 3.2 describe how to interpret Bayesian statistics and
¹⁰⁷⁵ explains the MCMC techniques used within this analysis, there is no mention of
¹⁰⁷⁶ how to interpret the output of the chain. The posterior distribution output from the
¹⁰⁷⁷ chain is a high dimension object, with as many dimensions as there are parameters
¹⁰⁷⁸ included in the fit. However, this multi-dimensional object is difficult to conceptualize
¹⁰⁷⁹ so parameter estimations are often presented in one or two-dimensional projections
¹⁰⁸⁰ of this probability distribution. To do this, we invoke the marginalisation technique
¹⁰⁸¹ highlighted in subsection 3.3.1.

¹⁰⁸² 3.3.1 Marginalisation

¹⁰⁸³ The output of the MCMC chain is a highly dimensional probability distribution
¹⁰⁸⁴ which is very difficult to interpret. From the standpoint of an oscillation analysis
¹⁰⁸⁵ experiment, the one or two-dimensional ‘projections’ of the oscillation parameters of
¹⁰⁸⁶ interest are most relevant. Despite this, the best fit values and uncertainties on the
¹⁰⁸⁷ oscillation parameters of interest should correctly encapsulate the correlations to the
¹⁰⁸⁸ other systematic uncertainties (colloquially called ‘nuisance’ parameters). For this joint
¹⁰⁸⁹ beam and atmospheric analysis, the oscillation parameters of interest are $\sin^2(\theta_{23})$,
¹⁰⁹⁰ $\sin^2(\theta_{13})$, Δm_{23}^2 , and δ_{CP} . All other parameters (Including the oscillation parameter
¹⁰⁹¹ this fit is insensitive to) are deemed nuisance parameters. To generate these projections,
¹⁰⁹² we rely upon integrating the posterior distribution over all nuisance parameters. This
¹⁰⁹³ is called marginalisation. A simple example of this technique is to imagine the scenario
¹⁰⁹⁴ where two coins are flipped. To determine the probability that the first coin returned
¹⁰⁹⁵ a ‘head’, the exact result of the second coin flip is disregarded and simply integrated

over. For the parameters of interest, $\vec{\theta}_i$, we can calculate the marginalised posterior by integrating over the nuisance parameters, $\vec{\theta}_n$. In this case, Equation 3.2 becomes

$$P(\vec{\theta}_i|D) = \frac{\int P(D|\vec{\theta}_i, \vec{\theta}_n)P(\vec{\theta}_i, \vec{\theta}_n)d\vec{\theta}_n}{\int P(D|\vec{\theta})P(\vec{\theta})d\vec{\theta}} \quad (3.7)$$

Where $P(\vec{\theta}_i, \vec{\theta}_n)$ encodes the prior knowledge about the uncertainty and correlations between the parameters of interest and the nuisance parameters. In practice, this is simply taking the one or two-dimensional projection of the multi-dimensional probability distribution.

Whilst in principle an easy solution to a complex problem, correlations between the interesting and nuisance parameters can bias the marginalised results. A similar effect is found when the parameters being marginalised over have non-Gaussian probability distributions. For example, Figure 3.5 highlights the marginalisation bias in the probability distribution found for a parameter when requiring a correlated parameter to have a positive parameter value. Due to the complex nature of this oscillation parameter fit presented in this thesis, there are certainly correlations occurring between the oscillation parameters of interest and the other nuisance parameters included in the fit.

3.3.2 Parameter Estimation and Credible Intervals

The purpose of this analysis is to determine the best fit values for the oscillation parameters that the beam and atmospheric samples are sensitive to; $\sin^2(\theta_{23})$, $\sin^2(\theta_{13})$, Δm_{23}^2 , and δ_{CP} . Typically, the results presented take the form of one or two-dimension marginalised probability distributions for the appearance ($\sin^2(\theta_{13})$ and δ_{CP}) and

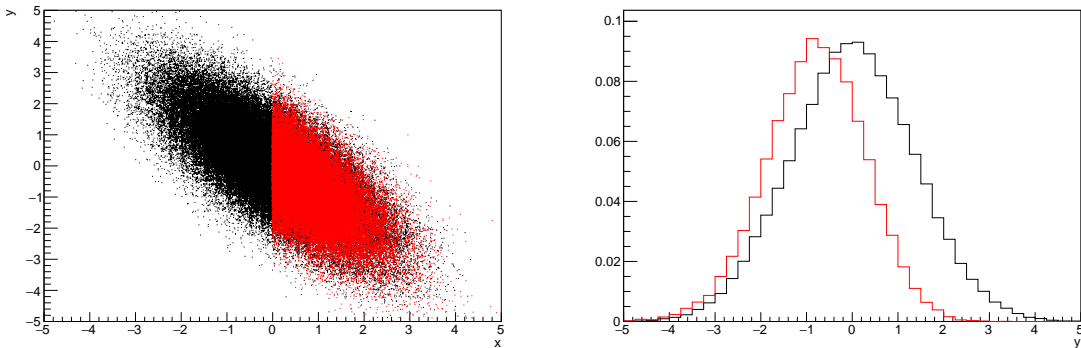


Figure 3.5: Left: The two dimensional probability distribution for two correlated parameters x and y . The red distribution shows the two dimensional probability distribution when $0 \leq x \leq 5$. Right: The marginalised probability distribution for the y parameter found when requiring the x to be bound between $-5 \leq x \leq 5$ and $0 \leq x \leq 5$ for the black and red distribution, respectively.

1116 disappearance ($\sin^2(\theta_{23})$ and Δm_{23}^2) parameters. The posterior probability density
 1117 taken from the output MCMC chain is binned in these parameters. The parameter
 1118 best-fit point is then taken to be the value that has the highest posterior probability.
 1119 This is performed in both one and two-dimensional projections.

1120 However, the single best-fit point in a given parameter is not of much use on its
 1121 own. We would also like to determine the uncertainty, or credible interval, on that
 1122 best-fit point. The definition of the 1σ credible interval is that we have 68% belief that
 1123 the parameter is within those bounds. For a more generalised definition, the credible
 1124 interval is the region of the posterior distribution that contains a specific fraction of
 1125 the total probability, such that

$$\int P(\theta|D)d\theta = \alpha \quad (3.8)$$

1126 Where θ is the parameter on which we calculate the credible interval. This technique
 1127 then calculates the $\alpha \times 100\%$ credible interval.

In practice, this analysis uses the highest posterior density (HPD) credible intervals which are calculated through the following method. First, the probability distribution is area-normalised such that it has an integrated area equal to 1.0. The bins of probability are then summed from the highest to lowest until the sum exceeds the 1σ level (0.68 in this example). This process is repeated for a range of credible intervals, notably the 1σ , 2σ and 3σ along with other levels where the critical values for each level can be found in [128]. This process can be repeated for the two-dimensional probability distributions by creating two-dimensional contours of credible intervals rather than a one-dimensional result.

3.3.3 Application of Bayes' Theorem

Due to the matter resonance, this analysis has some sensitivity to the mass hierarchy of neutrino states (whether Δm_{23}^2 is positive or negative) and the octant of $\sin^2(\theta_{23})$. The Bayesian approach utilised within this analysis gives an intuitive method of model comparison by determining which hypothesis is most favourable. Taking the ratio of Equation 3.3 for the two hypotheses of normal hierarchy, NH , and inverted hierarchy, IH , gives

$$\frac{P(\vec{\theta}_{NH}|D)}{P(\vec{\theta}_{IH}|D)} = \frac{P(D|\vec{\theta}_{NH})}{P(D|\vec{\theta}_{IH})} \times \frac{P(\vec{\theta}_{NH})}{P(\vec{\theta}_{IH})}. \quad (3.9)$$

The middle term defines the Bayes factor which is a data-driven interpretation of how strong the data prefers one hierarchy to the other. For this analysis, equal priors on both mass hierarchy hypotheses are chosen ($P(\vec{\theta}_{NH}) = P(\vec{\theta}_{IH}) = 0.5$). In practice, the MCMC chain proposes a value of $|\Delta m_{23}^2|$ and then applies a 50% probability that the value is sign flipped. Consequently, the Bayes factor can be calculated from

1149 the ratio of the probability density in either hypothesis. This equates to counting the
1150 number of steps taken in the normal and inverted hierarchies and taking the ratio. The
1151 same approach can be taken to compare the upper octant (UO) compared to the lower
1152 octant (LO) hypothesis of $\sin^2(\theta_{23})$.

1153 Whilst the value of the Bayes factor should always be shown, the Jeffreys scale [129]
1154 (highlighted in Table 3.1) gives an indication of the strength of preference for one model
1155 compared to the other. Other interpretations of the strength of preference of a model
1156 exist, e.g. the Kass and Raferty Scale [130].

$\log_{10}(B_{AB})$	B_{AB}	Strength of Preference
< 0.0	< 1	No preference for hypothesis A (Supports hypothesis B)
0.0 – 0.5	1.0 – 3.16	Preference for hypothesis A is weak
0.5 – 1.0	3.16 – 10.0	Preference for hypothesis A is substantial
1.0 – 1.5	10.0 – 31.6	Preference for hypothesis A is strong
1.5 – 2.0	31.6 – 100.0	Preference for hypothesis A is very strong
> 2.0	> 100.0	Decisive preference for hypothesis A

Table 3.1: Jeffreys scale for strength of preference for two models A and B as a function of the calculated Bayes factor ($B_{AB} = B(A/B)$) between the two models [129]. The original scale is given in terms of $\log_{10}(B(A/B))$ but converted to linear scale for easy comparison throughout this thesis.

1157 3.3.4 Comparison of MCMC Output to Expectation

1158 Whilst not important for the extraction of oscillation parameters, understanding how
1159 the data constrains the model parameters is important to the understanding of this
1160 analysis. A simple method of doing this is to perform a comparison in the fitting
1161 parameters (For instance, the reconstructed neutrino energy and lepton direction for
1162 T2K far detector beam samples) of the spectra generated by the MCMC chain to ‘data’.
1163 This ‘data’ could be true data or some variation of Monte Carlo prediction. This allows
1164 easy comparison of the MCMC probability distribution to the data. To perform this, N

1165 steps from the post burn-in MCMC chain are randomly selected (Where for all plots
1166 of this style in this thesis, $N = 3000$). From these, the Monte Carlo prediction at each
1167 step is generated by reweighting the model parameters to the values specified at that
1168 step. Due to the probability density being directly correlated with the density of steps
1169 in a certain region, parameter values close to the best fit value are most likely to be
1170 selected.

1171 In practice, for each bin of the fitting parameters has a probability distribution
1172 of event rates, with one entry per sampled MCMC step. This distribution is binned
1173 where the bin with the highest probability is selected as the mean and an error on
1174 the width of this probability distribution is calculated using the approach highlighted
1175 in subsection 3.3.2. Consequently, the best fit distribution in the fit parameter is not
1176 necessarily that which would be attained by reweighting the Monte Carlo prediction
1177 to the most probable parameter values.

1178 A similar study can be performed to illustrate the freedom of the model parameter
1179 space prior to the fit. This can be done by throwing parameter values from the prior
1180 uncertainty of each parameter. This becomes troublesome for parameters with no
1181 prior uncertainty as the range is technically infinite. Where applicable solutions to
1182 remove these have been addressed.

₁₁₈₃ **Chapter 4**

₁₁₈₄ **Oscillation Probability Calculation**

₁₁₈₅ The calculation of the oscillation probability is crucial to the reliability of the sensitivity
₁₁₈₆ measurements of the analysis presented within this thesis. Firstly, it is important to
₁₁₈₇ understand how and where the sensitivity to the oscillation parameters come from
₁₁₈₈ for both atmospheric and beam samples. An overview of how these sets of samples
₁₁₈₉ observe changes in δ_{CP} , Δm_{23}^2 and $\sin^2(\theta_{23})$ as well as how the atmospheric samples
₁₁₉₀ have an increased sensitivity to mass hierarchy determination is given in section 4.1.
₁₁₉₁ It also explains the additional complexities involved when including atmospheric
₁₁₉₂ neutrinos as compared to a beam-only analysis.

₁₁₉₃ Without additional techniques, atmospheric sub-GeV upward-going neutrinos can
₁₁₉₄ artificially inflate the sensitivity to δ_{CP} due to the quickly varying oscillation probabil-
₁₁₉₅ ity in this region. Therefore, a “sub-sampling” approach has been developed to reduce
₁₁₉₆ these biases ensuring accurate and reliable sensitivity measurements. This technique
₁₁₉₇ ensures that small-scale unresolvable features of the oscillation probability have been
₁₁₉₈ averaged over whilst the large-scale resolvable features in the oscillation probability
₁₁₉₉ have been kept. The documentation of this technique is found in section 4.2 alongside
₁₂₀₀ the validation of the choices which have been made. The CUDAProb3 implementation
₁₂₀₁ choice made within the fitting framework, as detailed in section 4.3, ensures that the
₁₂₀₂ analysis can be done in a timely manner.

₁₂₀₃ Whilst the beam neutrinos are assumed to propagate through a constant density
₁₂₀₄ slab of material, the density variations through the Earth result in more complex
₁₂₀₅ oscillation patterns Furthermore, the uncertainty in the electron density can modify

the oscillation probability for the denser core-layers of the Earth. section 4.4 details the model of the Earth used within this analysis. This includes the official SK-only methodology as well as a relatively straight forward improvement which can be made to more closely approximate the PREM model. Another quirk of atmospheric neutrinos oscillation studies is that the height of production in the atmosphere is not known on an event-by-event analysis. An analytical averaging technique that approximates the uncertainty on the oscillation probability has been followed, with the author of this thesis being responsible for the implementation and validation. This technique is illustrated in section 4.5 alongside the variation in oscillation probability which would be expected effect in the down-going and horizontal-going neutrinos.

4.1 Overview

The analysis presented within this thesis focuses on the determination of oscillation parameters from atmospheric and beam neutrinos. Whilst subject to the same oscillation probability, the way in which the two sets of samples have sensitivity to the different oscillation parameters differs quite significantly.

Atmospheric neutrinos have a varying baseline, or “path length”, such that the distance each neutrino travels before interacting is dependent upon the zenith angle. Therefore the oscillation probability can be represented as a two-dimensional “oscillogram” as shown in Figure 4.1. For this calculation, four layers of fixed density were used to model the Earth with values taken from an approximation of the PREM model. These can be seen in the distinct discontinuities in the oscillogram as a function of the zenith angle.

Another complexity of atmospheric neutrino oscillation probability calculation is the uncertainty in the height at which a neutrino was produced, termed the “produ-

tion height". Primary cosmic rays, whch contribute most of the neutrino flux, can interact anywhere between the Earth's surface and $\sim 50\text{km}$ above that. The baseline, L , for a neutrino generated with zenith angle, θ , and production height, h , can be calculated as

$$L = \sqrt{(R_E + h)^2 - R_E^2 (1 - \cos^2(\theta))} - R_E \cos(\theta), \quad (4.1)$$

where $R_E = 6,371\text{km}$ is the Earth's radius.

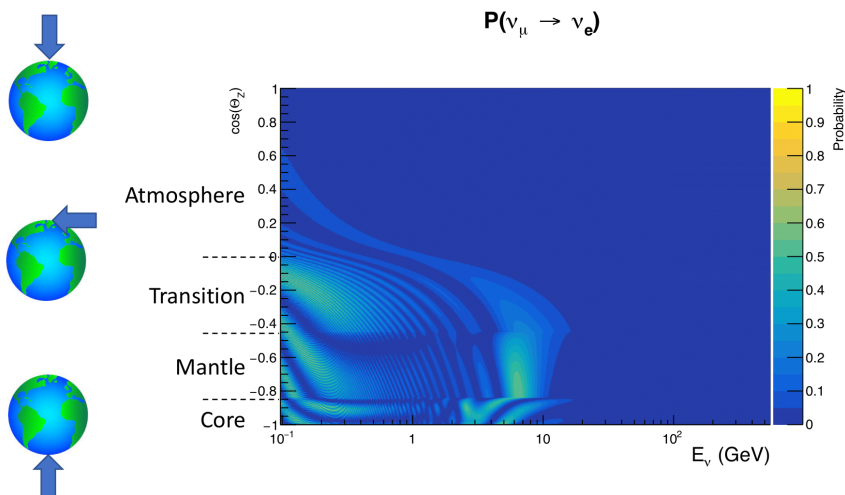


Figure 4.1: An "Oscillogram" that depicts the $P(\nu_\mu \rightarrow \nu_e)$ oscillation probability as a function of neutrino energy and cosine of the zenith angle. The zenith angle is defined such that $\cos(\theta_Z) = 1.0$ represents neutrinos that travel from directly above the detector. The four-layer constant density PREM model approximation is used and Asimov A oscillation parameters are assumed.

Atmospheric neutrinos do have some sensitivity to δ_{CP} through a normalisation term. Figure 4.2 illustrates the difference in oscillation probability between CP-conserving and CP-violating δ_{CP} values. The result is a complicated oscillation pattern in the appearance probability for sub-GeV upgoing neutrinos. The detector does not have sufficient resolution to resolve these individual patterns so the sensi-

tivity to δ_{CP} for atmospheric neutrinos comes via the overall normalisation of the sub-GeV upgoing events. The presence of matter means that the effect δ_{CP} has on the oscillation probability is not equal between neutrinos and antineutrinos which would be expected when propagating through a vacuum. This is further extenuated by the fact that SK can not distinguish neutrinos and antineutrinos well and that the cross-section neutrino interaction is larger than that for antineutrinos. Finally, sample selections (discussed in [DB: Link to selection chapter](#)) targeting different neutrino interaction modes (charge current quasi-elastic and single pion production) result in an imbalance in the percentage of neutrinos to anti-neutrinos in these samples due to pion capture. Negatively charged pions from antineutrino interactions are more likely to be captured by a nucleus compared to a positively charged pion emitted from a neutrino interaction. This all culminates in atmospheric neutrinos having a very complex sensitivity to δ_{CP} .

Atmospheric neutrinos are subject to matter effects as they travel through the dense matter in the Earth. The vacuum and matter oscillation probabilities for $P(\nu_e \rightarrow \nu_e)$ and $P(\bar{\nu}_e \rightarrow \bar{\nu}_e)$ are presented in Figure 4.3. The oscillation probability for both neutrinos and antineutrinos are affected in the presence of matter but the resonance (Effects around $E_\nu \sim 5\text{GeV}$) only occurs for neutrinos in normal mass hierarchy and antineutrinos for inverse mass ordering. The exact position and amplitude of the resonance depend on $\sin^2(\theta_{23})$ meaning that the atmospheric neutrinos have sensitivity to the octant of θ_{23} .

As the T2K beam flux is centered at the first oscillation maximum, the sensitivity to δ_{CP} is predominantly observed as a change in the event-rate of e-like samples in $\nu/\bar{\nu}$ modes. Figure 4.4 illustrates the $P(\nu_\mu \rightarrow \nu_e)$ oscillation probability for a range of δ_{CP} values. A circular modulation of the oscillation peak (in both magnitude and position) is observed when varying throughout the allowable values of δ_{CP} . The CP-

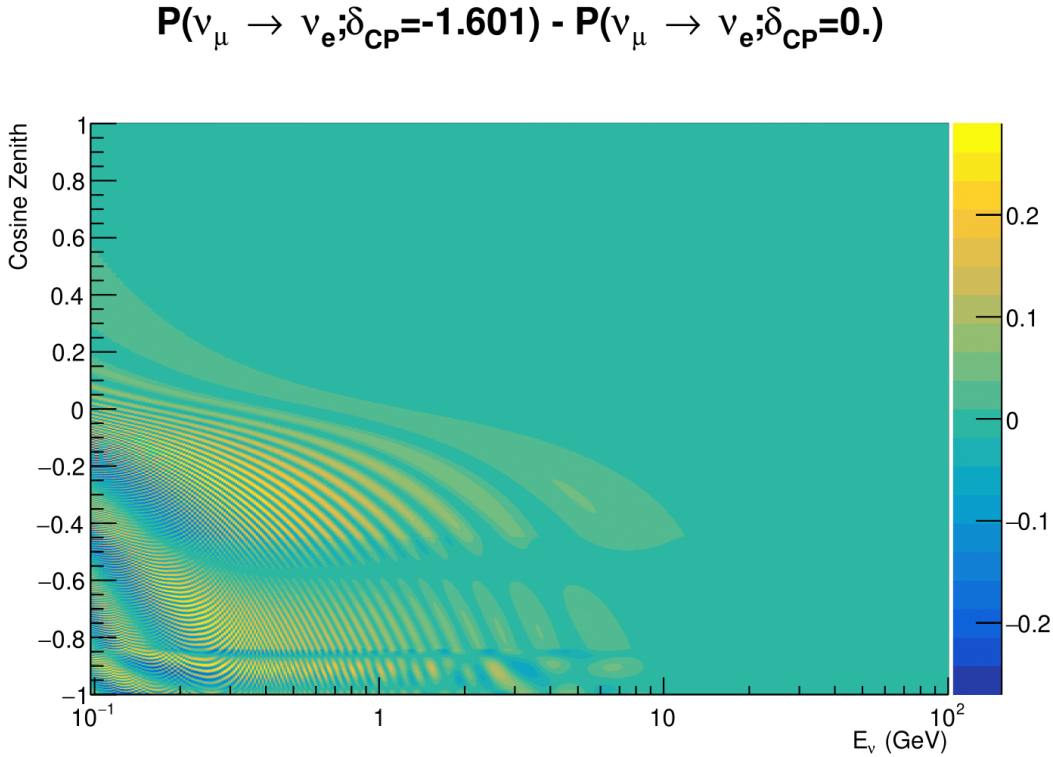


Figure 4.2: The effect of δ_{CP} for atmospheric neutrinos given in terms of the neutrino energy and zenith angle. The oscillogram compares the $P(\nu_\mu \rightarrow \nu_e)$ oscillation probability for a CP conserving ($\delta_{CP} = 0.0$) and CP violating ($\delta_{CP} = -1.601$) value of δ_{CP} . The other oscillation parameters assume the “Asimov A” oscillation parameter set given in Table 4.1.

1266 conserving values of $\delta_{CP} = 0, \pi$ have a lower(higher) oscillation maximum than the
 1267 CP-violating values of $\delta_{CP} = -\pi/2 (\delta_{CP} = \pi/2)$ leading to a $\sin(\delta_{CP})$ type sensitivity.
 1268 A sub-dominant shift in the energy of the oscillation peak is also present to aid in
 1269 separating the two CP-conserving values of δ_{CP} .

1270 T2K’s sensitivity to the atmospheric oscillation parameters is more of a shape-
 1271 based variation of the muon-like samples, as illustrated in Figure 4.4. The value of
 1272 Δm_{32}^2 laterally shifts the position of the oscillation dip (around $E_\nu \sim 0.6$ GeV) in the
 1273 $P(\nu_\mu \rightarrow \nu_\mu)$ oscillation probability. A variation of $\sin^2(\theta_{23})$ is predominantly observed
 1274 as a vertical shift of the oscillation dip with second-order horizontal shifts being due
 1275 to matter effects. The beam neutrinos have limited sensitivity to matter effects due

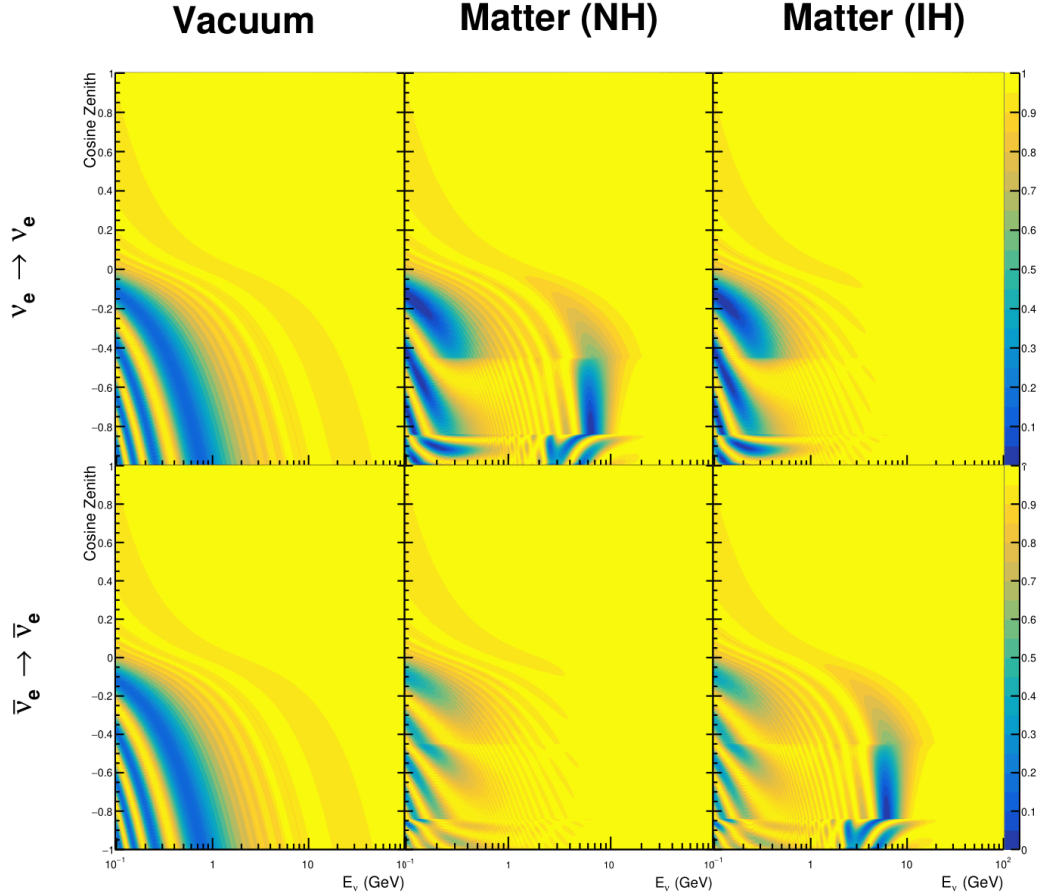


Figure 4.3: An illustration of the matter-induced effects on the oscillation probability, given as a function of neutrino energy and zenith angle. The top row of panels gives the $P(\nu_e \rightarrow \nu_e)$ oscillation probability and the bottom row illustrates the $P(\bar{\nu}_e \rightarrow \bar{\nu}_e)$ oscillation probability. The left column highlights the oscillation probability in a vacuum, whereas the middle and right column represents the oscillation probabilities when the four layer fixed density PREM model is assumed. All oscillation probabilities assume the “Asimov A” set given in Table 4.1, but importantly, the right column sets an inverted mass hierarchy. The “matter resonance” effects at $E_\nu \sim 5\text{GeV}$ can be seen in the $P(\nu_e \rightarrow \nu_e)$ for normal mass hierarchy and $P(\bar{\nu}_e \rightarrow \bar{\nu}_e)$ for inverted hierarchy.

to the shorter baseline as well as the Earth’s mantle is relatively low-density material (as compared to the Earth’s core). For some values of δ_{CP} , the degeneracy in the number of e-like events allows the mass hierarchy to be resolved. This leads to a δ_{CP} -dependent mass hierarchy sensitivity. **DB: Bi-probability plot?**

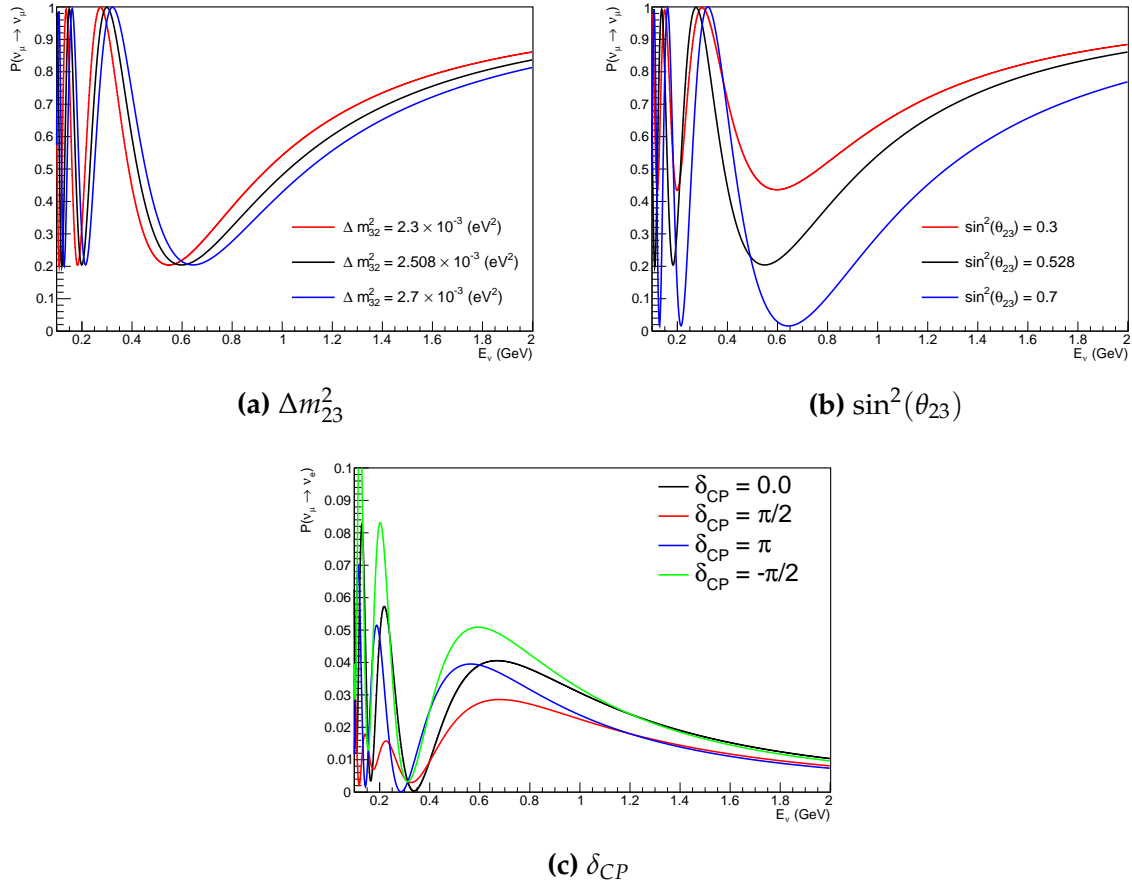


Figure 4.4: The oscillation probability for beam neutrino events, given as a function of neutrino energy. All oscillation parameters assume the “Asimov A” set given in Table 4.1 unless otherwise stated. Each panel represents a change in one of the oscillation parameters whilst keeping the remaining parameters fixed.

Whilst all oscillation channels should be included for completeness, the computational resources required to run a fit are limited and any reasonable approximations which reduce the number of oscillation probability calculations which need to be made should be applied. The $\nu_e \rightarrow \nu_{e,\mu,\tau}$ (and antineutrino equivalent) oscillations can be ignored for beam neutrinos as the $\nu_e/\bar{\nu}_e$ fluxes being approximately two orders of magnitude smaller than the corresponding $\nu_\mu/\bar{\nu}_\mu$ flux. Furthermore, as the peak neutrino energy of the beam is well below the threshold for τ production ($E_\nu \sim 3$ GeV [131]) only a small proportion of the neutrinos produced in the beam have the required energy. For the few neutrinos that have sufficient energy, the oscillation probability is very small due to the short baseline. Whilst these approximations can be made for the

1290 beam neutrinos, the atmospheric flux of ν_e is of the same order of magnitude as the ν_μ
1291 flux and the energy distribution of atmospheric neutrinos extends well above the tau
1292 production threshold.

1293 Throughout this thesis, several spectra predictions, Asimov fits, and contour com-
1294 parisons are presented which require oscillation parameters to be assumed. Table 4.1
1295 defines two sets of oscillation parameters, with “Asimov A” set being close to the
1296 preferred values from a previous T2K-only fit [DB: Need Citation](#) and “Asimov B”
1297 being CP-conserving and further from maximal θ_{23} mixing.

Parameter	Asimov A	Asimov B
Δm_{12}^2	$7.53 \times 10^{-5} \text{ eV}^2$	
Δm_{32}^2	$2.509 \times 10^{-3} \text{ eV}^2$	
$\sin^2(\theta_{12})$	0.304	
$\sin^2(\theta_{13})$	0.0219	
$\sin^2(\theta_{23})$	0.528	0.45
δ_{CP}	-1.601	0.0

Table 4.1: Reference values of the neutrino oscillation parameters for two different oscillation parameter sets.

1298 4.2 Treatment of Fast Oscillations

1299 As shown in Figure 4.5, atmospheric neutrino oscillations have a significantly more
1300 complex structure for upgoing neutrinos with energy below 1GeV. This is because the
1301 L/E dependence of the oscillation probability in this region induces rapid variations
1302 for small changes in L or E . As discussed in section 4.1, this is also the region in which
1303 atmospheric neutrinos have sensitivity to δ_{CP} . In practice, the direction between
1304 the detector and a neutrino’s production vertex is inferred from the direction of any
1305 secondary particles created in the detector target. For low energy neutrinos, this

1306 inference can be rather poor and introduces a distinct difference to beam neutrinos
1307 where the direction to production vertex is very well known.

1308 As a consequence of the poor detector resolution, an average oscillation probability
1309 is observed in this region. This creates a computational problem as a significantly
1310 large amount of MC statistics would be required to accurately predicted the number
1311 of events in each bin if MC averaging was the only technique used. This section
1312 describes the ‘sub-sampling’ approach developed for this analysis and compares it to
1313 the methodology used within the SK-only analysis.

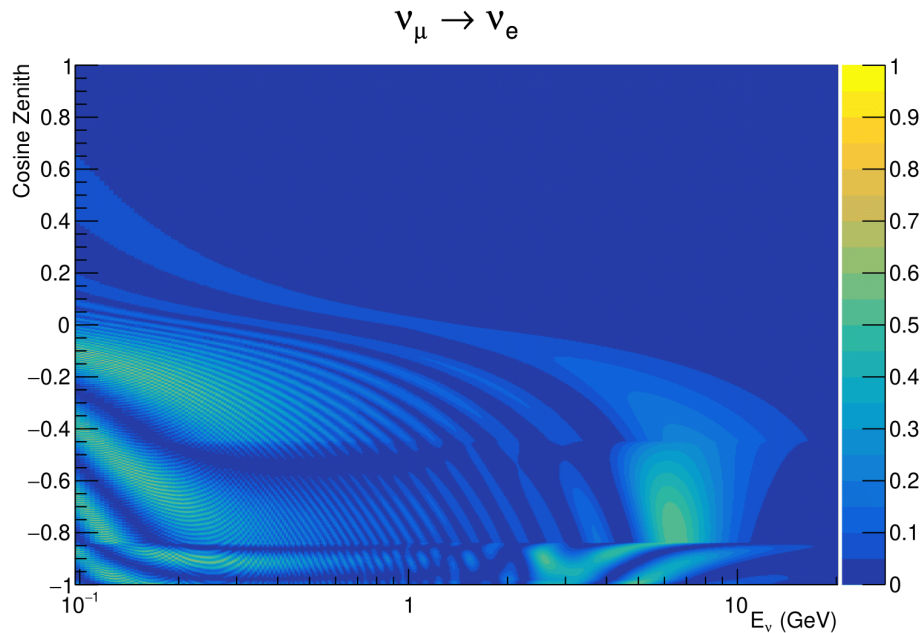


Figure 4.5: The oscillation probability $P(\nu_\mu \rightarrow \nu_e)$, given as a function of neutrino energy and zenith angle, which highlights an example of the “fast” oscillations in the sub-GeV upgoing region.

1314 The official SK-only analysis uses the osc3++ oscillation parameter fitter [132]. To
1315 perform the fast oscillation averaging, it uses a ‘nearest-neighbour’ technique. For a
1316 given neutrino MC event, the nearest neighbours in reconstructed lepton momentum
1317 and zenith angle are found and a distribution of neutrino energies is built. This

₁₃₁₈ distribution is then used to compute an average oscillation probability for the given
₁₃₁₉ neutrino MC event.

₁₃₂₀ For the i^{th} event, the oscillation weight is calculated as

$$W_i = \frac{1}{5}P(E_i, \bar{L}_i) + \frac{1}{5} \sum_{\beta=-1,-0.5,0.5,1} P(E_i + \beta\sigma_i, L_\beta), \quad (4.2)$$

₁₃₂₁ where $P(E, L)$ is the oscillation probability calculation for neutrino energy E and
₁₃₂₂ path length L , σ_i is the RMS of the energy distribution for the given event, and the
₁₃₂₃ two path lengths, \bar{L}_i and L_β are discussed below. In practice, twenty of the nearest
₁₃₂₄ neighbours are used to generate the neutrino energy distribution. All of the oscillation
₁₃₂₅ probability calculations are performed with a fixed zenith angle (and therefore have
₁₃₂₆ same matter density profile).

₁₃₂₇ The uncertainty in the production height is controlled by using an “average” pro-
₁₃₂₈ duction height. \bar{L}_i represents the average path length computed using twenty produc-
₁₃₂₉ tion heights taken from the Honda flux model’s prediction DB: Need citation for a
₁₃₃₀ fixed zenith angle, where the production heights are sampled in steps of 5% of their
₁₃₃₁ cumulative distribution function. L_β values are similarly calculated but instead use
₁₃₃₂ different combinations of four production heights (sampled in the same way),

$$\begin{aligned} L_{-1.0} &= \frac{1}{4}L(45, 50, 55, 60), \\ L_{-0.5} &= \frac{1}{4}L(35, 40, 65, 70), \\ L_{+0.5} &= \frac{1}{4}L(25, 30, 75, 68), \\ L_{+1.0} &= \frac{1}{4}L(15, 20, 85, 89). \end{aligned} \quad (4.3)$$

1333 This averaging works well because of the correlation between true neutrino zenith
1334 angle and the inferred direction from secondary particles in the detector. For low
1335 energy neutrinos, where the resolution of the true neutrino direction is poor, σ_i will be
1336 large resulting in significant averaging effects. Contrary to this, the inferred direction
1337 of high energy neutrinos will be much closer to the true value, meaning that σ_i will be
1338 smaller.

1339 In practice, this technique is performed before the fit in order to deal with the
1340 computational cost. Oscillation probabilities are pre-calculated on a 4D grid. This
1341 is possible as the Osc3++ framework uses binned oscillation parameters rather than
1342 continuous so the oscillation parameters used in the fit are known prior to run-time. The
1343 framework used in the analysis presented within this thesis uses continuous oscillation
1344 parameters. Due to the MCMC technique invoked within the fitter (see chapter 3),
1345 there is no way to know which oscillation parameter values will be selected in each
1346 step at run-time. Therefore, the oscillation parameter calculation would have to
1347 be performed at run-time which is very expensive for event-by-event reweighting.
1348 Having to compute five oscillation probabilities per event would require far too much
1349 computational resources to be viable so the SK technique can not be used within this
1350 analysis. However, the concept of the averaging technique can be taken from it.

1351 This analysis uses a binned oscillogram in which oscillation probabilities for a given
1352 event are selected based on that event's attributes. To perform a similar averaging as
1353 the SK analysis, a sub-sampling approach has been devised. The technique can be
1354 explained by considering a "fine" and "coarse" oscillogram. The fine oscillograms
1355 are used to define the array of cosine zeniths and energies for the neutrino oscillation
1356 engine. The coarse oscillograms cover the same phasespace as the fine oscillograms
1357 but have fewer bins in that range. Then, for a given coarse oscillogram bin, the value

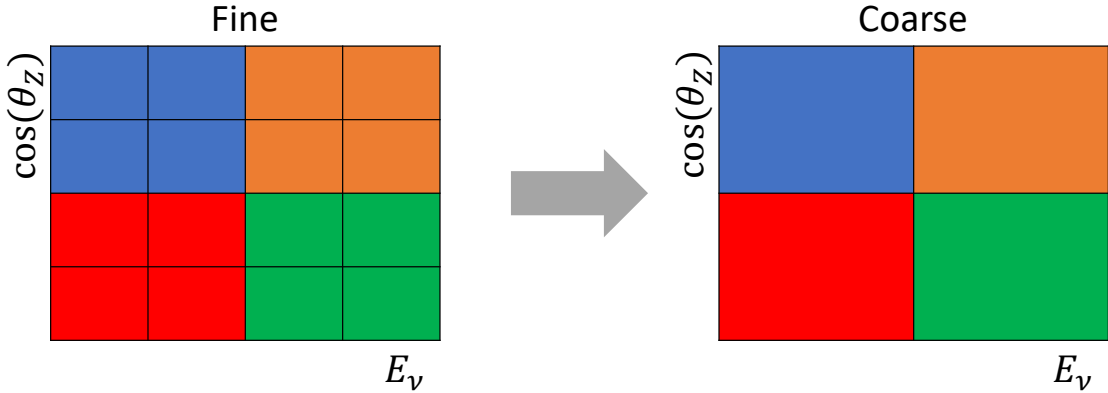


Figure 4.6: Illustration of the averaging procedure for $N = 2$. The oscillation probabilities calculated on the finer left binning are averaged to obtain the oscillation probabilities in the coarser right binning. These averaged oscillation probabilities with the coarser binning are then applied to each event during the fit.

1358 of that bin will be taken as the average of all the oscillation probabilities of all the fine
1359 oscillogram bins which fall into that coarse oscillogram bin.

1360 The binning which is used to calculate the oscillation probabilities, known as the
1361 ‘fine’ binning, has $N \times N$ subdivisions per coarse bin. The value assigned to a coarse
1362 bin is the linear average (flat prior in E_ν and $\cos(\theta_Z)$) of all the oscillation probabilities
1363 calculated at the center of each fine bin contained within that coarse bin. Figure 4.6
1364 illustrates the $N = 2$ example where the assigned value to a coarse bin is the linear
1365 average of the four fine bins which fall in that coarse bin. Whilst the coarse bin edges
1366 are not linear in either axis, the sub-division of the fine bins is linear over the range
1367 of a coarse bin. The alignment of the fine and coarse binning edges are checked at
1368 run-time.

1369 The coarse binning is defined with 67×52 bins in true neutrino energy \times cosine
1370 zenith. In general, the binning is logarithmically spaced in neutrino energy but has
1371 some hand-picked bin edges. Firstly, the bin density around the matter resonance is
1372 smoothly increased around the matter resonance region. This is to avoid smearing
1373 this region which can be well sampled by the Monte Carlo. Secondly, bin edges
1374 are selected to hit 0.4, 0.6, 1, 10, 30, 50, 100GeV. This is to ensure that the Coloumb

correction systematic and the atmospheric flux systematics definitions in neutrino energy can be hit. The cosine zenith binning is approximately linearly spaced across the allowable range but the values of layer transitions are hit precisely; -0.8376 (core-mantle) and -0.4464 (mantle/transition zone). Bins are spread further apart for downgoing events as this is a region unaffected by the fast oscillation wavelengths and reduces the total number of calculations required to perform the reweight (Not the number required to perform the oscillation calculation).

The choice of N is justified based on two studies. Firstly, the variation of event rates of each sample is studied as a function of the number of subdivisions. For a given set of oscillation parameters thrown from the PDG prior constraints, the oscillation probabilities are calculated using a given value of N . Each sample is reweighted and the event rate is stored. The value of N is scanned from 1, which corresponds to no averaging, to 24, which corresponds to the largest computationally viable subdivision binning. The event rate of each sample at large N is expected to converge to a stationary value due to the fine binning fully sampling the small scale structure. Figure 4.7 illustrates this behaviour for the SubGeV_elike_0dcy sample for 30 different throws of the oscillation parameters.

Denoting the event rate for one sample for a given throw t at each N by $\lambda_t^{(N)}$, the average over all considered N values ($\bar{\lambda}_t = \frac{1}{24} \sum_{N=1}^{24} \lambda_t^{(N)}$) is computed. The variance in the event rate at each N is then calculated from

$$\text{Var}[\lambda^{(N)}] = \frac{1}{N_{\text{throws}}} \sum_{t=1}^{N_{\text{throws}}} (\lambda_t^{(N)} - \bar{\lambda}_t)^2 - \left[\frac{1}{N_{\text{throws}}} \sum_{t=1}^{N_{\text{throws}}} (\lambda_t^{(N)} - \bar{\lambda}_t) \right]^2. \quad (4.4)$$

The aim of the study is to find the lowest value of N such that this variance is below 0.001. This is the typical threshold used by T2K fitters to validate systematic

SubGeV-elike-0dcy

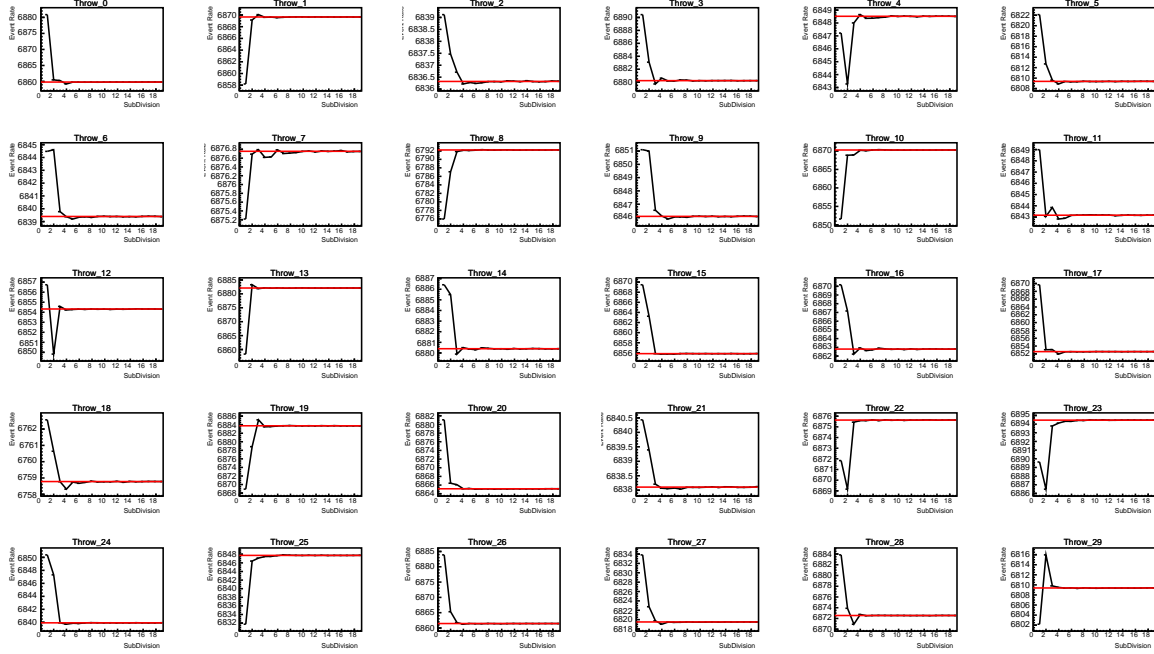


Figure 4.7: Event rate of the SubGeV_elike_0dcy sample as a function of the number of subdivisions per coarse bin. Each sub-plot represents the event rate of the sample at a different oscillation parameter set (thrown from the PDG priors). The red-line in each sub plot represents the mean of the event rate over the different values of subdivisions for that particular oscillation parameter throw.

implementation so is just as applicable to the oscillation probability calculation. The results of this study for each atmospheric sample used within this thesis are illustrated in Figure 4.8 for 2000 throws of the oscillation parameters. As can be seen, the variance is below the threshold at $N = 10$, and is driven primarily by the SubGeV_mulike_1dcy and SubGeV_elike_0dcy selections.

The second study to determine the value of N is as follows. The likelihood for each sample is computed against an Asimov data set created with oscillation parameters from “Asimov A” in Table 4.1. Following Equation 4.4, the variance of the log-likelihood over all considered N is computed. The results are shown in Figure 4.9. This tests the impact of the averaging on each sample’s binning by reconstructed

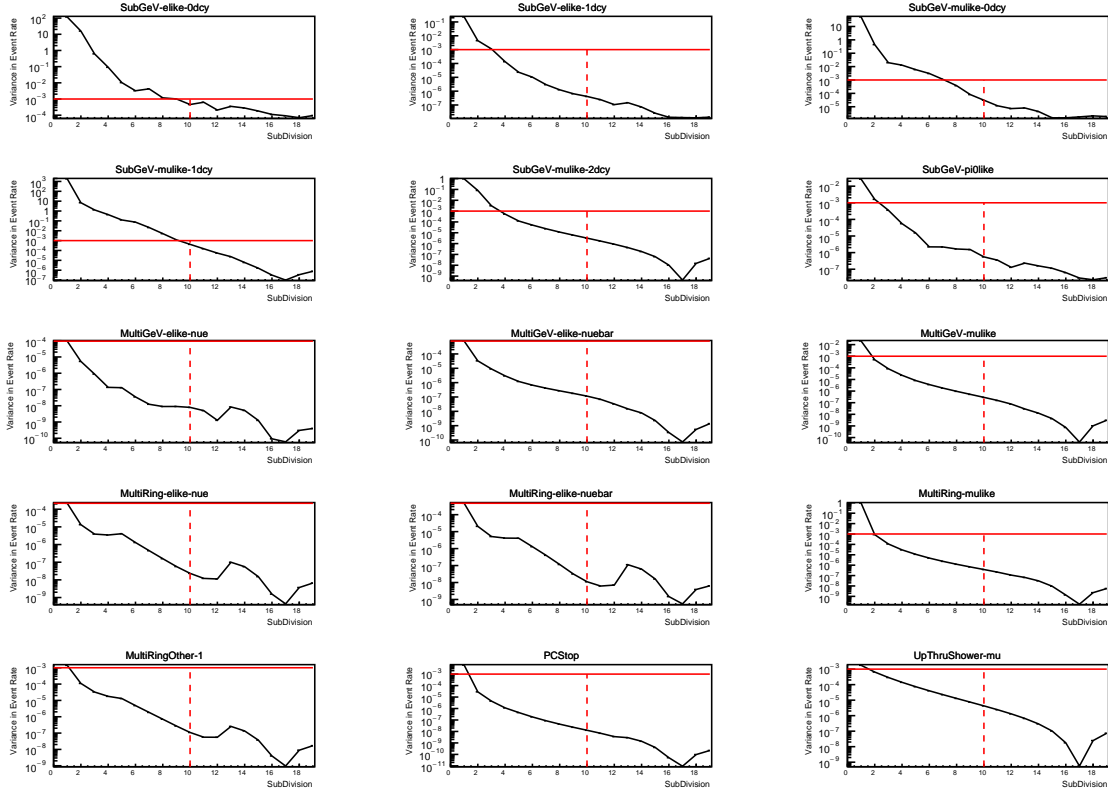


Figure 4.8: Variance of event rate for each atmospheric sample as a function of the number of sub-divisions per coarse bin. The solid red line indicates the 0.1% threshold and the dashed red line is a graphical indication of the variance at a sub-division $N = 10$.

1407 momentum and/or zenith angle and also provides a scale for the calculation errors
 1408 compared to their statistical uncertainties.

1409 A choice of N sub-divisions per coarse bin has a variance in both event rate and
 1410 log-likelihood residuals less than the required threshold of 0.001. The event rate test is
 1411 the more stringent test. For the variance of log-likelihood residuals the largest value is
 1412 of order 10^{-7} , corresponding to an error on the log-likelihood of about 3×10^{-4} , small
 1413 enough to be negligible for the oscillation analysis.

1414 In practice Figure 4.10 illustrates the effect of the smearing using $N = 10$. The fast
 1415 oscillations in the sub-GeV upgoing region have been replaced with a normalisation
 1416 effect whilst the large matter resonance structure remains.

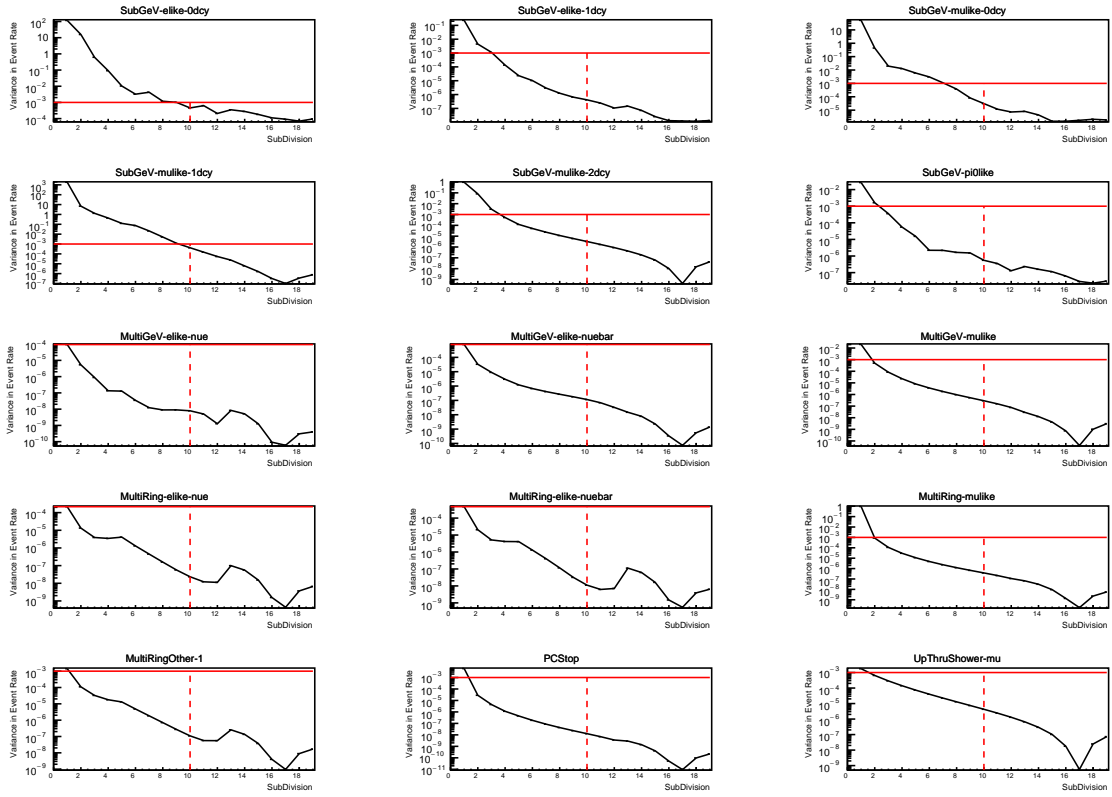


Figure 4.9: Variance of sample likelihood, when compared to ‘Asimov data’ set at Asimov A, for each atmospheric sample as a function of the number of sub-divisions per coarse bin. The solid red line indicates the 0.1% threshold and the dashed red line is a graphical indication of the variance at a sub-division $N = 10$.

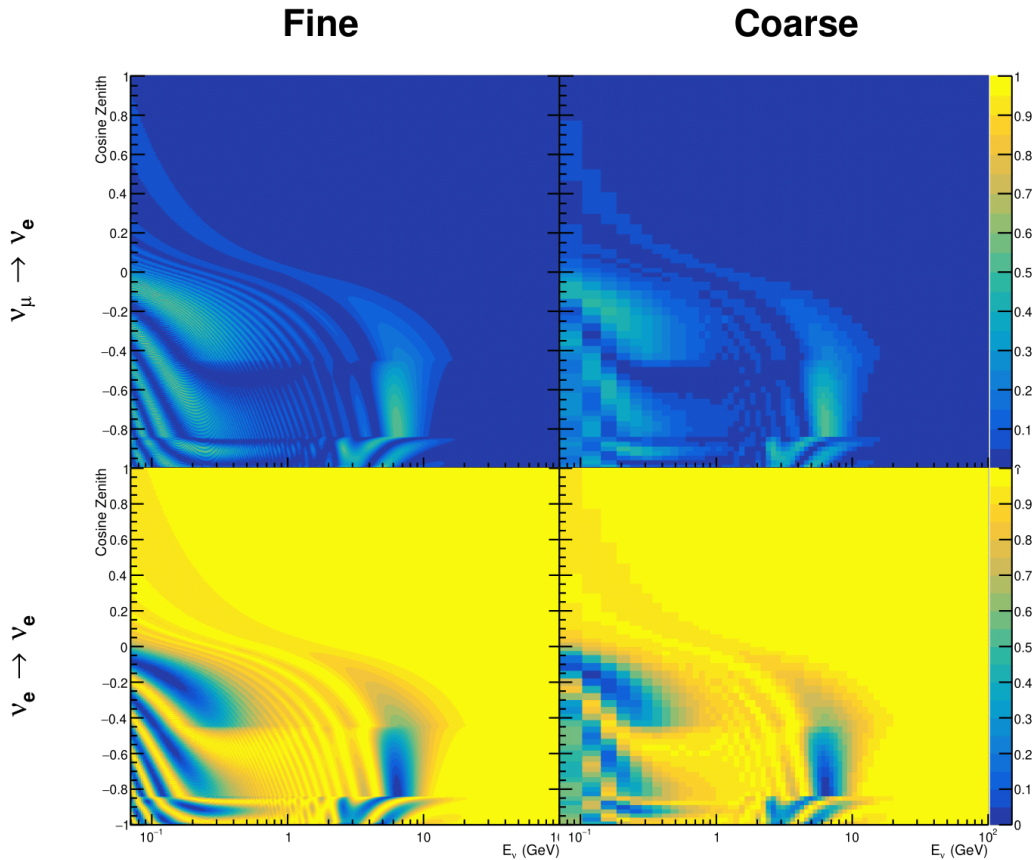


Figure 4.10: The oscillation probability, $P(\nu_\mu \rightarrow \nu_e)$ (top row) and $P(\nu_e \rightarrow \nu_e)$ (bottom row), given as a function of neutrino energy and zenith angle. The left column gives the “fine” binning used to calculate the oscillation probabilities and the right column illustrates the “coarse” binning used to reweight the MC events. The fine binning choice is given with $N = 10$, which was determined to be below threshold from Figure 4.8 and Figure 4.9.

¹⁴¹⁷ 4.3 Calculation Engine

¹⁴¹⁸ As previously discussed in section 4.2, the calculation of oscillation probabilities is per-
¹⁴¹⁹ formed at run-time due to utilising continuous oscillation parameters. Consequently,
¹⁴²⁰ the time per calculation is crucial for fit performance. The fitting framework used for
¹⁴²¹ this analysis was developed with ProbGPU [133]. This is a GPU-only implementation
¹⁴²² of the prob3 engine [134]. It is primarily designed for neutrino propagation in a beam
¹⁴²³ experiment (single layer of constant density) with the atmospheric propagation code
¹⁴²⁴ not being used prior to the analysis in this thesis.

¹⁴²⁵ Another engine, CUDAProb3 [135], has been implemented within the fitting frame-
¹⁴²⁶ work used within this analysis. It has been specifically optimised for atmospheric
¹⁴²⁷ neutrino oscillation calculation so unfortunately does not contain the code to replace
¹⁴²⁸ the beam oscillation calculation. The engine is utilises object orientated techniques as
¹⁴²⁹ compared to the functional implementation of ProbGPU. This allows the energy and
¹⁴³⁰ cosine zenith arrays to be kept on GPU memory, rather than having to load these
¹⁴³¹ arrays onto GPU memory for each calculation. General memory interfacing is one
¹⁴³² of the slowest tasks which GPUs can do, so being able to eliminate this significantly
¹⁴³³ reduces the time required for calculation. This can be seen in Figure 4.11, where
¹⁴³⁴ the GPU implementaton of CUDAProb3 is approximately three times faster than the
¹⁴³⁵ ProbGPU engine.

¹⁴³⁶ Another significant advantage of CUDAProb3 is that it contains a CPU multithreaded
¹⁴³⁷ implementation which is not possible with the ProbGPU or prob3 engines. This elimi-
¹⁴³⁸ nates the requirement for GPU resources when submitting jobs to batch systems. As
¹⁴³⁹ illustrated in Figure 4.11, the calculation speed depends on the number of available
¹⁴⁴⁰ threads. Using 8 threads (which is typical of the batch systems being used) is ap-
¹⁴⁴¹ proximately twice as slow as the ProbGPU engine implementation, but would allow

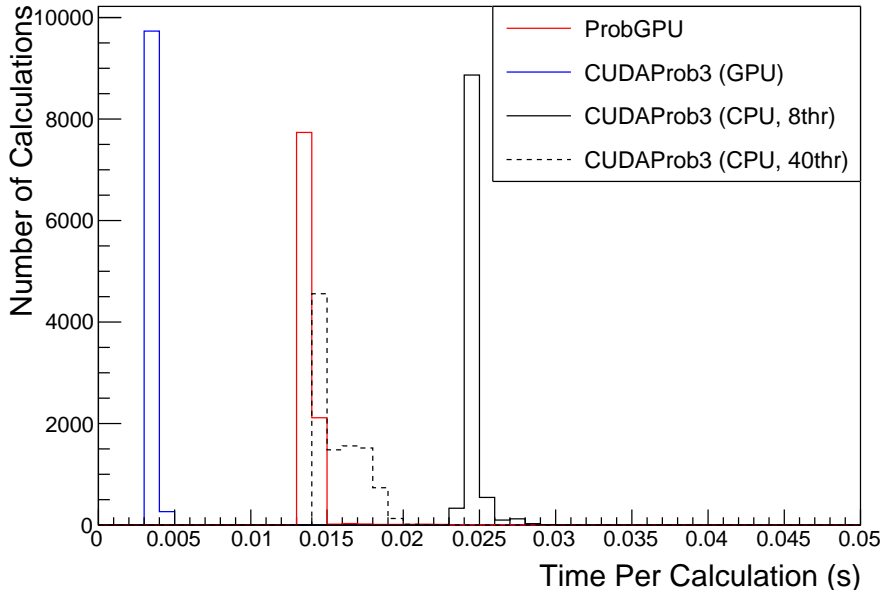


Figure 4.11: The calculation time taken to both calculate the oscillation probabilities and fill the “coarse” oscillograms, following the technique given in section 4.2, for the CUDAProb3 and ProbGPU (Red) calculation engines. CUDAProb3 has both a GPU (Blue) and CPU (Black) implementation, where the CPU implementation is multithreaded. Therefore, 8-threads (solid) and 40-threads (dashed) configurations have been used. Prob3, which is a CPU single-thread implementation has a mean step time of 1.142s.

¹⁴⁴² the fitting framework to be run on many more resources. This fact is utilised for any
¹⁴⁴³ SK-only fits but GPU resources are required for any fits which include beam samples
¹⁴⁴⁴ due to the ProbGPU requirement.

¹⁴⁴⁵ 4.4 Matter Density Profile

¹⁴⁴⁶ For an experiment observing atmospheric neutrinos propagating through the Earth,
¹⁴⁴⁷ such as the studies presented in this thesis, a model of the Earth’s density and layering
¹⁴⁴⁸ is required. The model used within this analysis is the Preliminary Reference Earth
¹⁴⁴⁹ Model (PREM) [136]. This model provides piecewise cubic polynomials as a function
¹⁴⁵⁰ of radius which results in the density profile illustrated in Figure 4.12. As will be
¹⁴⁵¹ discussed in section 4.5, the propagator used within the calculation engine requires

¹⁴⁵² constant density layers. To follow the official SK-only analysis [132], the average
¹⁴⁵³ density of each layer has been taken from the PREM model. Table 4.2 documents the
¹⁴⁵⁴ density and radii of the layers used within this approximation.

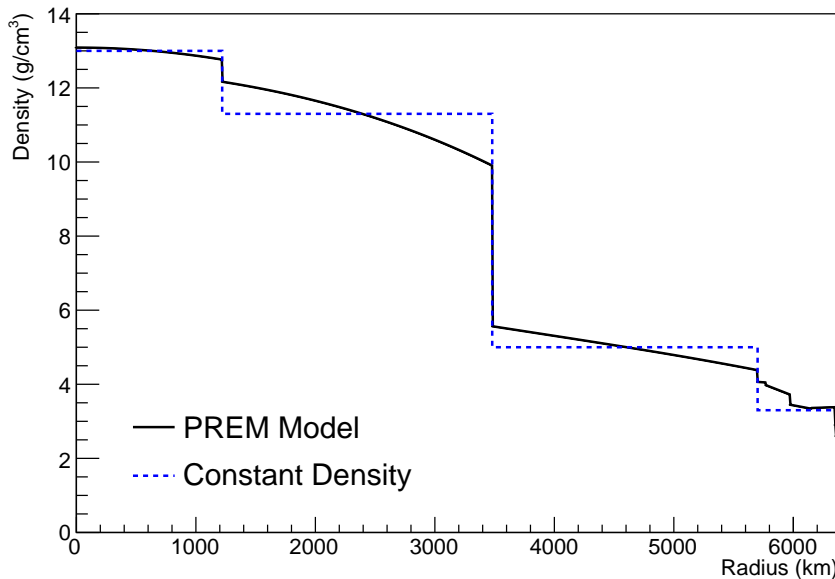


Figure 4.12: The density of the Earth given as a function of the radius, as given by the PREM model (Black) and the constant density four-layer approximation (Blue), as used in the official SK-only analysis.

Layer	Outer Radius [km]	Density [g/cm ³]	Chemical composition (Z/A)
Inner Core	1220	13	0.468 ± 0.029
Outer Core	3480	11.3	0.468 ± 0.029
Lower Mantle	5701	5.0	0.496
Transition Zone	6371	3.3	0.496

Table 4.2: Description of the four layers of the Earth invoked within the average constant density approximation of the PREM model [136].

¹⁴⁵⁵ The density measurements provided in the PREM model are provided in terms
¹⁴⁵⁶ of mass density, whereas neutrino oscillations are sensitive to the electron number
¹⁴⁵⁷ density. This value can be computed as the product of the chemical composition, or
¹⁴⁵⁸ the Z/A value, and mass density of each layer. Currently, the only way to calculate
¹⁴⁵⁹ this value for layers close to the Earth's core is through neutrino oscillations. The

¹⁴⁶⁰ chemical composition of the upper layers of the Earth's Mantle and Transition zone is
¹⁴⁶¹ well known due to it being predominantly pyrolite which has a chemical composition
¹⁴⁶² value of 0.496 [137]. The components of the Earth's core region is less well known.
¹⁴⁶³ Consequently the chemical composition dial for the core layers is set to a value of 0.468
¹⁴⁶⁴ [138]. This value is assigned a Gaussian error with standard deviation equivalent to
¹⁴⁶⁵ the difference of chemical composition in core and mantle layers. Figure 4.13 illustrates
¹⁴⁶⁶ the effect of moving from the $Z/A = 0.5$ method which is used in the official SK-only
¹⁴⁶⁷ analysis [132] to more precise values recorded by other neutrino experiments.

¹⁴⁶⁸ The beam oscillation probability in this thesis uses a baseline of 295km, density
¹⁴⁶⁹ 2.6g/cm^3 [139], and chemical composition 0.5 as is done by the official T2K-only
¹⁴⁷⁰ analysis.

¹⁴⁷¹ Whilst the propagator requires a fixed density layer model of the Earth, the density
¹⁴⁷² only has to be fixed for a specific neutrino energy $\times \cos(\theta_Z)$ bin in a given layer (I.e.
¹⁴⁷³ set of values at which to calculate the oscillation probability). As the density is a
¹⁴⁷⁴ function of radius, which is a function of the direction in which a neutrino propagates,
¹⁴⁷⁵ a better approximation of the PREM model can be made if a $\cos(\theta_Z)$ -specific density is
¹⁴⁷⁶ calculated.

¹⁴⁷⁷ To achieve this, the average density, $\langle \rho \rangle_i$, in the i^{th} layer, is calculated as the density,
¹⁴⁷⁸ ρ , integrated over the track a given $\cos(\theta_Z)$,

$$\langle \rho \rangle_i = \frac{1}{t_{i+1} - t_i} \int_{t_i}^{t_{i+1}} \rho(t) dt \quad (4.5)$$

¹⁴⁷⁹ where t_i are the intersection points between each layer and t is the path length of
¹⁴⁸⁰ the trajectory across the layer which is dependent upon $\cos(\theta_Z)$.

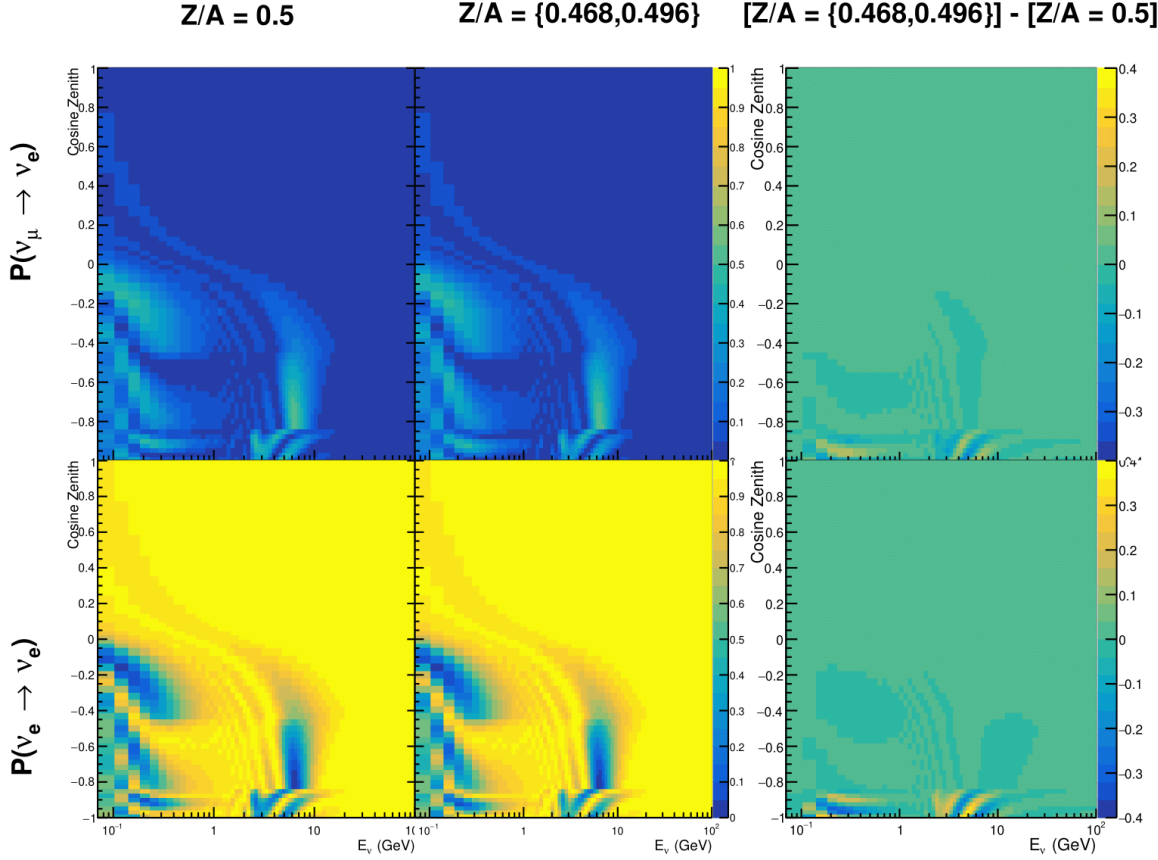


Figure 4.13: The oscillation probability, $P(\nu_\mu \rightarrow \nu_e)$ (top row) and $P(\nu_e \rightarrow \nu_\mu)$ (bottom row), given as a function of neutrino energy and zenith angle. The left column gives probabilities where the constant $Z/A = 0.5$ approximation which is used in the official SK-only analysis. The middle column gives the probabilities where the more accurate $Z/A = [0.468, 0.498]$ values as given in Table 4.2. The right column illustrates the difference in oscillation probability between the two different techniques.

The oscillation probability calculation speed is approximately linear in the number of layers invoked within the Earth model. Therefore a four layer model is still utilized with the only difference to the above example being that the four layer model used for each value of $\cos(\theta_Z)$ is different. Following the method outlined in [140], a four layer piecewise quadratic polynomial is fit to the PREM model for the four layers defined in Table 4.2. This fit was not performed by the author of the thesis and is documented in [141]. The co-efficients of the quadratic fit to each layer is given in Table 4.3 with

¹⁴⁸⁸ the final distribution illustrated in Figure 4.14. The quadratic approximation is clearly
¹⁴⁸⁹ much closer to the PREM model as compared to the constant density approximation.

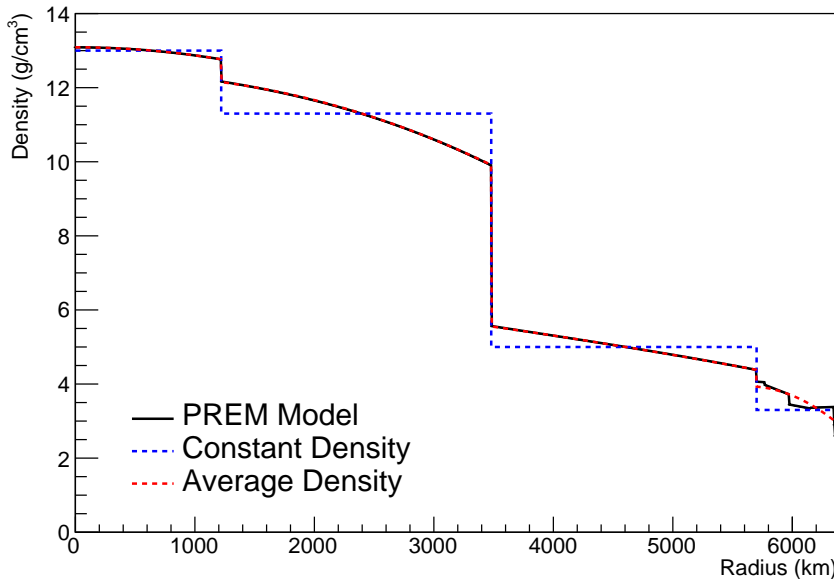


Figure 4.14: The density of the Earth given as a function of the radius, as given by the PREM model (Black), the constant density four-layer approximation (Blue), as used in the official SK-only analysis, and the quadratic approximation of the PREM model (Red).

Layer	Outer Radius [km]	Density [g/cm ³]
Inner Core	1220	$13.09 - 8.84x^2$
Outer Core	3480	$12.31 + 1.09x - 10.02x^2$
Lower Mantle	5701	$6.78 - 1.56x - 1.25x^2$
Transition Zone	6371	$-50.42 + 123.33x - 69.95x^2$

Table 4.3: The quadratic polynomial fits to the PREM model for four assumed layers of the PREM model. The fit to calculate the coefficients is given in [141], where $x = R/R_{Earth}$.

¹⁴⁹⁰ The effect of using the average density per $\cos(\theta_Z)$ model is highlighted in Fig-
¹⁴⁹¹ ure 4.15. The slight discontinuity in the oscillation probability around $\cos(\theta_Z) \sim -0.45$
¹⁴⁹² in the fixed density model, which is due to the transition to mantle layer boundary, has
¹⁴⁹³ been reduced. This is expected as the difference in the density across this boundary is
¹⁴⁹⁴ significantly smaller in the average density model as compared to the constant density

model. Whilst the difference in density across the other layer transitions is reduced, there is still a significant difference. This means the discontinuities in the oscillation probabilities remain, but are significantly reduced. However, as the average density approximation matches the PREM model well in this region, these discontinuities are due to the Earth model rather than an artifact of the oscillation calculation.

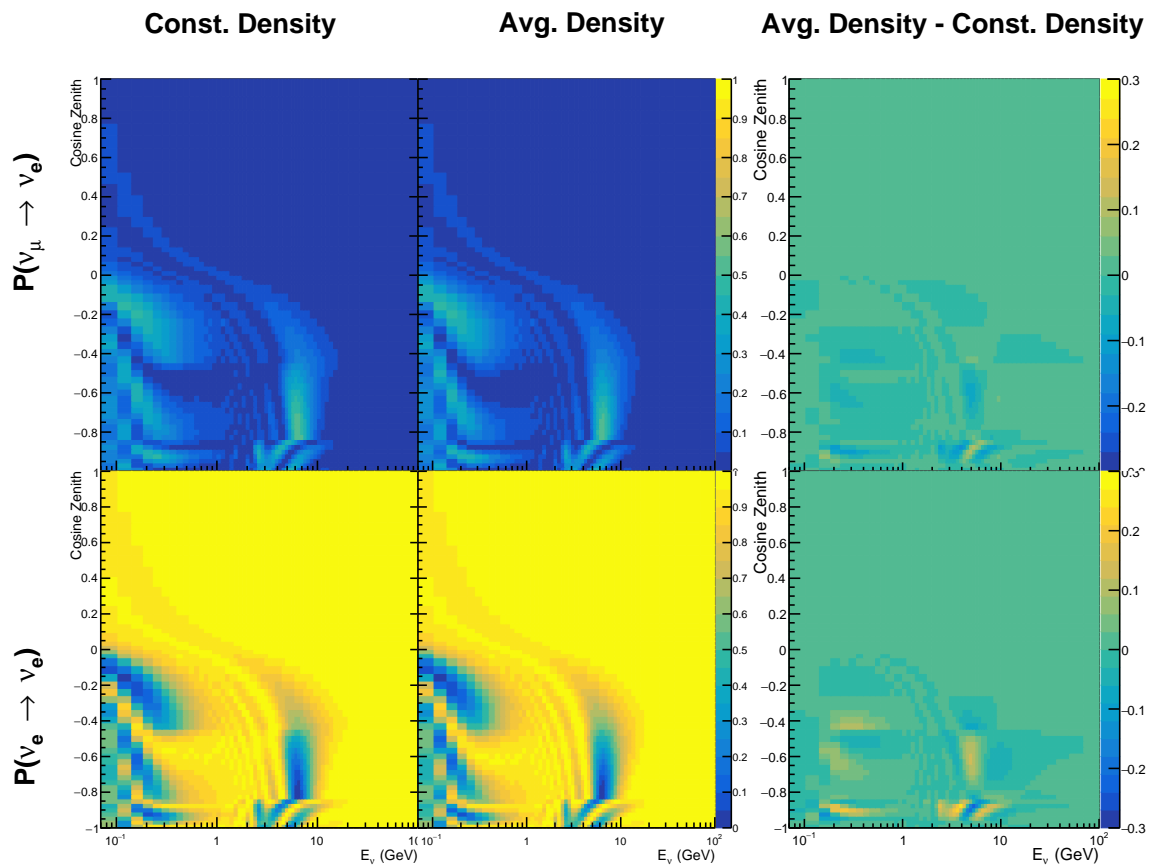


Figure 4.15: The oscillation probability, $P(\nu_\mu \rightarrow \nu_e)$ (top row) and $P(\nu_e \rightarrow \nu_e)$ (bottom row), given as a function of neutrino energy and zenith angle. The left column gives probabilities where the four-layer constant density approximation is used. The middle column gives the probabilities where the density is integrated over the trajectory, using the quadratic PREM approximation, for each $\cos(\theta_Z)$ is used. The right column illustrates the difference in oscillation probability between the two different techniques.

1500 4.5 Production Height Averaging

1501 As discussed in section 4.1, the height at which the cosmic ray flux interacts in the
1502 atmosphere is not known on an event-by-event basis. The production height can
1503 vary from the Earth's surface to 50km above that. The SK-only analysis methodol-
1504 ogy (described in section 4.2) for including the uncertainty on the production height
1505 is to include variations from the Honda model when pre-calculating the oscillation
1506 probabilities prior to the fit. This technique is not possible for this analysis which
1507 uses continuous oscillation parameters that can not be known prior to the fit. Conse-
1508 quently, an analytical averaging technique was developed in [141]. The author of this
1509 thesis was not responsible for the derivation of the technique but has performed the
1510 implementation and validation of the technique for this analysis alone.

1511 The oscillation probability used within this analysis is based on [142]. The neutrino
1512 wavefunction in the vacuum Hamiltonian evolves in each layer of constant matter
1513 density via

$$i \frac{d\psi_j(t)}{dt} = \frac{m_j^2}{2E_\nu} \psi_j(t) - \sum_k \sqrt{2} G_F N_e U_{ej} U_{ke}^\dagger \psi_k(t), \quad (4.6)$$

1514 where m_j^2 is the square of the j^{th} vacuum eigenstate mass, E_ν is the neutrino energy,
1515 G_F is Fermi's constant, N_e is the electron number density and U is the PMNS matrix.
1516 $N_e \rightarrow -N_e$ and $\delta_{CP} \rightarrow -\delta_{CP}$ for antineutrino propagation.

1517 Using the 20 production heights per MC neutrino event, provided as 5% percentiles
1518 from the Honda flux model, a production height distribution $p_j(h|E_\nu, \cos \theta_Z)$ is built
1519 for each neutrino flavour $j = \nu_e, \bar{\nu}_e, \nu_\mu, \bar{\nu}_\mu$. In practice, a histogram is filled with 20
1520 evenly spaced bins in production height h between 0 and 50km. The neutrino energy

and cosine zenith binning is the same as that provided in section 4.2. The average production height, $\bar{h} = \int dh \frac{1}{4} \sum_j p_j(h|E_\nu, \cos(\theta_Z))$, is calculated. The production height binning of this histogram is then translated into $\delta t(h) = t(z, \bar{h}) - t(z, h)$, where $t(z, h)$ is the distance travelled along the trajectory.

For the i^{th} traversed layer, the transition amplitude, $D_i(t_{i+1}, t_i)$, is computed. The time ordered product of these is then used as the overall transition amplitude via

$$A(t_{n+1}, t_0) = D_n(t_{n+1}, t_n) \dots D_1(t_2, t_1) D_0(t_1, t_0), \quad (4.7)$$

where,

$$\begin{aligned} D_n(t_{n+1}, t_n) &= \exp[-iH_n(t_{n+1} - t_n)] \\ &= \sum_{k=1}^3 C_k \exp[ia_k \delta t] \end{aligned} \quad (4.8)$$

is expressed as a diagonalised time-dependent solution to the schrodinger equation. The 0^{th} layer is the propagation through the atmosphere and is the only term which depends on the production height. Using the substitution $t_0 = t(\bar{h}) - \delta t(h)$, it can be shown that

$$D_0(t_1, t_0) = D_0(t_1, \bar{h}) D_0(\delta t). \quad (4.9)$$

Thus Equation 4.7 becomes

$$\begin{aligned}
A(t_{n+1}, t_0) &= D_n(t_{n+1}, t_n) \dots D_1(t_2, t_1) D_0(t_1, \bar{h}) D(\delta t) \\
&= A(t_{n+1}, \bar{h}) \sum_{k=1}^3 C_k \exp[i a_k \delta t], \\
&= \sum_{k=1}^3 B_k \exp[i a_k \delta t].
\end{aligned} \tag{4.10}$$

₁₅₃₃ The oscillation probability, averaged over production height is calculated as

$$\begin{aligned}
\bar{P}(\nu_j \rightarrow \nu_i) &= \int d(\delta t) p_j(\delta t | E_\nu, \cos \theta_Z) P(\nu_j \rightarrow \nu_i) \\
&= \int d(\delta t) p_j(\delta t | E_\nu, \cos \theta_Z) A(t_{n+1}, t_0) A^*(t_{n+1}, t_0) \\
&= \sum_{km} (B_k)_{ij} (B_m)_{ij}^* \int d(\delta t) p_j(\delta t | E_\nu, \cos \theta_Z) \exp[i(a_k - a_m)\delta t]
\end{aligned} \tag{4.11}$$

₁₅₃₄ In practice, implementation in CUDAProb3 [135] is relatively straight forward as
₁₅₃₅ the majority of these terms are already calculated in the standard oscillation calculation.
₁₅₃₆ Figure 4.16 illustrates the results of the production height averaging. As expected,
₁₅₃₇ the main effect is observed in the low-energy downward-going and horizontal-going
₁₅₃₈ events. Upward-going events have to travel the radius of the Earth, $R_E = 6371\text{km}$,
₁₅₃₉ where the production height uncertainty is a small fraction of the total path length.

₁₅₄₀

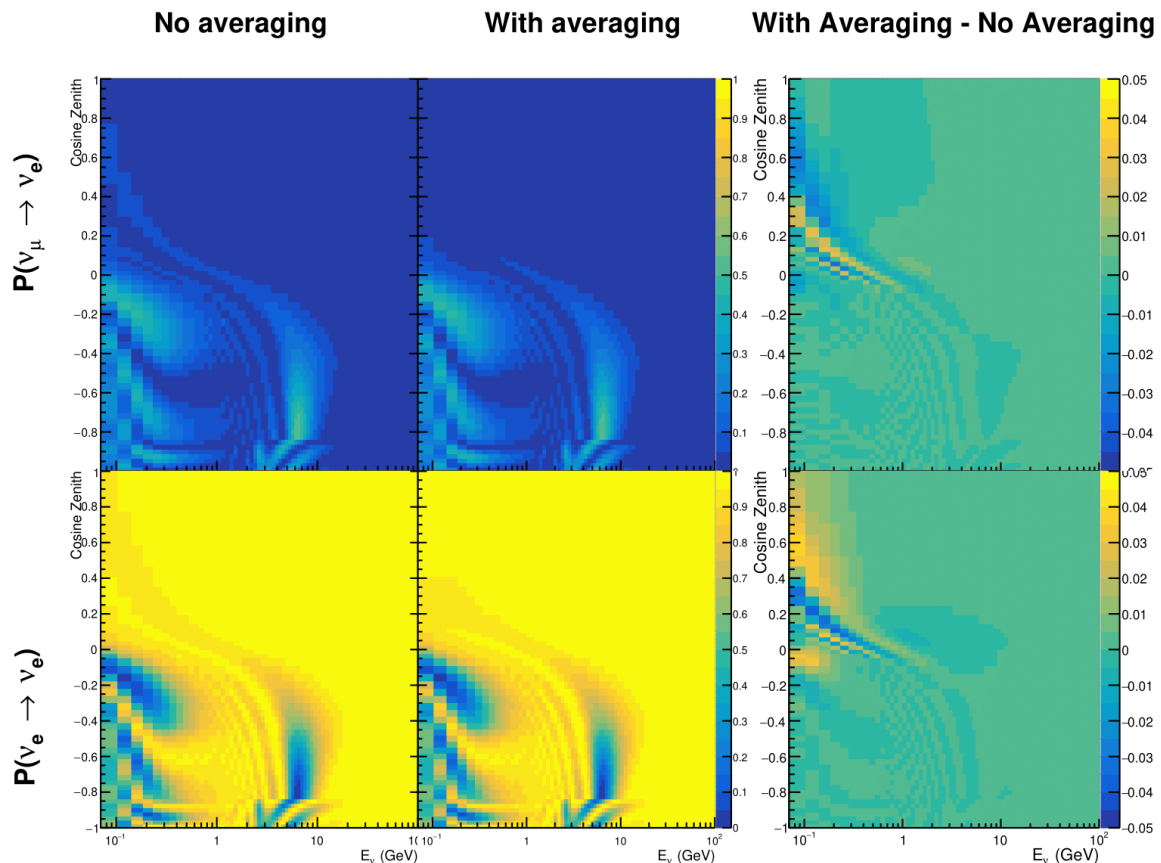


Figure 4.16: The oscillation probability, $P(\nu_\mu \rightarrow \nu_e)$ (top row) and $P(\nu_e \rightarrow \nu_\mu)$ (bottom row), given as a function of neutrino energy and zenith angle. The left column gives probabilities where a fixed production height of 25km is used. The middle column gives the probabilities where the production height is analytically averaged. The right column illustrates the difference in oscillation probability between the two different techniques.

₁₅₄₁ **Bibliography**

- ₁₅₄₂ [1] J. Chadwick, Verhandl. Dtsc. Phys. Ges. **16**, 383 (1914).
- ₁₅₄₃ [2] C. D. Ellis and W. A. Wooster, Proc. R. Soc. Lond. A Math. Phys. Sci. **117**, 109
₁₅₄₄ (1927).
- ₁₅₄₅ [3] W. Pauli, Phys. Today **31N9**, 27 (1978).
- ₁₅₄₆ [4] E. Fermi, Z. Phys. **88**, 161 (1934).
- ₁₅₄₇ [5] F. Reines and C. L. Cowan, Phys. Rev. **92**, 830 (1953).
- ₁₅₄₈ [6] C. L. Cowan, F. Reines, F. B. Harrison, H. W. Kruse, and A. D. McGuire, Science
₁₅₄₉ **124**, 103 (1956), <http://science.sciencemag.org/content/124/3212/103.full.pdf>.
- ₁₅₅₀ [7] G. Danby *et al.*, Phys. Rev. Lett. **9**, 36 (1962).
- ₁₅₅₁ [8] K. Kodama *et al.*, Physics Letters B **504**, 218 (2001).
- ₁₅₅₂ [9] LSND, A. Aguilar-Arevalo *et al.*, Phys. Rev. **D64**, 112007 (2001), hep-ex/0104049.
- ₁₅₅₃ [10] MiniBooNE Collaboration, A. A. Aguilar-Arevalo *et al.*, Phys. Rev. Lett. **110**,
₁₅₅₄ 161801 (2013).
- ₁₅₅₅ [11] and P. A. R. Ade *et al.*, Astronomy and Astrophysics **594**, A13 (2016).
- ₁₅₅₆ [12] B. Pontecorvo, Sov. Phys. JETP **26**, 984 (1968), [Zh. Eksp. Teor. Fiz. 53, 1717 (1967)].
- ₁₅₅₇ [13] B. Pontecorvo, Sov. Phys. JETP **7**, 172 (1958), [Zh. Eksp. Teor. Fiz. 34, 247 (1957)].
- ₁₅₅₈ [14] M. Kobayashi and T. Maskawa, Progress of Theoretical Physics **49**, 652 (1973).
- ₁₅₅₉ [15] N. Cabibbo, Phys. Rev. Lett. **10**, 531 (1963).
- ₁₅₆₀ [16] A. Y. Smirnov, (2003).
- ₁₅₆₁ [17] S. Mikheyev and A. Smirnov, Soviet Journal of Nuclear Physics **42**, 913 (1985).
- ₁₅₆₂ [18] L. Wolfenstein, Phys. Rev. D **17**, 2369 (1978).
- ₁₅₆₃ [19] The Super-Kamiokande Collaboration, Y. Ashie *et al.*, Phys. Rev. Lett. **93**, 101801
₁₅₆₄ (2004).
- ₁₅₆₅ [20] SNO Collaboration, Q. R. Ahmad *et al.*, Phys. Rev. Lett. **89**, 011301 (2002).

- 1566 [21] 2015 Nobel prize in Physics as listed by Nobelprize.org, [https://www.](https://www.nobelprize.org/nobel_prizes/physics/laureates/2015/)
1567 nobelprize.org/nobel_prizes/physics/laureates/2015/, Accessed: 22-06-
1568 2022.
- 1569 [22] J. A. Formaggio and G. P. Zeller, Rev. Mod. Phys. **84**, 1307 (2012), 1305.7513.
- 1570 [23] A. Bellerive, Int. J. Mod. Phys. A **19**, 1167 (2004).
- 1571 [24] R. Davis, D. S. Harmer, and K. C. Hoffman, Phys. Rev. Lett. **20**, 1205 (1968).
- 1572 [25] N. Vinyoles *et al.*, Astrophys. J. **835**, 202 (2017).
- 1573 [26] V. Gribov and B. Pontecorvo, Phys. Lett. B **28**, 493 (1969).
- 1574 [27] K. S. Hirata *et al.*, Phys. Rev. Lett. **63**, 16 (1989).
- 1575 [28] W. Hampel *et al.*, Phys. Lett. B **447**, 127 (1999).
- 1576 [29] SAGE Collaboration, J. N. Abdurashitov *et al.*, Phys. Rev. C **60**, 055801 (1999).
- 1577 [30] Q. R. Ahmad *et al.*, Phys. Rev. Lett. **89** (2002).
- 1578 [31] Borexino Collaboration, Nature **562**, 505 (2018).
- 1579 [32] B. Aharmim *et al.*, Astrophys. J. **653**, 1545 (2006).
- 1580 [33] M. Agostini *et al.*, (2020).
- 1581 [34] S. Andringa *et al.*, Adv. High Energy Phys. **2016**, 1 (2016).
- 1582 [35] J. F. Beacom *et al.*, Chin. phys. C **41**, 023002 (2017).
- 1583 [36] F. An *et al.*, J. Phys. G Nucl. Part. Phys. **43**, 030401 (2016).
- 1584 [37] J. Aalbers *et al.*, (2020), 2006.03114.
- 1585 [38] T. K. Gaisser and M. Honda, (2002).
- 1586 [39] G. D. Barr, T. K. Gaisser, P. Lipari, S. Robbins, and T. Stanev, Physical Review D
1587 **70** (2004).
- 1588 [40] M. Honda, T. Kajita, K. Kasahara, S. Midorikawa, and T. Sanuki, Physical Review
1589 D **75** (2007).
- 1590 [41] M. Honda, T. Kajita, K. Kasahara, and S. Midorikawa, Phys. Rev. D **70**, 043008
1591 (2004).

- 1592 [42] A. Fasso, A. Ferrari, P. R. Sala, and J. Ranft, (2001).
- 1593 [43] Y. Ashie *et al.*, Physical Review D **71** (2005).
- 1594 [44] F. Reines *et al.*, Phys. Rev. Lett. **15**, 429 (1965).
- 1595 [45] D. Casper *et al.*, Phys. Rev. Lett. **66**, 2561 (1991).
- 1596 [46] K. S. Hirata *et al.*, Phys. Lett. B **280**, 146 (1992).
- 1597 [47] Z. Li *et al.*, Physical Review D **98** (2018).
- 1598 [48] Kamiokande Collaboration *et al.*, (2017).
- 1599 [49] T2K Collaboration, Nature **580**, 339 (2020).
- 1600 [50] M. A. Acero *et al.*, Phys. Rev. Lett. **123**, 151803 (2019).
- 1601 [51] M. G. Aartsen *et al.*, Phys. Rev. Lett. **120** (2018).
- 1602 [52] P. Adamson *et al.*, Phys. Rev. Lett. **112** (2014).
- 1603 [53] M. S. Athar *et al.*, Progress in Particle and Nuclear Physics **124**, 103947 (2022).
- 1604 [54] G. Danby *et al.*, Phys. Rev. Lett. **9**, 36 (1962).
- 1605 [55] K. Abe *et al.*, Physical Review D **87** (2013).
- 1606 [56] MINOS Collaboration, D. G. Michael *et al.*, Phys. Rev. Lett. **97**, 191801 (2006).
- 1607 [57] G. Danby *et al.*, Phys. Rev. Lett. **9**, 36 (1962).
- 1608 [58] NOvA Collaboration, M. A. Acero *et al.*, Phys. Rev. Lett. **123**, 151803 (2019).
- 1609 [59] B. Abi, R. Acciarri, M. A. Acero, and G. e. a. Adamov, Eur. Phys. J. C Part. Fields **80** (2020).
- 1610 [60] Hyper-Kamiokande Proto-Collaboration *et al.*, Prog. Theor. Exp. Phys. **2015**, 53C02 (2015).
- 1611 [61] C. Blanco, D. Hooper, and P. Machado, Physical Review D **101** (2020).
- 1612 [62] MicroBooNE Collaboration *et al.*, Search for an Excess of Electron Neutrino Interactions in MicroBooNE Using Multiple Final State Topologies, 2021.
- 1613 [63] KARMEN Collaboration, B. Armbruster *et al.*, Phys. Rev. D **65**, 112001 (2002).
- 1614 [64] S.-B. Kim, T. Lasserre, and Y. Wang, Adv. High Energy Phys. **2013**, 1 (2013).

- [65] M. Sajjad Athar *et al.*, Prog. Part. Nucl. Phys. **124**, 103947 (2022), 2111.07586.
- [66] K. Abe *et al.*, Nucl. Instrum. Methods Phys. Res. A **1027**, 166248 (2022).
- [67] F. P. An *et al.*, Phys. Rev. Lett. **108**, 171803 (2012).
- [68] RENO Collaboration, J. K. Ahn *et al.*, Phys. Rev. Lett. **108**, 191802 (2012).
- [69] Double Chooz Collaboration, Y. Abe *et al.*, Phys. Rev. Lett. **108**, 131801 (2012).
- [70] J. Collaboration *et al.*, TAO Conceptual Design Report: A Precision Measurement of the Reactor Antineutrino Spectrum with Sub-percent Energy Resolution, 2020, 2005.08745.
- [71] for the RENO Collaboration, New results from RENO and the 5 MeV excess, AIP Publishing LLC, 2015.
- [72] Y. Abe *et al.*, Journal of High Energy Physics **2014** (2014).
- [73] Daya Bay Collaboration, D. Adey *et al.*, Phys. Rev. Lett. **123**, 111801 (2019).
- [74] M. P. Decowski, Nucl. Phys. B. **908**, 52 (2016).
- [75] The KamLAND Collaboration, A. Gando *et al.*, Phys. Rev. D **83**, 052002 (2011).
- [76] Y. Fukuda *et al.*, Phys. Rev. Lett. **81**, 1562 (1998).
- [77] K. Abe *et al.*, Nuclear Instruments and Methods in Physics Research Section A: Accelerators, Spectrometers, Detectors and Associated Equipment **737**, 253 (2014).
- [78] S. Fukuda *et al.*, Nucl. Instrum. Methods Phys. Res. A **501**, 418 (2003).
- [79] Y. Itow *et al.*, (2001).
- [80] M. Jiang *et al.*, Prog. Theor. Exp. Phys. **2019** (2019).
- [81] S. Fukuda *et al.*, Nuclear Instruments and Methods in Physics Research Section A: Accelerators, Spectrometers, Detectors and Associated Equipment **501**, 418 (2003), <http://www.sciencedirect.com/science/article/pii/S016890020300425X>.
- [82] Y. Nakano *et al.*, Nucl. Instrum. Methods Phys. Res. A **977**, 164297 (2020).
- [83] Hamamatsu, Hamamatsu Photonics Photomultiplier Tubes Handbook.
- [84] K. Abe *et al.*, Nucl. Instrum. Methods Phys. Res. A **1027**, 166248 (2022).

- [85] J. F. Beacom and M. R. Vagins, Phys. Rev. Lett. **93**, 171101 (2004).
- [86] L. Marti *et al.*, Nucl. Instrum. Methods Phys. Res. A **959**, 163549 (2020).
- [87] L. Marti *et al.*, (2019).
- [88] G. Carminati, Phys. Procedia **61**, 666 (2015).
- [89] T. Tanimori *et al.*, IEEE Transactions on Nuclear Science **36**, 497 (1989).
- [90] Super-Kamiokande Collaboration, J. Hosaka *et al.*, Phys. Rev. D **73**, 112001 (2006).
- [91] H. Nishino *et al.*, Nucl. Instrum. Methods Phys. Res. A **610**, 710 (2009).
- [92] S. Yamada *et al.*, IEEE Transactions on Nuclear Science **57**, 428 (2010).
- [93] S. Yamada, Y. Hayato, Y. Obayashi, and M. Shiozawa, New online system without hardware trigger for the Super-Kamiokande experiment, in *2007 IEEE Nuclear Science Symposium Conference Record*, IEEE, 2007.
- [94] P. A. Čerenkov, Phys. Rev. **52**, 378 (1937).
- [95] I. Frank and I. Tamm, Coherent visible radiation of fast electrons passing through matter, in *Selected Papers*, pp. 29–35, Springer Berlin Heidelberg, Berlin, Heidelberg, 1991.
- [96] The T2K Collaboration, KEK Proposal (2001), <http://neutrino.kek.jp/jhfnu/loi/loi.v2.030528.pdf>.
- [97] Y. Itow *et al.*, (2001), hep-ex/0106019.
- [98] The K2K Collaboration and S. H. Ahn, (2001), hep-ex/0103001.
- [99] The T2K Collaboration, KEK Proposal (2006), http://j-parc.jp/researcher/Hadron/en/pac_0606/pdf/p11-Nishikawa.pdf.
- [100] T2K Collaboration, K. Abe *et al.*, Phys. Rev. Lett. **112**, 061802 (2014), <https://link.aps.org/doi/10.1103/PhysRevLett.112.061802>.
- [101] NINJA Collaboration, T. Fukuda *et al.*, Proposal for precise measurement of neutrino-water cross-section in NINJA physics run, Proposal for J-PARC and KEK, 2017.
- [102] T. Ovsiannikova *et al.*, Physics of Particles and Nuclei **48**, 1014 (2017),

- 1673 <https://doi.org/10.1134/S1063779617060478>.
- 1674 [103] M. Antonova *et al.*, Journal of Instrumentation **12**, C07028 (2017),
1675 <http://stacks.iop.org/1748-0221/12/i=07/a=C07028>.
- 1676 [104] The T2K Collaboration, K. Abe *et al.*, Phys. Rev. D **102**, 012007 (2020).
- 1677 [105] K. Abe *et al.*, Progress of Theoretical and Experimental Physics **2021** (2021).
- 1678 [106] The T2K Collaboration, K. Abe *et al.*, Nuclear Instruments
1679 and Methods in Physics Research Section A: Accelerators, Spec-
1680 trometers, Detectors and Associated Equipment **659**, 106 (2011),
1681 <http://www.sciencedirect.com/science/article/pii/S0168900211011910>.
- 1682 [107] K. Matsuoka *et al.*, Nuclear Instruments and Methods in Physics Research Section
1683 A: Accelerators, Spectrometers, Detectors and Associated Equipment **624**, 591
1684 (2010), <http://www.sciencedirect.com/science/article/pii/S016890021002098X>.
- 1685 [108] K. Abe *et al.*, Phys. Rev. D. **103** (2021).
- 1686 [109] T. Vladisavljevic, *Predicting the T2K neutrino flux and measuring oscillation parame-*
1687 *ters* Springer theses, 1 ed. (Springer Nature, Cham, Switzerland, 2020).
- 1688 [110] D. Beavis, A. Carroll, and I. Chiang, (1995).
- 1689 [111] P.-A. Amaudruz *et al.*, Nuclear Instruments and Methods in Physics Research
1690 Section A: Accelerators, Spectrometers, Detectors and Associated Equipment
1691 **696**, 1 (2012).
- 1692 [112] N. Abgrall *et al.*, Nuclear Instruments and Methods in Physics Research Section
1693 A: Accelerators, Spectrometers, Detectors and Associated Equipment **637**, 25
1694 (2011).
- 1695 [113] S. Assylbekov *et al.*, Nuclear Instruments and Methods in Physics Research
1696 Section A: Accelerators, Spectrometers, Detectors and Associated Equipment
1697 **686**, 48 (2012).
- 1698 [114] D. Allan *et al.*, Journal of Instrumentation **8**, P10019 (2013).
- 1699 [115] F. Vannucci, Advances in High Energy Physics **2014**, 1 (2014).
- 1700 [116] UA1 magnet sets off for a second new life, 2022.
- 1701 [117] S. Aoki *et al.*, Nuclear Instruments and Methods in Physics Research Section

- 1702 A: Accelerators, Spectrometers, Detectors and Associated Equipment **698**, 135
1703 (2013).
- 1704 [118] M. Yokoyama *et al.*, Nuclear Instruments and Methods in Physics Research
1705 Section A: Accelerators, Spectrometers, Detectors and Associated Equipment
1706 **622**, 567 (2010).
- 1707 [119] K. Suzuki *et al.*, Progress of Theoretical and Experimental Physics **2015**, 53C01
1708 (2015).
- 1709 [120] S. Brooks, A. Gelman, G. L. Jones, and X.-L. Meng, *Handbook of Markov Chain
1710 Monte Carlo* (CRC Press, 2011).
- 1711 [121] W. R. Gilks, S. Richardson, and D. J. Spiegelhalter, *Markov Chain Monte Carlo in
1712 Practice* (Chapman & Hall/CRC Interdisciplinary Statistics, 1995).
- 1713 [122] C. Wret, *Minimising systematic uncertainties in the T2K experiment using near-
1714 detector and external data*, PhD thesis, Imperial College London, 2018.
- 1715 [123] K. E. Duffy, *Measurement of the Neutrino Oscillation Parameters $\sin^2 \theta_{23}$, Δm_{32}^2 ,
1716 $\sin^2 \theta_{13}$, and δ_{CP} in Neutrino and Antineutrino Oscillation at T2K*, PhD thesis, Oriel
1717 College, University of Oxford, 2016.
- 1718 [124] T. Bayes, Rev., Phil. Trans. Roy. Soc. Lond. **53**, 370 (1764).
- 1719 [125] N. Metropolis, A. W. Rosenbluth, M. N. Rosenbluth, A. H. Teller, and E. Teller,
1720 Journal of Chemical Physics **21** (1970).
- 1721 [126] W. K. Hastings, Biometrika **57** (1970).
- 1722 [127] J. Dunkley, M. Bucher, P. G. Ferreira, K. Moodley, and C. Skordis, Mon. Not. R.
1723 Astron. Soc. **356**, 925 (2005).
- 1724 [128] Particle Data Group *et al.*, Prog. Theor. Exp. Phys. **2020** (2020).
- 1725 [129] H. Jeffreys, *The Theory of Probability* Oxford Classic Texts in the Physical Sciences
1726 (, 1939).
- 1727 [130] R. E. Kass and A. E. Raftery, J. Am. Stat. Assoc. **90**, 773 (1995).
- 1728 [131] P. Machado, H. Schulz, and J. Turner, Physical Review D **102** (2020).
- 1729 [132] R. Wendell, *Three Flavor Oscillation Analysis of Atmospheric Neutrinos in Super-
1730 Kamiokande*, PhD thesis, University of North Carolina, 2008.

- ₁₇₃₁ [133] R. G. Calland, A. C. Kaboth, and D. Payne, **9**, P04016 (2014).
- ₁₇₃₂ [134] R. Wendell, <http://www.phy.duke.edu/raw22/public/Prob3++/>.
- ₁₇₃₃ [135] F. Kallenborn, C. Hundt, S. Böser, and B. Schmidt, Computer Physics Communications **234**, 235 (2019).
- ₁₇₃₄
- ₁₇₃₅ [136] A. M. Dziewonski and D. L. Anderson, Phys. Earth Planet. Inter. **25**, 297 (1981).
- ₁₇₃₆ [137] S. Bourret, J. A. B. Coelho, and V. V. E. and, Journal of Physics: Conference Series **888**, 012114 (2017).
- ₁₇₃₇
- ₁₇₃₈ [138] C. Rott, A. Taketa, and D. Bose, Scientific Reports **5** (2015).
- ₁₇₃₉ [139] K. Hagiwara, N. Okamura, and K. ichi Senda, Journal of High Energy Physics **2011** (2011).
- ₁₇₄₀
- ₁₇₄₁ [140] D. Typinski, Earth Gravity, <http://www.typnet.net/Essays/EarthGravGraphics/EarthGrav.pdf>, Accessed: 24-06-2022.
- ₁₇₄₂
- ₁₇₄₃ [141] D. B. et al., T2K Technical Note **425** (2022).
- ₁₇₄₄ [142] V. D. Barger, K. Whisnant, S. Pakvasa, and R. J. N. Phillips, Phys. Rev. D **22**, 2718 (1980).
- ₁₇₄₅

¹⁷⁴⁶ List of Figures

¹⁷⁴⁷ 1.1	The cross-section of neutrinos from various natural and man-made sources as a function of neutrino energy. Taken from [22]	9
¹⁷⁴⁸		
¹⁷⁴⁹ 1.2	The solar neutrino flux as a function of neutrino energy for various fusion reactions and decay chains as predicted by the Standard Solar Model. Taken from [23].	10
¹⁷⁵⁰		
¹⁷⁵¹ 1.3	Left panel: The atmospheric neutrino flux for different neutrino flavours as a function of neutrino energy as predicted by the 2007 Honda model (“This work”) [40], the 2004 Honda model (“HKKM04”) [41], the Bartol model [39] and the FLUKA model [42]. Right panel: The ratio of the muon to electron neutrino flux as predicted by all the quoted models. Both figures taken from [40].	12
¹⁷⁵²		
¹⁷⁵³		
¹⁷⁵⁴		
¹⁷⁵⁵		
¹⁷⁵⁶		
¹⁷⁵⁷		
¹⁷⁵⁸ 1.4	A diagram illustrating the definition of zenith angle as used in the Super Kamiokande experiment [43].	13
¹⁷⁵⁹		
¹⁷⁶⁰ 1.5	Predictions of the summed neutrino and antineutrino flux for electron and muon neutrinos from the Bartol [39], Honda [40] and FLUKA [42] models as a function of zenith angle with respect to the detector. Left panel: $0.3 < E_\nu < 0.5$. Middle panel: $0.9 < E_\nu < 1.5$. Right panel: $3.0 < E_\nu < 5.0$. Figures taken from [43].	14
¹⁷⁶¹		
¹⁷⁶²		
¹⁷⁶³		
¹⁷⁶⁴		
¹⁷⁶⁵ 1.6	Constraints on the atmospheric oscillation parameters, $\sin^2(\theta_{23})$ and Δm_{23}^2 , from atmospheric and long baseline experiments: SK [48], T2K [49], NO ν A [50], IceCube [51] and MINOS [52]. Figure taken from [53].	15
¹⁷⁶⁶		
¹⁷⁶⁷		
¹⁷⁶⁸ 1.7	Reactor electron antineutrino fluxes for ^{235}U (Black), ^{238}U (Green), ^{239}Pu (Purple), and ^{241}Pu (Orange) isotopes. The inverse β -decay cross-section (Blue) and corresponding measurable neutrino spectrum (Red) are also given. Top panel: Schematic of Inverse β -decay interaction including the eventual capture of the emitted neutron. This capture emits a γ -ray which provides a second signal of the event. Taken from [65].	18
¹⁷⁶⁹		
¹⁷⁷⁰		
¹⁷⁷¹		
¹⁷⁷²		
¹⁷⁷³		
¹⁷⁷⁴ 2.1	A schematic diagram of the Super-Kamiokande Detector. Taken from [79].	22

1775	2.2	The location of “standard PMTs” (red) inside the SK detector. Taken from [77].	26
1776			
1777	2.3	Schematic view of the data flow through the data acquisition and online system. Taken from [92].	29
1778			
1779	2.4	The cross-section view of the Tokai to Kamioka experiment illustrating the beam generation facility at J-PARC, the near detector situated at a baseline of 280m and the Super Kamiokande far detector situated 295km from the beam target.	32
1780			
1781			
1782			
1783	2.5	The near detector suite for the T2K experiment showing the ND280 and INGRID detectors. The distance between the detectors and the beam target is 280m.	33
1784			
1785			
1786	2.6	Top panel: Bird’s eye view of the most relevant part of primary and secondary beamline used within the T2K experiment. The primary beamline is the main-ring proton synchrotron, kicker magnet, and graphite target. The secondary beamline consists of the three focusing horns, decay volume, and beam dump. Figure taken from [106]. Bottom panel: The side-view of the secondary beamline including the focusing horns, beam dump and neutrino detectors. Figure taken from [107].	35
1787			
1788			
1789			
1790			
1791			
1792			
1793	2.7	The Monte Carlo prediction of the energy spectrum for each flavour of neutrino (ν_e , $\bar{\nu}_e$, ν_μ and $\bar{\nu}_\mu$) in the neutrino dominated beam FHC mode (Left) and antineutrino dominated beam RHC mode (Right) expected at SK. Taken from [108].	36
1794			
1795			
1796			
1797	2.8	Top panel: T2K muon neutrino disappearance probability as a function of neutrino energy. Middle panel: T2K electron neutrino appearance probability as a function of neutrino energy. Bottom panel: The neutrino flux distribution for three different off-axis angles (Arbitrary units) as a function of neutrino energy.	38
1798			
1799			
1800			
1801			
1802	2.9	The components of the ND280 detector. The neutrino beam travels from left to right. Taken from [106].	39
1803			
1804	2.10	Comparison of data to Monte Carlo prediction of integrated deposited energy as a function of track length for particles that stopped in FGD1. Taken from [111].	41
1805			
1806			

1807	2.11 Schematic design of a Time Projection Chamber detector. Taken from [112].	42
1808	2.12 The distribution of energy loss as a function of reconstructed momentum for charged particles passing through the TPC, comparing data to Monte Carlo prediction. Taken from [112].	42
1810		
1811	2.13 A schematic of the P0D side-view. Taken from [113].	44
1812	2.14 Left panel: The Interactive Neutrino GRID on-axis Detector. 14 modules are arranged in a cross-shape configuration, with the center modules being directly aligned with the on-axis beam. Right panel: The layout of a single module of the INGRID detector. Both figures are recreated from [106].	46
1814		
1816		
1817	3.1 Example of using Monte Carlo techniques to find the area under the blue line. The gradient and intercept of the line are 0.4 and 1.0 respectively. The area found to be under the curve using one thousand samples is 29.9 units.	51
1819		
1820		
1821	3.2 The area under a line of gradient 0.4 and intercept 1.0 for the range $0 \leq x \leq 10$ as calculated using Monte Carlo techniques as a function of the number of samples used in each repetition. The analytical solution to the area is 30 units as given by the red line.	52
1823		
1824		
1825	3.3 Three MCMC chains, each with a stationary distribution equal to a Gaussian centered at 0 and width 1 (As indicated by the black dotted lines). All of the chains use a Gaussian proposal function but have different widths (or ‘step size σ ’). The top panel has $\sigma = 0.1$, middle panel has $\sigma = 0.5$ and the bottom panel has $\sigma = 5.0$.	57
1827		
1829		
1830	3.4 The log-likelihood from the fit detailed in DB: Link to AsimovA Sensitivity Section as a function of the number of steps accumulated in each fit. Many independent MCMC chains were run in parallel and overlaid on this plot. The red line indicates the 1×10^5 step burn-in period after which the log-likelihood becomes stable.	58
1831		
1832		
1833		
1834		

1835 3.5	Left: The two dimensional probability distribution for two correlated parameters x and y . The red distribution shows the two dimensional probability distribution when $0 \leq x \leq 5$. Right: The marginalised probability distribution for the y parameter found when requiring the x to be bound between $-5 \leq x \leq 5$ and $0 \leq x \leq 5$ for the black and red distribution, respectively.	61
1841 4.1	An “Oscillogram” that depicts the $P(\nu_\mu \rightarrow \nu_e)$ oscillation probability as a function of neutrino energy and cosine of the zenith angle. The zenith angle is defined such that $\cos(\theta_Z) = 1.0$ represents neutrinos that travel from directly above the detector. The four-layer constant density PREM model approximation is used and Asimov A oscillation parameters are assumed.	67
1847 4.2	The effect of δ_{CP} for atmospheric neutrinos given in terms of the neutrino energy and zenith angle. The oscillogram compares the $P(\nu_\mu \rightarrow \nu_e)$ oscillation probability for a CP conserving ($\delta_{CP} = 0.0$) and CP violating ($\delta_{CP} = -1.601$) value of δ_{CP} . The other oscillation parameters assume the “Asimov A” oscillation parameter set given in Table 4.1.	69
1852 4.3	An illustration of the matter-induced effects on the oscillation probability, given as a function of neutrino energy and zenith angle. The top row of panels gives the $P(\nu_e \rightarrow \nu_e)$ oscillation probability and the bottom row illustrates the $P(\bar{\nu}_e \rightarrow \bar{\nu}_e)$ oscillation probability. The left column highlights the oscillation probability in a vacuum, whereas the middle and right column represents the oscillation probabilities when the four layer fixed density PREM model is assumed. All oscillation probabilities assume the “Asimov A” set given in Table 4.1, but importantly, the right column sets an inverted mass hierarchy. The “matter resonance” effects at $E_\nu \sim 5\text{GeV}$ can be seen in the $P(\nu_e \rightarrow \nu_e)$ for normal mass hierarchy and $P(\bar{\nu}_e \rightarrow \bar{\nu}_e)$ for inverted hierarchy.	70
1863 4.4	The oscillation probability for beam neutrino events, given as a function of neutrino energy. All oscillation parameters assume the “Asimov A” set given in Table 4.1 unless otherwise stated. Each panel represents a change in one of the oscillation parameters whilst keeping the remaining parameters fixed.	71

1868	4.5	The oscillation probability $P(\nu_\mu \rightarrow \nu_e)$, given as a function of neutrino energy and zenith angle, which highlights an example of the “fast” oscillations in the sub-GeV upgoing region.	73
1871	4.6	Illustration of the averaging procedure for $N = 2$. The oscillation probabilities calculated on the finer left binning are averaged to obtain the oscillation probabilities in the coarser right binning. These averaged oscillation probabilities with the coarser binning are then applied to each event during the fit.	76
1876	4.7	Event rate of the SubGeV_elike_0dcy sample as a function of the number of sub-divisions per coarse bin. Each sub-plot represents the event rate of the sample at a different oscillation parameter set (thrown from the PDG priors). The red-line in each sub plot represents the mean of the event rate over the different values of sub divisions for that particular oscillation parameter throw.	78
1882	4.8	Variance of event rate for each atmospheric sample as a function of the number of sub-divisions per coarse bin. The solid red line indicates the 0.1% threshold and the dashed red line is a graphical indication of the variance at a sub-division $N = 10$	79
1886	4.9	Variance of sample likelihood, when compared to ‘Asimov data’ set at Asimov A, for each atmospheric sample as a function of the number of sub-divisions per coarse bin. The solid red line indicates the 0.1% threshold and the dashed red line is a graphical indication of the variance at a sub-division $N = 10$	80
1891	4.10	The oscillation probability, $P(\nu_\mu \rightarrow \nu_e)$ (top row) and $P(\nu_e \rightarrow \nu_e)$ (bottom row), given as a function of neutrino energy and zenith angle. The left column gives the “fine” binning used to calculate the oscillation probabilities and the right column illustrates the “coarse” binning used to reweight the MC events. The fine binning choice is given with $N = 10$, which was determined to be below threshold from Figure 4.8 and Figure 4.9.	81

1898	4.11 The calculation time taken to both calculate the oscillation probabilities 1899 and fill the “coarse” oscillograms, following the technique given in 1900 section 4.2, for the CUDAProb3 and ProbGPU (Red) calculation engines. 1901 CUDAProb3 has both a GPU (Blue) and CPU (Black) implementation, 1902 where the CPU implementation is multithreaded. Therefore, 8-threads 1903 (solid) and 40-threads (dashed) configurations have been used. Prob3, 1904 which is a CPU single-thread implementation has a mean step time of 1905 1.142s.	83
1906	4.12 The density of the Earth given as a function of the radius, as given by the 1907 PREM model (Black) and the constant density four-layer approximation 1908 (Blue), as used in the official SK-only analysis.	84
1909	4.13 The oscillation probability, $P(\nu_\mu \rightarrow \nu_e)$ (top row) and $P(\nu_e \rightarrow \nu_e)$ (bot- 1910 tom row), given as a function of neutrino energy and zenith angle. 1911 The left column gives probabilities where the constant $Z/A = 0.5$ 1912 approximation which is used in the official SK-only analysis. The mid- 1913 dle column gives the probabilities where the more accurate $Z/A =$ 1914 $[0.468, 0.498]$ values as given in Table 4.2. The right column illustrates 1915 the difference in oscillation probability between the two different tech- 1916 niques.	86
1917	4.14 The density of the Earth given as a function of the radius, as given by 1918 the PREM model (Black), the constant density four-layer approxima- 1919 tion (Blue), as used in the official SK-only analysis, and the quadratic 1920 approximation of the PREM model (Red).	87
1921	4.15 The oscillation probability, $P(\nu_\mu \rightarrow \nu_e)$ (top row) and $P(\nu_e \rightarrow \nu_e)$ (bot- 1922 tom row), given as a function of neutrino energy and zenith angle. The 1923 left column gives probabilities where the four-layer constant density ap- 1924 proximation is used. The middle column gives the probabilities where 1925 the density is integrated over the trajectory, using the quadratic PREM 1926 approximation, for each $\cos(\theta_Z)$ is used. The right column illustrates the 1927 difference in oscillation probability between the two different techniques.	88

- 1928 4.16 The oscillation probability, $P(\nu_\mu \rightarrow \nu_e)$ (top row) and $P(\nu_e \rightarrow \nu_e)$ (bot-
1929 tom row), given as a function of neutrino energy and zenith angle. The
1930 left column gives probabilities where a fixed production height of 25km
1931 is used. The middle column gives the probabilities where the produc-
1932 tion height is analytically averaged. The right column illustrates the
1933 difference in oscillation probability between the two different techniques. 92

List of Tables

1935	2.1	The various SK periods and respective live-time. The SK-VI live-time is calculated until 1 st April 2022. SK-VII started during the writing of this thesis.	21
1936			
1937			
1938	2.2	The trigger thresholds and extended time windows saved around an event which were utilised throughout the SK-IV period. The exact thresholds can change and the values listed here represent the thresholds at the start and end of the SK-IV period.	30
1939			
1940			
1941			
1942	2.3	The threshold momentum and energy for a particle to generate Cherenkov light in ultrapure water, as calculated in Equation 2.2 in ultrapure water which has refractive index $n = 1.33$	31
1943			
1944			
1945	3.1	Jeffreys scale for strength of preference for two models A and B as a function of the calculated Bayes factor ($B_{AB} = B(A/B)$) between the two models [129]. The original scale is given in terms of $\log_{10}(B(A/B))$ but converted to linear scale for easy comparison throughout this thesis.	63
1946			
1947			
1948			
1949	4.1	Reference values of the neutrino oscillation parameters for two different oscillation parameter sets.	72
1950			
1951	4.2	Description of the four layers of the Earth invoked within the average constant density approximation of the PREM model [136].	84
1952			
1953	4.3	The quadratic polynomial fits to the PREM model for four assumed layers of the PREM model. The fit to calculate the coefficients is given in [141], where $x = R/R_{Earth}$	87
1954			
1955			